FROM MOLECULAR PATHWAYS TO NEURAL POPULATIONS: INVESTIGATIONS OF DIFFERENT LEVELS OF NETWORKS IN THE TRANSVERSE SLICE RESPIRATORY NEURAL CIRCUITRY

A Thesis
Presented to
The Academic Faculty

by

Tzu-Hsin B. Tsao

In Partial Fulfillment
of the Requirements for the Degree
Doctor of Bioengineering in the
School of Biomedical Engineering

Georgia Institute of Technology
December 2010

FROM MOLECULAR PATHWAYS TO NEURAL POPULATIONS: INVESTIGATIONS OF DIFFERENT LEVELS OF NETWORKS IN THE TRANSVERSE SLICE RESPIRATORY NEURAL CIRCUITRY

Approved by:

Dr. Robert Butera, Advisor
School of Electrical & Computer Engineering
Georgia Institute of Technology

Dr. Hang Lu
School of Chemical & Biomolecular Engineering
Georgia Institute of Technology

Dr. Astrid Prinz
School of Biology
Emory University

Dr. Jeffrey Smith
National Institute of Neurological Disorders and Stroke (NINDS)
National Institute of Health

Dr. Eberhard Voit
School of Biomedical Engineering
Georgia Institute of Technology

Date Approved: August 23rd 2010

Original artwork by the author of this document.

ACKNOWLEDGEMENTS

First and foremost, I would like to express my *utmost gratitude* to Dr. Jeffrey C. Smith from NIH, who recognized issues potentially detrimental to my academic career in 2009 and took actions by bringing these issues to the attention of the proper authority. With his support, I have been able to finally defend myself. Without him, the gravity of the situation would never have been officially acknowledged, and I would never have been able to complete my research work at Georgia Institute of Technology. Therefore, I hereby thank him for his trust and respect, and will carry his grace and magnanimous example with me in my heart pour toujours.

I would also like to thank my advisor, Professor Robert Butera, who gave me free-reign to define, design, implement, and guide the evolution of my research work. In addition, especially during the committee update meetings, Professor Hang Lu, Professor Astrid Prinz, and Professor Eberhard Voit from my PhD committee have all given me invaluable guidance with infinite patience. Without them, I would not have been able to accomplish what I have accomplished during my oral defense.

A large part of the computational work presented in this document is made possible by the fine individuals from Simatra Modeling Technologies (www.simatratechnologies.com), who allowed me to set up a workstation in their office and utilized their software to finish my simulations. Research work performed by previous colleagues – Dr. Luke Purvis and Ms. Jie Shao – has provided the solid foundation which facilitated my research; for this, I cannot thank them enough. Last but not least, I would like to thank several distinguished individuals & mentors – Mrs. M. Conrad, Dr. J.X. Cui, Mr. P. Ho, Professor S.H. Huang, Dr. J. Jean, Dr. F. Kung, Mr. K. Lai, Mr. G. Liu, and Mr. C. Wei – all of them have supported me, helped me develop my career path, and taught me great courageous life lessons especially during the more difficult periods of my life – thank you!

TABLE OF CONTENTS

LIST OF TABLES

LIST OF FIGURES

SUMMARY

Mammalian breathing activities consists of three phases – the inspiratory phase, the post-inspiratory phase, and the expiratory phase. Experiments investigating the spatial organization of the neural respiratory control signals among brainstem neuron populations showed that the minimal experiment model for studying mammalian inspiratory activities is simply a brainstem slice containing the pre-Bötzinger Complex (PBC) region. This preparation is generally referred to as the transverse slice preparation.

The transverse slice preparation also contains a neuron population called the Raphé nucleus (RN). The neuromodulatory substances (e.g. serotonin, substance P, thyrotropin-releasing hormone) tonically released by the RN have been shown to modulate the activities of other respiratory-related neural networks in the preparation, such as the PBC region and the Hypoglossal Motor-nucleus (HMN). Even though neuromodulatory effects mediated by second-messenger pathways have been widely studied in other disciplines such as systems biology, such efforts have been lacking in the area of respiratory control until recently. Motivated by questions such as how external stress factors shown to manifest as different levels of neuromodulator release can affect the breathing activities itself, the PBC region and the HMN, especially their responses to neuromodulators, are central to the investigations presented in this document; since the PBC region has long been considered the "kernel" for respiratory rhythmogenesis, and the HMN produces motor-output controlling the upper airway. In addition, anatomical evidence has indicated a complex connectivity pattern among the RN, the PBC, and the HMN.

By exploiting the concept of emergent network properties and the hierarchical nature of networks, we first constructed an intracellular second messenger pathway model, and then incorporated the pathway model into previously developed single PBC

neuron & Hypoglossal Motoneuron (HM) models. The new single PBC model neuron further serves as a basis for simulating network-level PBC region activities. The methodology adopted allows us to dissect and examine the neural control signals generated by the PBC neuron, the HM, and the PBC region *in silico*, providing important basis for future investigations on the respiratory neural circuitry contained in the transverse-slice preparation.

As will be discussed in this documentation, several important conclusions can be derived regarding to the respiratory neural control signals generated at the single PBC neuron level, the single HM model, and the level of the PBC region within the transverse slice preparation. Since, with the incorporation of a second-messenger pathway model, the new PBC and HM single neuron model are able to simulate neuromodulatory effects, they represent the ideal building blocks for future investigations on the orchestrated neuromodulations in the transverse slice. The significance of pacemaking PBC neuron in a network has also been supported by examining the electrical activities generated by our simulated PBC region. Additionally, in another set of network-level simulations, it has been shown that the postulated anatomical organization of the PBC region (the small-world topology) can support network-level rhythmogenesis. Last but not least, the interactions between the two coupling types within the PBC region, e.g. the synaptic coupling and the gap-junctional coupling, have also been investigated. The results show complicated thresholding phenomena in burst period at multiple structural levels resulting from changes in the bifurcation landscape, which are in turn due to variations in the strengths of the inter-neuron couplings. These observations are in line with experiment results where the interactions between different types of couplings as well as different excitatory factors are examined in respiratory-related neurons.

1 INTRODUCTION

Important across various scientific disciplines is the concept of emergent network properties. These properties are characteristics of a network arising from the interactions among network components; they can neither manifest themselves nor be predicted unless the network is being examined in its entirety. In the area of systems biology, it has been proposed that a pathway-based drug discovery and development process other than the molecular target-based process should be adopted, as the robustness of the metabolic pathways makes it unlikely that targeting some molecular target will have predictable and beneficial functional outcome (Kumar et al. 2006; Rajasethupathy et al. 2005). In the area of neuroscience, where the functional outputs of neuronal populations control critical physiological functions, emergent network properties are especially important since a multitude of interactions exist among neurons. These interactions can include but are not limited to chemical synapses, gap junctions (electrical synapses), neuromodulatory substances, intracellular age-dependent second-messenger pathways (Puzianowska-Kuznicka and Kuznicki 2009), exogenous factors including external stimuli, and astrocytic integrations. Consequently, one of the major issues in neuroscience today involves establishing the mechanistic link between the types of interactions within a neuron population and the spatial-temporal boundaries of the complex functional output of the neuronal network in question.

In the area of respiratory rhythmogenesis, new experimental observations have led to the hypothesis that respiratory rhythm is a network emergent property rather than a direct manifestation of rhythmic pacemaking activities (e.g. intrinsic bursting activities) of some of the neurons in the respiratory neural network (Del Negro and Hayes 2008; Del Negro et al. 2008). In fact, within the "kernel" for respiratory rhythmogenesis called the pre-Bötzinger Complex (PBC), the population of pacemaking neurons has been

consistently shown to be either intrinsic or conditional. Contrary to the pacemakers that exhibit intrinsic pacemaking (e.g. bursting) properties when synaptically isolated, the pacemaking properties (e.g. bursting abilities) of conditional pacemakers are dependent upon serotonergic/noradrenergic neuromodulation (Doi and Ramirez 2008; Viemari and Ramirez 2006). The remaining PBC population is characterized as silent non-pacemakers, who exhibit either no activities or spiking activities when isolated, and respond to depolarization and serotonin/norepinephrine with intensified spiking activities. Contributing to the complexity of the collective output from the PBC region are experiment observations indicating that the PBC region is under tonic innervations from the Raphé neuron population, mediated by neuromodulatory substances such as serotonin (5HT), substance P (SP), and norepinephrine (NE) (Ptak et al. 2009). Therefore, it is not without reason that when addressing the role of neural control in respiratory activities, recent efforts have not only focused on inter-neuron interactions, but also on examining the interactions among neuron populations (e.g. inter-nuclei interactions).

Among all the available techniques applicable to obtain a better understanding of the emergent outputs of neuronal networks, computational modeling enables examinations of how isolated and controlled variations contribute to physiologically important functional network-level activities. Furthermore, when certain parameters such as baseline component concentrations and rate constants from a specific cell type describing some chemical reaction of interest are not readily available due to un-resolved experimental complications, modeling methodology provides a starting point to study these important reactions by allowing for the possibility of adopting experimentally-derived parameter values describing these reactions in other similar cell types. Using the respiratory neural control circuitry in the brainstem transverse slice as our model system, the work presented here summarizes several projects utilizing such technique to focus on the investigation and categorization of important network emergent properties at multiple network structure levels. This transverse slice respiratory neural circuitry includes the

Raphé nucleus, the PBC region, and the Hypoglossal Motor-nucleus (HMN), all of which are discussed in details in Section 2.1 (Figure 2-1). The outline and logical flow of the projects are presented in Figure 1-1.

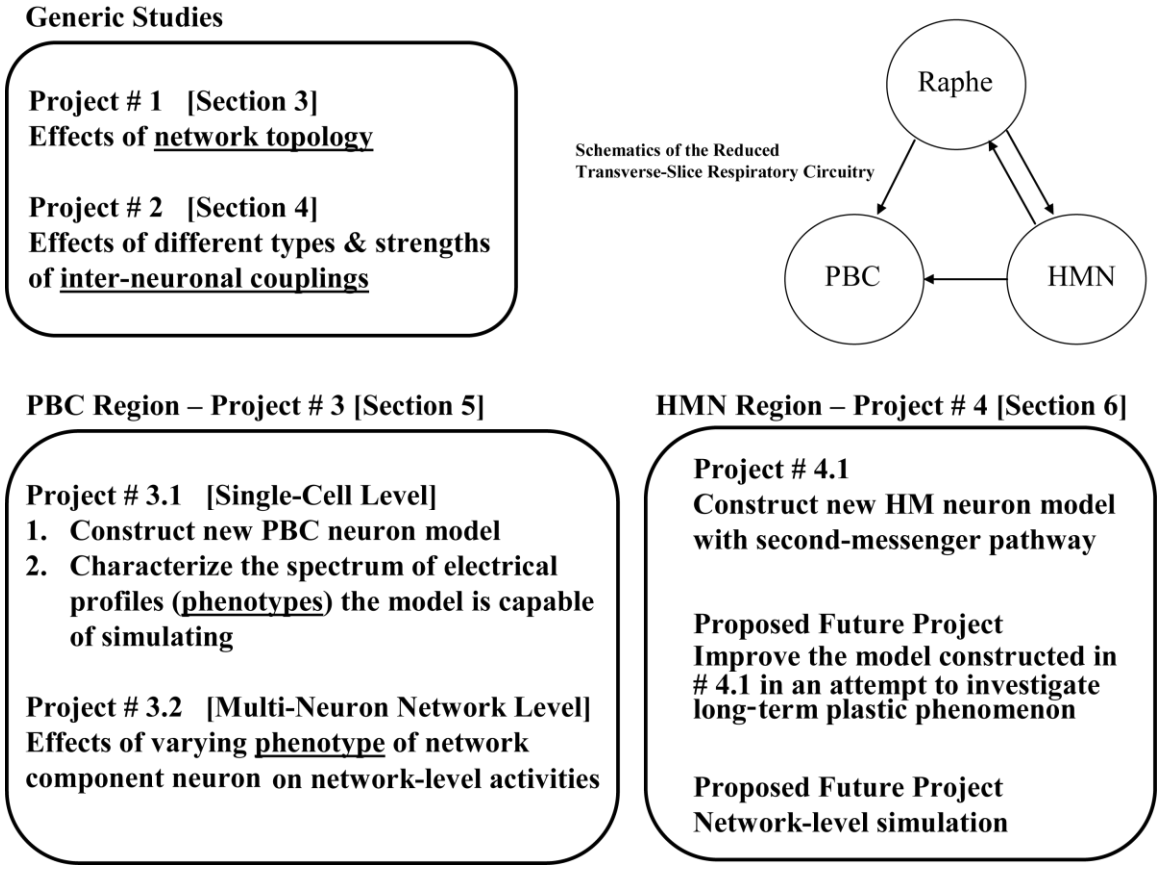

Figure 1.1 Structure of the research presented.

With discourses into studies which delve into the emergent properties in more generalized neural networks, the end goal of this research project is to resolve how a certain intracellular second-messenger pathway, how network topology and inter-neuron couplings can influence single-cell and network-level activities. The results presented in this document will facilitate future investigation of some of the unresolved phenomena – such as long-term facilitation (LTF) – manifesting as network emergent properties in the area of respiratory neural control (Figure 1-2).

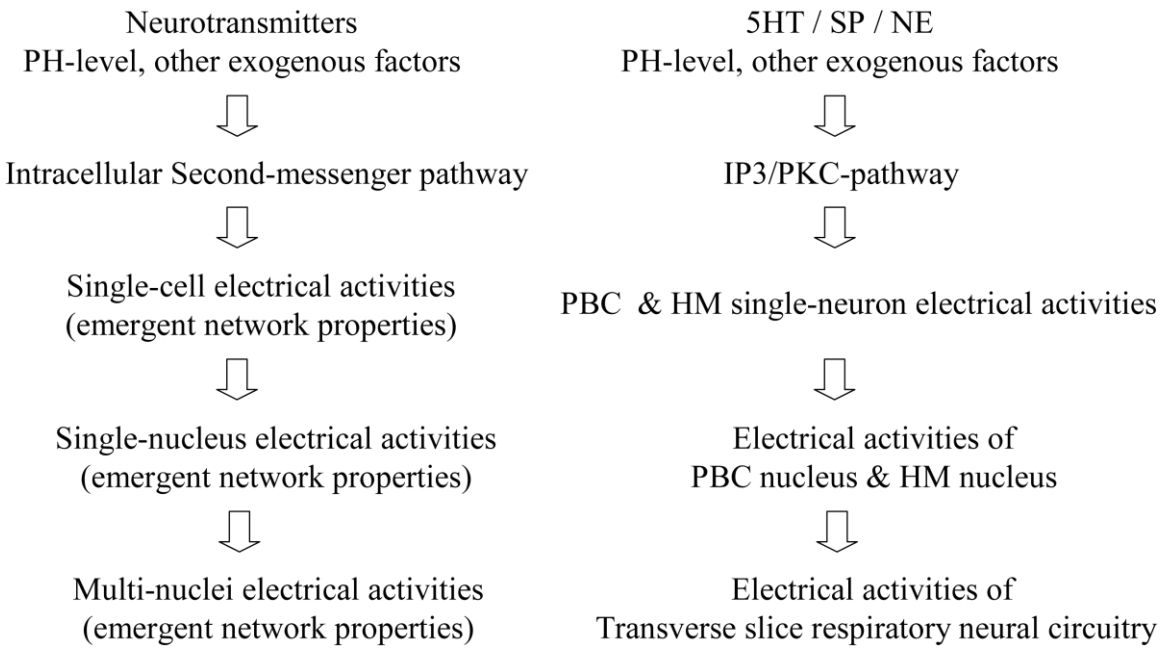

Figure 1.2 Manifestation of the effects of exogenous factors on network-emergent properties at different levels.

2 BACKGROUND & SIGNIFICANCE

2.1 Significance of the Research Projects

Breathing is a fundamental neurophysiological process involving the rhythmic activation of populations of spinal and cranial motoneurons required to sustain life and health. Understanding the CNS mechanisms responsible for the generation, the maintenance, and the reconfiguration of the respiratory rhythm and pattern is required to understand the neural control of breathing in health and disease. For example, the third leading cause of infant death in 2003 in the United States was Sudden Infant Death Syndrome (SIDS), accounting for 2162 deaths nation-wide (Mathews and MacDorman 2006). While SIDS is complex to diagnose and may have multiple causes, evidence suggests that abnormalities in the neural circuitry responsible for the generation and control of the respiratory rhythm (Carpentier et al. 1998; Guntheroth and Spiers 2002; Kinney et al. 1995; Obonai and Takashima 1998; Obonai et al. 1998) are involved in pathophysiological conditions such as SIDS. In particular, these abnormalities may be due in part to a delay in neuronal development (Becker and Zhang 1996; Saito et al. 2001) and dysfunction of the medullary serotonergic system (Kinney et al. 2005; Panigrahy et al. 2000; Paterson et al. 2006).

We are still a long way away from fully understanding the dynamics of the complex circuitry that is responsible for the generation and control of the respiratory rhythm. The spatial organization as well as the state-dependent respiratory pattern and rhythm generation have been elucidated in both experiments and computer simulation work (Rubin et al. 2009; Rybak et al. 2007). Other recent experimental advances are exemplified by various reduced preparations for investigating respiratory rhythm. These reduced preparations are the en bloc (Feldman et al. 1991; Smith et al. 1990; Suzue 1984), the transverse slice (Smith et al. 1991), and the sagittal slice preparations (Mellen et al.

2002). These reduced preparations from neonatal rodents have provided powerful tools for studying the CNS respiratory circuitry in a highly reduced setting that still maintains critical aspects of the respiratory rhythm. Beyond advances in experiment preparations, research publications in the past two years have also indicated significant movement toward emphasizing how functional network level output manifests differently depending upon various neuromodulatory factors at play, the downstream second-messenger pathways triggered by these neuromodulatory factors, as well as the direction of interactions among various nuclei in the respiratory circuitry (Doi and Ramirez 2008; Lega et al.; McIntyre et al. 2004; Ptak et al. 2009).

In the work presented here, the focus is the respiratory neural control circuitry contained in the transverse slice preparation (Figure 2-1) containing the PBC region, and which has been shown to be the minimal experiment model for studying the inspiratory activity in mammals (Ruangkittisakul et al. 2008; Rybak et al. 2007). The ultimate goal is to elucidate how the interactions within and among the distinct neuron populations contained in the circuitry affect physiologically important neural outputs such as those from the PBC region or the HM nucleus. While the long-term goal is to develop an integrated computational model of the mammalian respiratory circuitry in the transverse slice (Figure 2-1), the intermediate steps accomplished here are the construction of new generation single neuron models (Figure 1-1), as well as the completion of network level studies on emergent properties either in a general sense or specific to the respiratory-related neuron populations (Figure 1-1).

Based on previously developed models, the new generation ion-channel based models of respiratory-related neurons constructed are those of the Raphé neuron (Chapter 7), the PBC neuron (Chapter 5), and the HM neuron (Chapter 6) found in the transverse slice preparation. The important aspect that sets these new neuron models apart from previous work is the inclusion of the interactions among ion-channel properties, intracellular ion concentration, and second-messenger pathways. Together, these

mechanisms facilitate the simulated electrical profiles to both qualitatively and quantitatively reproduce experimental recordings of neuronal activities with or without the presence of multiple modulatory factors such as the pH value or neurotransmitters (e.g. serotonin, norepinephrine). As will be detailed in later chapters, the new PBC model neuron can simulate two different pacemaking (e.g. bursting) modes. Per experiment observations, each of these two pacemaking modes can be selectively abolished by the application of Riluzole and Cadmium (Cd) (Del Negro et al. 2002a; Pena et al. 2004; Thoby-Brisson and Ramirez 2001). The new model faithfully reproduces features of the two pacemaking modes by including distinct mechanisms responsible for the pacemaking properties in each mode – namely, the conductance of persistent sodium current (g_{nap}) and the conductance of calcium-activated cationic current (g_{can}). On the other hand, the second-messenger signaling pathways in the new HM neuron model qualitatively reproduces serotonergic modulatory effects as seen in experiments (Feldman et al. 2005; Neverova et al. 2007). Furthermore, the new HM model provides a basis for identifying possible underlying mechanisms for long-term plasticity such as long-term facilitation (LTF). With careful evaluations, the principals derived from such plasticity which not only depends on the stimulus type and strength, but also on stimulus pattern, may be generalized to explain similar phenomena observed in other animal models.

In summary, by assimilating novel data from these reduced preparations, valuable insights derived from studies regarding to network topology and multiple inter-neuron interactions at the neural network level, and the pathway modeling methodology traditionally adopted in the discipline of systems biology – we have developed a series of new computation models of critical neural components of the respiratory pattern-generating network. These models can eventually serve as the basis of a new transverse slice model and beyond (e.g. a model of the brainstem respiratory circuitry), which can potentially facilitate the investigation of important emergent functional output.

The following sections contain summarizing background descriptions of the current and pressing concepts, topics, and techniques specific to the area of respiratory control relevant to the defined scope of this work. Since the majority of the work presented in this document is based on improved versions of single neuron models published in Purvis et al. 2007 as well as Purvis and Butera 2005, these neuron models will be reviewed in a section after the concept of electrical & chemical signaling in neural systems has been introduced. The review on previous models will be followed by a brief description on the technique of nonlinear bifurcation analysis, which is frequently adopted throughout this document in an attempt to understand simulated electrical activities of neurons in a mathematical context. Furthermore, details will be provided on the general perspectives of how commonly identified factors such as network topology, intra- and inter-nuclei interactions, and neuromodulatory factors acting via second-messenger pathways may exert their influences on the emergent properties of various networks in the model system, e.g. transverse slice preparation.

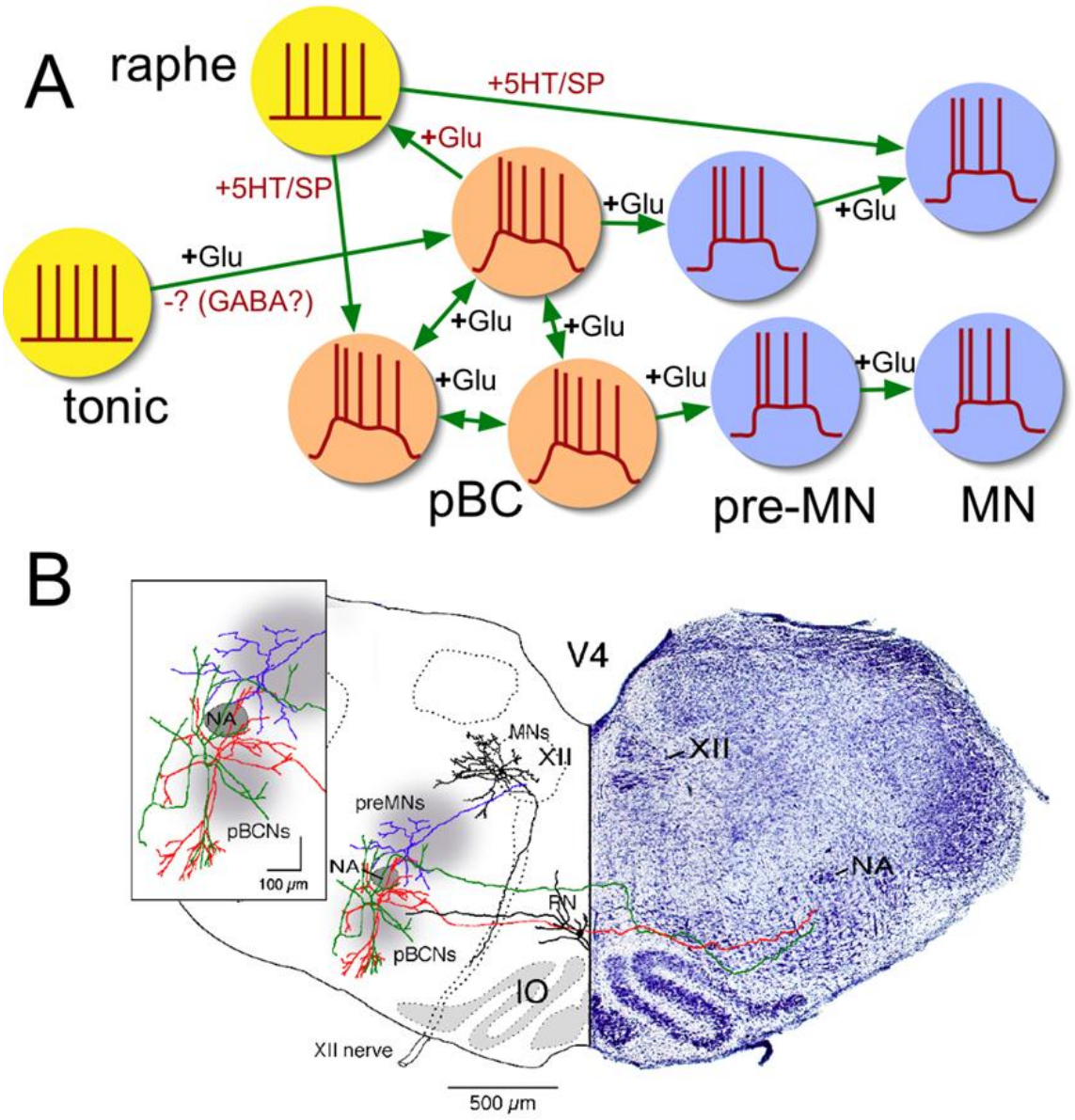

Figure 2.1 Spatial organization of the respiratory neural circuitry in neonatal rat transverse slice preparation. Panel A. Conceptual illustration of tonically firing neurons and Raphé neurons (yellow), pBC neurons (orange), pre-motor and motoneurons (blue) and putative synaptic connections. The green arrow indicates the direction of influence mediated by neuromodulatory substances (Glu: glutamate, 5HT: serotonin, SP: substance P, GABA: γ-Aminobutyric acid), with the preceding plus sign indicating an excitatory effect and the minus sign indicating an inhibitory effect. Panel B. Electrophysiologically identified transverse slice respiratory circuit neurons, morphologically reconstructed from representative neurons filled with neurobiotin during whole-cell patch-clamp recording, are PBC neurons, including pacemaker neurons with intrinsic bursting properties (red) and non-pacemaker neurons

(green), pre-motoneurons (preMNs, blue), and hypoglossal motoneurons (HMs, black). Figure adopted from Ptak et al. 2009.

2.2 Neuronal Signaling – ion channels, synapses, gap junctions and more

The essential function of all nervous systems is signaling, or information transfer, both intra-cellularly from one part of a cell to another, and inter-cellularly between cells. For the purpose of providing a solid basis to understanding the research work presented here, the emphasis in this section will be placed on the following two topics: 1.) the generation of action potential 2.) the two types of highly specialized structures – chemical synapses and electrical synapses (e.g. gap-junctions) – responsible for intercellular signaling.

Ion Channels underlie electrical signaling in neurons

Within each neuron, signaling is accomplished by transmission of electrical activity in the form of an "action potential" (AP, Figure 2-2, Panel A) from one part of the cell to another. An AP is a large all-or-none fluctuation in the membrane potential. This membrane potential (V) is a direct result of an unequal distribution of electrical charges on the two sides of the membrane. The distribution of electrical charges is not static. In fact, movement of ions across the plasma membrane can be facilitated by specialized membrane proteins called ion channels. The ion channels are not inert pores in the membrane; on the contrary, they can undergo rapid conformational changes between an open state (e.g. able to conduct ions) and a closed state (e.g. not allowing ions to pass). The permeability of these ion channels, among other factors, is dependent upon time and membrane voltage (V), which is in turn dependent upon the re-distribution of ions across membranes (ΔV). A direct result from such two-way dependency is an orchestrated sequence of ion movements required to generate an action potential.

A

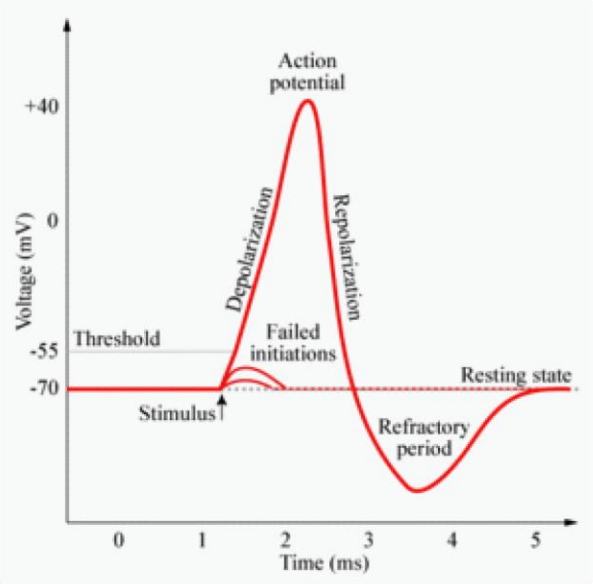

B

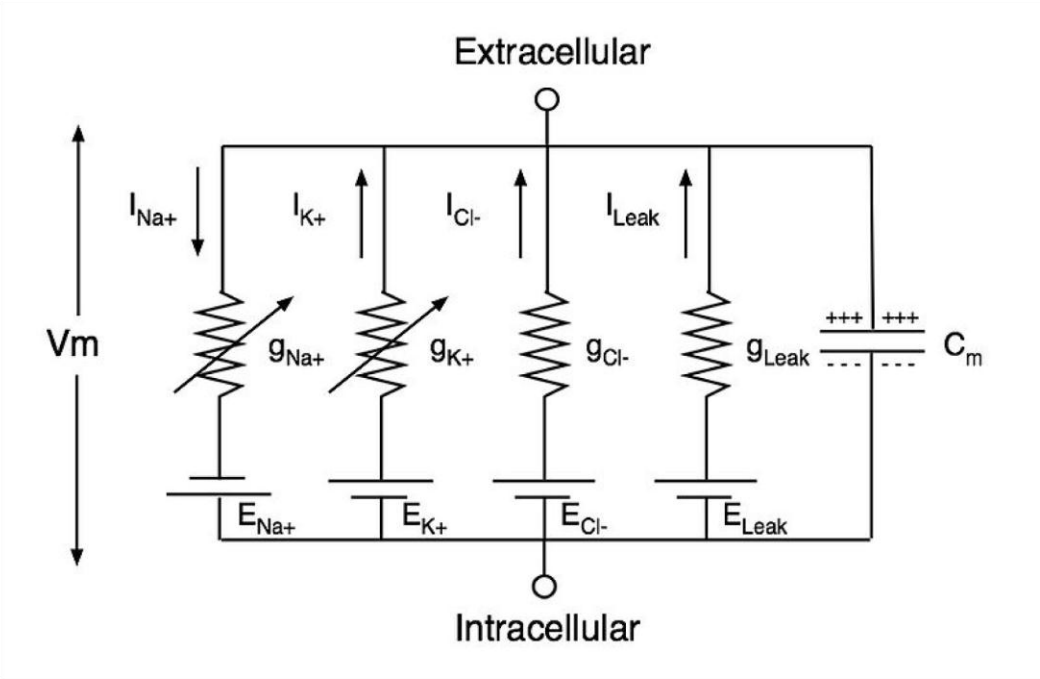

Figure 2.2 A typical action potential and the electrical circuitry representation of a Hodgkin Huxley style neuron model. Panel A illustrates the all-or-non nature of an action potential; the figure is adopted from http://mindoutpsyde.com/forums/index.php?topic=144. Panel B illustrates the components of a typical Hodgkin-Huxley style model showing how membrane voltage is determined as the electrical potential difference across the cell membrane; this figure is adopted from http://en.wikipedia.org/wiki/File:MembraneCircuit.jpg. The lipid bi-layer cell membrane is represented as a capacitance, and the voltage-gated sodium & potassium channels are represented by time-dependent and

voltage-dependent conductances. On the other hand, the leak channel and the chloride channel are represented by linear conductance (g_L, g_{cl}). The electrochemical gradient as the driving force behind ion flows are presented by the batteries (e.g. ENa+, EK+). The arrow indicates current, for example, the sodium current is presently flowing from the extracellular to the intracellular space.

Due to a direct analogy between ion movements in electrical circuit, the ion channels can be modeled in the form of a parallel conductance-resistor electrical circuit (Figure 2-2, Panel B). Specifically, the relationship between movement of charged ions across plasma membrane through ion channels and the fluctuation in membrane potential translates into the following equation:

$$C_m \, dV/dt = \sum I_{ionic}$$

where C_m is the membrane capacitance and $\sum I_{ionic}$ is the sum of ionic movement (current) inward or outward across the membrane. Using the convention illustrated in Figure 2-2, it can be deduced that an inward movement of positively charged ions (inward current) will cause an increase in the membrane potential. This inward current is described as "depolarizing" and the increase in membrane potential is described as a "depolarization". In most cases, the ionic movement is subject to the changes in ion-channel conductance and the electrical field created by charge distribution on both sides of the plasma membrane. Each individual ion current can be modeled in the form of the following equation:

$$I_{ionic} = g_{ion\text{-}channel} * (V\text{-}E_{ion})$$

where E_{ion} is a constant term approximating the electric field due to the ion distribution across the plasma membrane and V is the membrane potential. The term $g_{ion\text{-}channel}$ is the ion channel conductance, which is itself a function of V and modeled as a combination of differential equations:

$$g_{ion\text{-}channel} = g_{max} * \Pi \, x_i$$

$$dx_i / dt = F(V, t)$$

where g_{max} is the maximum conductance for the current. On the other hand, the value of the gating variable x_i describing the conformational change of the ion channel depends on both time and membrane voltage.

Throughout this presentation, the neuron models introduced were constructed based on the same concepts behind the equations outlined in this section.

Electrical Synapse

Intercellular communication through gap junctions is conceptually the very simplest form of cell-to-cell interaction. Small molecules and ions in one cell diffuse through pores in the plasma membrane directly into the plasma of a neighboring cell. These bi-directional connections between nerve cells via gap junctions are called "electrical synapses", due to the fact that this form of information transfer involves rapid electrical signaling. These electrical synapses allow the electrical activity of one neuron to be registered quickly in neighboring neurons and have been shown to allow groups of neurons to synchronize their electrical activities (Rohr 2004; Tribulova et al. 2008).

Chemical Synapse

Chemicals that are released from a neuron (pre-synaptic) and alter the excitability of another neuron (post-synaptic) are termed "neurotransmitters". A large number of such neurotransmitters act as extracellular signals to mediate the uni-directional information transfer among neurons through a special structure called "chemical synapse". These chemicals include amino acid, organic compounds, as well as small peptides, and are contained in vesicles for storage. Typically, these chemicals either directly activate the ion channels of the post-synaptic neuron, thus causing ions movement – or trigger a series of post-synaptic intracellular events – to alter the membrane potentials of the post-synaptic neurons. When a neuron is stimulated, e.g. when external factors cause the membrane potential of a neuron to fluctuate, the

transmitter-containing vesicles fuse with the neuron's plasma membrane and release their contents into the synaptic cleft. The chemical synapse can be either excitatory or inhibitory, and the model formulation of chemical synapses demonstrates this relationship of dependency of the post-synaptic ion movement on the pre-synaptic membrane voltage:

$$dS/dt = F(V_{pre}, S); \; I_{post} = G_{syn}*S*(V_{post} - E_{syn})$$

where S is the activation parameter modeling the process of vesicular secretion of neurotransmitters, V_{pre} is the pre-synaptic voltage, V_{post} is the post-synaptic voltage, and I_{post} is the post-synaptic ion current triggered by the neurotransmitter released pre-synaptically.

2.3 Review: previous PBC neuron model and Hypoglossal Motoneuron model

The new single PBC neuron model and the single HM model presented in Chapter 5 and 6 of this document are based on previously published models (Butera et al. 1999a; Purvis and Butera 2005; Purvis et al. 2007). By incorporating a second-messenger pathway model into these base models, these new models are able to simulate serotonergic neuromodulatory effects observed in experiments. In the case of the new PBC neuron model, it is now possible to simulate recent experiment results (e.g. two types of pacemakers, see Chapter 5) that have been the source of controversy in the area of respiratory rhythmogenesis. Since the new models can be considered as extensions of the previous models, a brief summary is provided here in an attempt to provide readers with the necessary background information.

Single PBC neuron model

The PBC neuron model presented in Purvis et al. 2007 is a single-compartment Hodgkin-Huxley style model (Hodgkin and Huxley 1952). The model consists of four ionic currents 1.) a fast Na^+ current and a leak current, 2.) a delayed K^+ current, 3.) a

slowly inactivating persistent Na^+ current (I_{nap}), and 4.) a K^+ - dominated leak current. In this model, the persistent sodium current (I_{nap}) is critical for the model neuron's voltage-dependent bursting activity. Other currents in this model include a tonic current and a synaptic current, where the former current represents the non-NMDA EAA-mediated (Excitatory Amino-Acid) drive received by a single PBC neuron from other tonically spiking neurons in experiment preparations. The synaptic current, on the other hand, is an excitatory EAA-mediated drive between individual PBC neurons (Butera et al. 1999a; b). In short, the membrane potential of the model is determined by the following equations. The parameter naming convention used here follows that introduced in the previous sub-section. The readers are further encouraged to refer to Butera et al. 1999a, Purvis et al. 2007, or Appendix B for the equations used in this model.

$C_m \, dV/dt = \sum (I_{ionic} + I_{tonic} + I_{syn} + I_{leak})$;

$I_{ionic} = g_{max} * x * (V - E_{ion})$; where the gating variable x is formularized as follows.

$dx/dt = [x_\infty(V) - x]/\tau_x(V)$;

where $x_\infty(V) = 1/[1 + \exp((V-\theta_x)/\sigma_x)]$ as the steady-state voltage-dependent activation or inactivation function of x, and τ_x is the voltage-dependent time constant determined by the following equation:

$\tau_x(V) = \tau_x/\cosh[((V- \theta_x)/2\sigma_x)]$

$I_{leak} = g_{leak} * (V-E_{leak})$; the leak current is modeled as an ohmic current,

$I_{tonic} = g_{tonic} * (V-E_{tonic})$

Assuming the binding of transmitter is rapid due to non-NMDA glutamatergic receptor activation (Butera et al. 1999b), the synaptic current I_{syn} can be modeled as:

$I_{syn} = (\sum (g_{syn} * S)) * (V - E_{synaptic})$, where $dS/dt = [(1-S)*S_\infty(V) - k*s]/\tau_s$

Single HM neuron model

The HM neuron model presented in Purvis and Butera 2005 does have its drawbacks due to limited information on 1.) ionic currents in motoneuron types other than those in neonatal rats, 2.) 3-D morphology of the HM neuron, and 3.) development changes in ion current properties and the neuron's morphology; nevertheless, the model (Purvis and Butera 2005) is able to reproduce several electrophysiological features of the HMs. Therefore, this model is chosen to be the basis of work focusing on serotonergic neuromodulatory effects of HMs to be presented in Chapter 6 of this document.

The previously developed HM neuron model has ten currents, 1.) a fast sodium current, 2.) a persistent sodium current, 3.) a delayed rectifying potassium current, 4.) a low voltage-activated calcium current, 5.) two high voltage-activated calcium current, 6.) calcium-induced potassium current, 7.) a fast transient potassium current, 8.) a hyper-polarization activated depolarizing current, and 10.) a leak current. The equations for the aforementioned currents also follow the Hodgkin-Huxley formalism as those in the PBC neuron model. The readers are encouraged to refer to Purvis and Butera 2005 for detailed discussions on how the ten currents interact with each other to reproduce experiment observations. The equations used in this model can also be found in Appendix B.

2.4 Nonlinear Bifurcation Analysis

Nonlinear bifurcation analysis is a tool adopted in this work to analyze the set of non-linear ordinary differential equations (ODEs) used to describe single-cell model neurons (Section 2.2). The purpose of the bifurcation analysis is to elucidate how the quasi steady-state solution of a selected model variable of interest behaves at different values of the *bifurcation parameter*. In this work, the bifurcation parameter is often used in association with quasi-steady-state assumptions and is a model variable that normally varies at a time scale much slower than other state variables in the model. In all the bifurcation analyses presented in this work, the model variable of interest is the

membrane voltage of neuron manifesting as the pacemaking, e.g. bursting, activities (Figure 2-3, top trace in the left portion) in the PBC neuron.

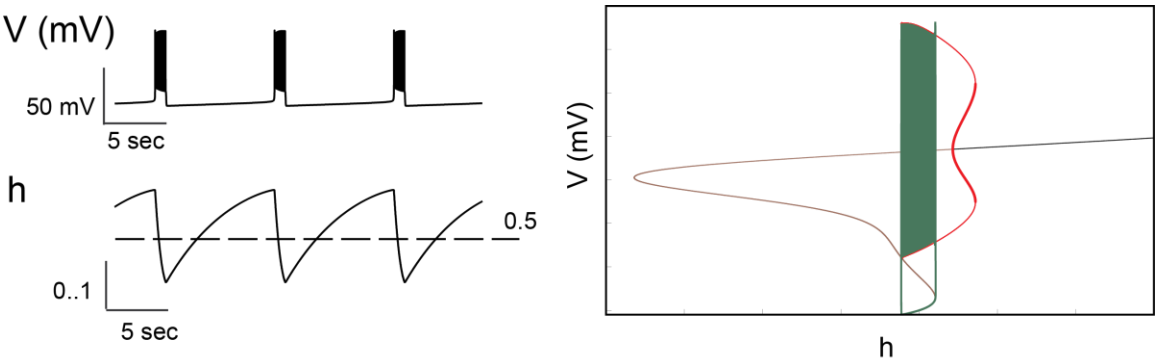

Figure 2.3 The bifurcation diagram using the PBC model neuron as an example. The neuron's membrane voltage (V) and the corresponding variations in the activation variable for the persistent sodium current (h) are shown on the left. The bifurcation diagram is shown on the right, where the bursting trajectory is super-imposed in green. The color black indicates stable steady state solution; the color brown indicates the unstable steady state solution. The color red indicates period solution (thick: unstable, thin: stable).

Using the PBC model neuron operating in the pacemaking mode sensitive to Riluzole application (Section 2.1) as an example, the top trace in the left portion of Figure 2-3 illustrates the typical bursting activity. The corresponding variations in persistent sodium current activation (h, bifurcation parameter) observed in the PBC neuron are shown in the bottom-left portion of Figure 2-3. The result from bifurcation analysis is illustrated in the right portion of Figure 2-3. With the bursting trajectory from the top-left super-imposed (green) on the bifurcation landscape, the bifurcation analysis shows how the value as well as the stability of the solution of the membrane voltage (V) changes as the activation level of persistent sodium current varies.

2.5 Network Topology

Previous research has provided anatomical evidence showing that in some cortical regions in the mammalian brains are inter-connected according to a small-world (SW)

network topology (Hartelt et al. 2008). In addition, results from modeling studies (Netoff et al. 2004; Ponten et al. 2007) conducted previously demonstrate a dependency of network activities on network topologies. For example, in Netoff et al. 2004, it has been shown that regular network firing activities intensifies to "seizing" activities, and eventually transitions into bursting activities as network topology changes from regular lattice to SW, and eventually to random connectivity; where, in general terms, a network with a regular lattice topology is a network where each neuron is connected to a specific number (*k*) of its nearest neighbor. Starting from a network with regular lattice topology, a SW network topology can be constructed by reconnecting (*pr*(reconnection) = *p*) these synaptic projections to randomly chosen post-synaptic neurons. Lastly, as the name suggests, a network exhibiting a random network topology is a network where synaptic projections are randomly established between pairs of neurons. Furthermore, starting from a network with regular lattice topology, the random network topology can be achieved when the reconnection probably, e.g. *pr*(reconnection), is set to 1.

Various formal measures have been developed to characterize the topology of a network. A few examples of these measures include averaged path length (L), clustering coefficient (C), degree, closeness, betweenness centralization, and betweenness centrality, among which two of the most commonly used measures are the averaged path length and the clustering coefficient. The averaged path length (L) is the average number of steps, i.e. nodes, along the shortest path one must traverse between all possible pairs of nodes in a network; whereas the clustering coefficient (C) measures the density of local connections as the ratio between the actual number of local connections and all possible local connections within a neighborhood. In a "small-world" network, groups of nodes are neighbors of each other (large C); however, most nodes can be reached in a small number of steps from other nodes in the network (low L). Therefore, the SW network topology is characterized by a low L and a high C. Similarly, the regular lattice network

is characterized by a high C and a high L, and the random network is characterized by a low L and low C.

As previous research has established a link between the SW network structure and "seizure-like (e.g. seizing)" or bursting activities (Netoff et al. 2004), the SW network topology that has been studied extensively in areas such as epilepsy where network synchronization is of extreme importance (Netoff et al. 2004; Ponten et al. 2007). Other network topologies have also begun to receive notice in the area of neuroscience, as it has been postulated that the changes in respiratory pattern during embryonic development associated with the cause of Rett syndrome can be explained by the phase transition of these two network structures (Mironov 2009; Mironov et al. 2009). Furthermore, specific to the work presented in this documentation, recent imaging work using enhanced green fluorescent proteins to label both the neuronal cell bodies and dendrites of neurons contained in the respiratory kernel (e.g. the PBC region) has shown that the neural organization of the PBC region is modular and characterized by "clusters" typical of both the "small-world" and the "scale-free" network structures (Hartelt et al. 2008).

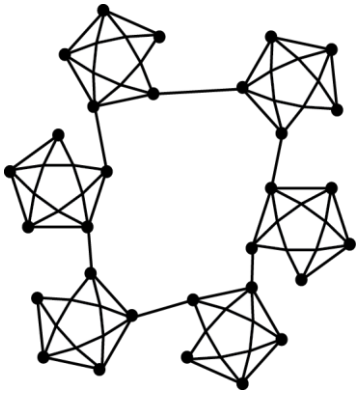

Figure 2.4 An examples of small-world network – the "caveman" graph (Watts 1999). Clusters of caves are interconnected to each other; these inter-caves connections form the edges of the larger "ring" and were transferred from within each cave. The readers are encouraged to refer to page 102~109 of Watts 1999 for detailed ruminations on this interesting network topology.

2.6 Summary: Investigating Network-Level Activities in the Transverse-Slice Respiratory Circuitry

As briefly outlined in the previous section, the PBC and neighboring respiratory-related neural populations in the transverse slice are responsible for generating and shaping the *in vivo* respiratory rhythm where different rhythmic patterns emerge as the interaction among neurons varies. The variations in rhythmic patterns can be due to either changes at the cellular level, e.g. ionic flux dynamics, changes at the network level, e.g. synaptic efficacy introduced in the previous sections, or changes at how the neural populations interact with each other (Ptak et al. 2009). Previous research work has demonstrated that these variations can also be induced by exogenous modulatory factors such as 5HT (Richter et al. 2003), substance P (Gray et al. 2001; Pena and Ramirez 2004; Ptak et al. 1999), and pH levels (Koizumi et al.).

These neuromodulatory factors assert their influences differentially on various types of respiratory neurons by either directly altering ion channel conductance or by triggering a second-messenger signaling cascade that eventually leads to changes in membrane potential. Specifically, endogenously activated $5HT_{2A}$ receptors are required for maintaining fictive respiratory activity in transverse slice by modulating the persistent sodium conductance (g_{nap}) in both Cd-sensitive and Cd-insensitive pacemaker neurons via a PKC pathway (Pena and Ramirez 2002). Substance P, on the other hand, modulates network activities by producing slow depolarization via activation of a low-threshold Tetradotoxin (TTX)-insensitive Na^+-dominant cationic current (Pena et al. 2004). While both 5HT and substance P modulate neuronal activities with time-dependent depolarization-related mechanisms, pH variations act on two-pore potassium TASK channels that form a prominent leak conductance and display little time or voltage dependence (Koizumi et al.).

The neuromodulatory factors do not act in isolated fashion, as different factors might have a common modulatory target. For example, in addition to being sensitive to pH in a narrow physiological range (Bayliss et al. 2001; Patel and Honore 2001), TASK channels are also subject to 5HT modulation (Talley et al. 2000). The PKC pathway that plays an important role in the modulatory effect mediated by $5HT_{2A}$ receptors can also induce changes in neuronal activity via alterations in intracellular calcium dynamics (Feldman et al. 2005) as well as changes in metabotropic glutamate receptor (mGluR) activation (Francesconi and Duvoisin 2000). The latter target, e.g. the metabotropic glutamate receptor, has also been demonstrated to selectively control "fictive sighs" in vitro but have no effect on fictive eupnea (Lieske and Ramirez 2006). The PKA pathway down-stream of G-protein coupled receptor for excitatory norepinephrine also putatively modulates inspiratory-phased inhibition prevalent in neonatal hypoglossal motoneurons (Saywell and Feldman 2004), and is consequently essential for maintaining the balance between excitation and inhibition in hypoglossal motoneurons (HMs).

In addition to the aforementioned excitatory factors, respiratory-related neurons including PBC, Raphé, hypoglossal motoneurons have also been shown to rely on their GABAergic as well as glycinergic transmission to maintain the overall network rhythmic discharge (Singer and Berger 2000). Furthermore, the existence of electrical couplings in respiratory-related neurons has been verified (Rekling et al. 2000) and their contributions cannot be overlooked. While NMDA receptors constitute the largest excitatory drive in hypoglossal neurons during inspiration, previous research indicates that gap-junction couplings are also actively involved (Wang et al. 2002). It has also been shown that the bath application of gap-junctional blockers in both the transverse slice and the en-bloc preparations modulate rhythmic inspiratory activities at multiple time scales (Bou-Flores and Berger 2001; Elsen et al. 2008). The fact that neurons existing in the transverse slice that constitute the respiratory circuitry of interest communicate with each other via local

electrical coupling as well as synaptic connections which can be local or long-range projections provides grounds for further investigations detailed in later chapters.

Due to the compounding nature of all the factors that can significantly affect functional network-level output, a modeling study that takes into account each individual mechanism as well as interactions among these pathways can lead to a better understanding of respiratory rhythmogenesis in vivo. The architecture of the model system – the respiratory neural circuitry in the transverse slice – used in this work to study the complex interactions outlined above can be summarized as follows (Figure 2-1).

Tonically firing neurons in the Raphé nucleus (RN) project to the PBC and have been shown to co-release 5HT, SP, and thyrotropin-releasing hormone (TRH); additional tonic neurons providing glutamatergic input to the PBC are found throughout the slice. The PBC axons project contralaterally through the midline to the PBC on the opposite side of the slice. In addition, axon collaterals of some PBC neurons project to the pre-motor nucleus (preMN) region. In contrast, the preMN region projects ipsilaterally to hypoglossal motornucleus (HMN). Thus the output of the PBC projects to the HMN via a two-neuron pathway that is ipsilaterally preserved.

In the following chapters, results from a series of simulations studies based on this model system will be detailed to illustrate the results of our efforts to investigate how neurotransmitters, type and strength of inter-neuron couplings, and network topology, can affect outputs at either the single-cell level or the level of an individual nucleus. Additionally, several future investigations that can be essential to further our knowledge in the area of respiratory neural control are proposed in the last chapter of this document.

3. NETWORK-TOPOLOGY DEPENDENT NETWORK-LEVEL PHENOMENA[1]

3.1 Abstract

"Bursting" is a dynamic phenomenon where episodes of neural activities are punctuated by periodic episodes of inactivity. At the single cell level, this phenomenon is frequently referred to as "pacemaking", where episodes of action potentials are punctuated by periods of silence. Typically, the process for burst initiation as well as the slower processes underlying burst termination at this level can be attributed to the interactions between fast and slow ion channel properties, calcium-dependent processes, or synaptic depression.

Single-cell level bursting activities are ubiquitous in neural systems. Network-wide rhythmic bursts of electrical activities in a neural network, characterized by inactivity-punctuated episodes of action potentials from all or a large portion of the neuron population, are also present in a variety of neural circuits. Examples include components of the respiratory rhythm generating circuitry in the brain stem (Del Negro et al. 2002b), spontaneous activity in the neonatal rat spinal cord (Bracci et al. 1996), and developing neural networks in the retina of the immature ferret (Harris et al. 2002). In most cases, the recurrent excitation through excitatory synaptic connections determines burst initiation, and the slower kinetics of ionic currents or synaptic depression at the single cell level collectively results in burst termination at the network-level.

[1] The majority of the work presented in this chapter is published as "Bursting without slow kinetics: a role for a small world?" Neural Comput. 2006 Sep;18(9):2029-35, of which the author of this document is the second author. The author of this document reproduced all results published in the paper, and contributed independently to the investigation of the burst termination mechanism, as well as to establishing the link between the value of synaptic delay and network-level "seizing" or "bursting" activities. All figures, unless otherwise specified, are produced independently by the author of this document,

The work presented in this chapter explores another mode of network-level rhythmogenesis (e.g. rhythm generation); namely, the bursting phenomenon in a network where no slow processes exist at the single-cell or synaptic level. Our investigation indicates that the bursting phenomenon critically depends on the connectivity of the network characterized as a small-world (SW) network. Furthermore, the progressive synchronization of network activities within each burst serves as the slow process which underlies burst termination.

3.2 Methods

To examine the direct contribution of the connectivity pattern among neurons to network-level activities, we utilize a paradigm detailed previously (Watts and Strogatz 1998) to modify the network structure from a localized connection in conjunction with utilizing the Morris-Lecar (ML) model as the component neurons.

Morris-Lecar Neuron Model

The ML model was originally developed to characterize the electrical activity of the barnacle muscle fiber (Morris and Lecar 1981). The model consists primarily of two voltage-dependent ion channels – an inward Ca^{2+} channel and an outward K^{+} channel. Both channels possess voltage-dependent activation, and neither channel possesses voltage-dependent inactivation. The ML model is considered a prototypical neural oscillator. It possesses the general characteristics of the activity "envelope" of bursting neurons.

In response to an injected current pulse, the firing activity of ML model neuron typically consists of an excitation followed by a repolarization phase (Figure 3-1, Panel A). The ML model is distinct from the typical canonical neuron model (e.g. Hodgkin-Huxley or Integrate-and-Fire model) in its response to two successive transient current pulses (Figure 3-1, Panel B & C). An action potential developed by a canonical model

has a well-defined absolute and relative refractory period. In contrast, due to the

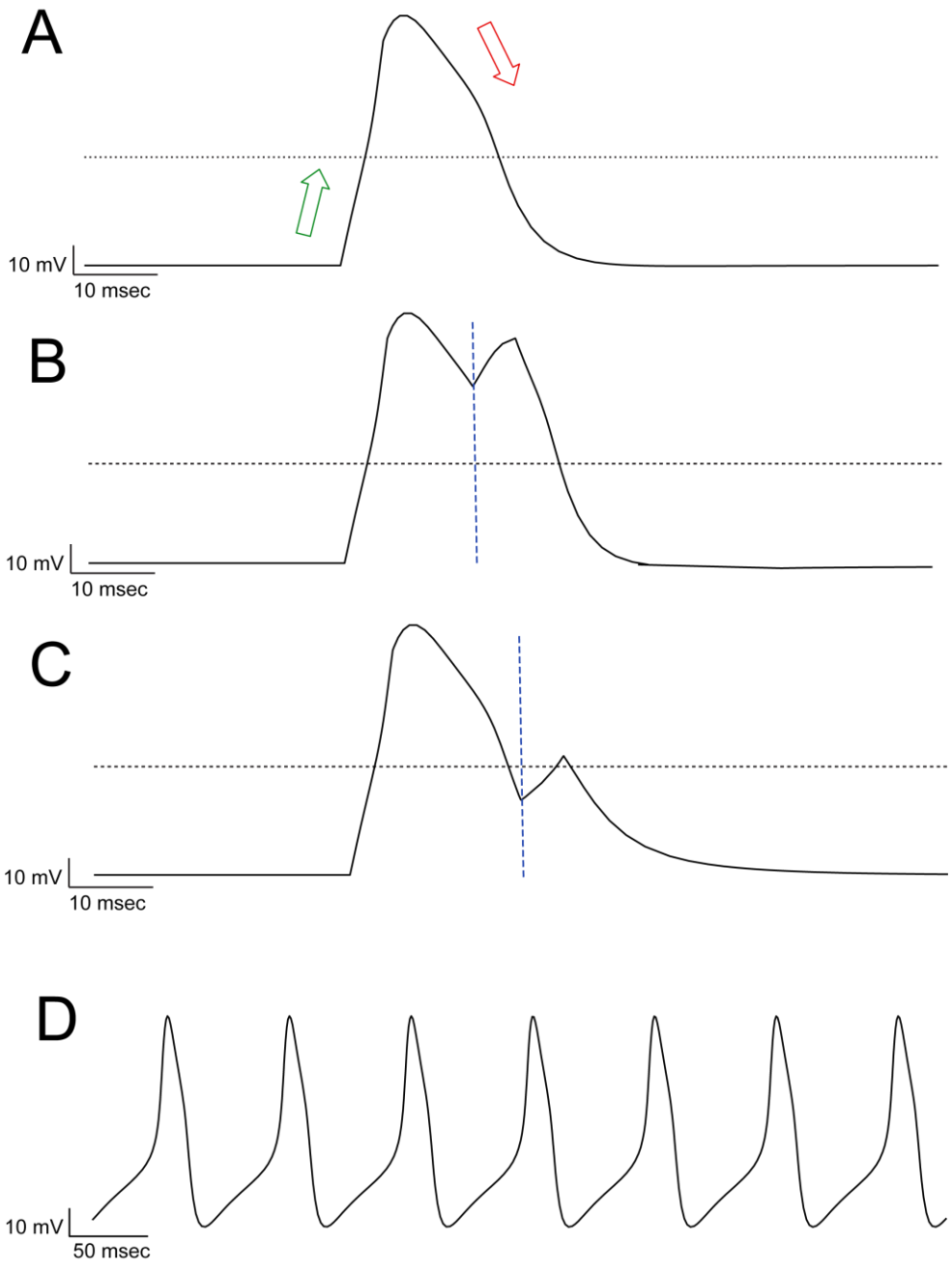

Figure 3.1 Response of the ML model neuron to successive transient current pulses or constant current injection. In Panel A through C, the black horizontal dashed line indicates the threshold of -20 mV; whereas the blue vertical dashed line indicates the time at which the transient current plus is applied. Panel A shows a typical Action Potential (AP) produced by an ML model neuron, the green arrow indicates the excitation phase, and the red arrow indicates a repolarization phase. Panel B & Panel C show either an extended repolarization phase or a threshold-crossing event can occur depending on the

timing when the second transient current pulse is administered. In Panel D, a series of spiking activities can be elicited by applying a background current of 2.5 $\mu A/cm^2$.

lack of an inactivation mechanism, the ML model has no absolute refractory effect. Consequently, the ML model can respond to an input at any phase during excitation and repolarization. In particular, as shown in Figure 3-1 Panel B, the time the ML membrane voltage spends above the threshold is extended when the membrane potential is already above the threshold when the second input arrives, e.g. the repolarization phase is delayed. On the other hand, if the membrane potential is below the threshold but above rest when the cell receives the second input, a threshold-crossing event is triggered. This phenomenon is consistent even if the amplitude of the second input is significantly smaller than that of the first input (Panel C, Figure 3-1). Such dynamics where the electrical profile can be modulated in shape and duration with successive excitation are more akin to the properties of bursting instead of spiking in individual neurons, therefore the notion of the ML model as a characteristic model for the "envelope" of bursting activity. Examples of previous computational works exploiting this property of the ML model include Skinner and Mulloney 1998 and Montejo et al. 2002.

Network Connectivity

The structure of any given networks can be qualified by the network's characteristic path length (L) and clustering coefficient (C). As introduced in Section 2.3, L is calculated as the mean shortest path length between any two neurons in the network; whereas the clustering coefficient C of the network is calculated as the averaged ratio between the number of connections existing within a neighborhood of k neurons and the maximum number of possible connections in the same neighborhood across the entire network. In terms of these two measures, a local regular network is a network exhibiting large C and large L, and a random network is a network exhibiting small C and small L.

In the work presented here, a systematic approach was applied to construct a variety of networks whose structures fall under 3 different characterizations (Newman and Watts 1999). The substrate of such construction is a "neuron ring"

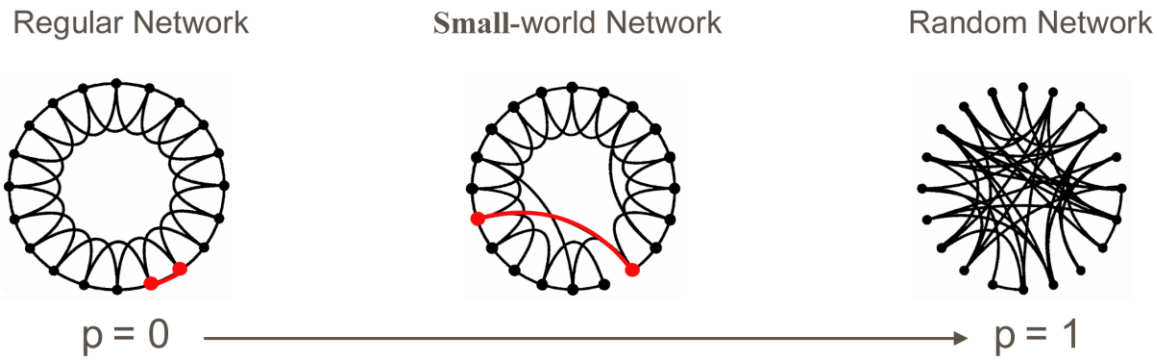

Figure 3.2 Different network topologies as a result of different reconnection probabilities. (Figure adopted from Watts 1999) Starting from a "neuron-ring" (k = 3, leftmost panel), the network structure transitions to the small-world topology and eventually to a random network as the reconnection probability increases. As an illustration to the reconnection scheme, the connection specified in red in the left-most panel was reconnected with probability p to another randomly selected neuron in the population in the middle panel.

(Figure 3-2), where each neuron projects synaptic connections to *k* of its nearest neighbors. Starting from this regular network, a rewiring procedure where each synaptic projection is reconnected with probability *p* to another neuron randomly selected from the network is then implemented. The process is systematically repeated for various values of *p* ranging from 0 to 1. As the value of *p* is increased from 0 in this range, the network topology changes from local and ordered to random at two extremities, with intermediate *p* values resulting in small-world topologies characterized by predominantly local and a few long-range connections (large *C* and small *L*).

Simulation Set-up

A series of networks consisting of 512 ML model neurons arranged as a neuron-ring according to the regular network topology is constructed for this work. In these

networks, the neurons are numbered sequentially from 0 to 511, and the connections between pairs of neurons are purely synaptic with a fixed strength of 0.01 μS. Out of the 512 ML model neurons, 10 consecutive neurons (e.g. neurons numbered 0~4 and 507~511) are injected with a current 2.5 $\mu A/cm^2$. This simulated current injection triggers at the single cell level a periodic firing activity with a frequency at 13.4 Hz (Figure 3-1, Panel D). Heterogeneity is introduced to the network with different initial values for the membrane voltage, the gating variable for the potassium currents, as well as a background noise modeled as a small injected current (normal distribution, mean = 0 $\mu A/cm^2$, $\sigma = 0.66\ \mu A/cm^2$) into each of the model neuron. Other parameters subject to manipulations in this study are *k* (6~20, initial neighborhood size), *p* (0~1, reconnection probability), and *d* (0~3 msec, synaptic delay). Starting from a neuron ring, four different sets of network structures were calculated for each reconnection probability *p*. All simulations were run for 6000 msec, where data from the first 3000 msec are discarded as transient.

3.3 Results

Network-wide bursting in the small-world regime

In this purely excitatory network, the firing pattern changes dramatically as the network topology transits from local, to small-world (small L, large C), and eventually to the random regime (Figure 3-3, Panel a). This transition in network topology corresponds to an increase of reconnection probability *p* from 0 to 1. In the local regime (Figure 3-3, Panel b1), the excitation originates from the pacing neurons and propagates to other neurons along the two halves of the ring. The waves of activities eventually end at the other end of the ring when they collide. This wave of activities has a propagation frequency of 13.4 Hz, which is identical to the firing rate of the pacing neurons (Figure 3-1, Panel D & Figure 3-3, Panel b1). In the small-world regime (Figure 3-3, Panel b2-b3),

a different dynamic emerges where successive waves from the pacemaker nodes propagate with a slightly increased velocity after the initial waves were triggered. The faster activity propagation is a result from the presence of the long-range connections characteristics of the small-world network topology. With these new wave sources, the network becomes increasingly more active until the entire episode of activity ultimately ceases. The duration of the network bursting activity is several times longer than the period of the firing activity of each of the pacemaker nodes, and the mechanism underlying the cessation of each network burst episode is examined in detail in one of the following sub-sections.

The burst period of the network level activities is calculated as the averaged sum of the duration of the episode of activity and the duration of the following episode of quiescence by examining the histogram of spike times. The frequency of the rhythmic network activity is then calculated as both the inverse of the calculated period, as well as the dominant frequency component of a Fast Fourier Transform on the spike-time histogram (bin size = 20 msec). As p increases in the SW regime, the period of the bursting activity decreases (Figure 3-3, Panel b2-b3) while the dominant firing frequency of the neurons increases. When p is further increased, resulting in the transition of the network topology into the random regime (Figure 3-3 Panel b4), all model neurons in the network fire in near synchrony at a frequency approximately 1-3% faster than 13.4 Hz (Figure 3-3, Panel a). The relationship between reconnection probability p and the dominant spiking frequency can be summarized as follows (Figure 3-3, Panel a) – when the network is operating in the small-world regime, the dominant firing frequency drops to a lower value; on the other hand, when the network topology falls either in the local (ordered) or the random paradigm, the dominant firing frequency closely corresponds to that of a single ML model neuron. These phenomena are due to the fact that higher reconnection probability p implies a larger number of long range projections, which allows for faster recruitment of network neurons to fire synchronously.

Synaptic delay supports network-wide bursting activities

In a separate set of simulations, synaptic delay was set to a value between 0~3 msec with 0.75 msec increment for each of the reconnection probabilities *p*. The simulation results are summarized in Figure 3-4 & Figure 3-5. When there is no synaptic delay, no topology-dependent bursting activities exist for any value of *p*. In this scenario, the propagating waves characteristic of a regular topology transition directly into synchronous firing activities in characteristics of the random network. As the synaptic delay is increased above zero, bursting activity starts to emerge in the SW regime. In the scenarios where non-zero synaptic delays are coupled with SW network topologies, the range of *p* that supports bursting activity becomes smaller as the delay increases. When the synaptic delay reaches 2.25 msec, before network-level bursting activities start to emerge, the network exhibits hyperactive firing activities which resemble "seizing" activities, or bursting activities with unusually long burst period, in the small-world regime. In conclusion, synaptic delays have a significant role in maintaining the robustness of the network as larger delays allow for a wider variety of network-level activities. As will be further detailed in the next sub-section, network-level bursting activities in our 512-cell network depend on an intricate balance between the de-synchronization of a silent network through recurrent excitations originating from pace-making neurons receiving constant current injections and the progressive synchronization facilitated by long-range projections. Therefore, only values of synaptic delay greater than zero support network-level bursting activities in the small-world regime. When the synaptic delay equals to 0 (msec), network synchronization is enhanced and the network transits directly into a synchronized firing state in the small-world regime. On the other hand, when the synaptic delay is set to at 2.25 (msec) or 3 (msec), network synchronization is hindered and bursting activities with unusually long period are observed. Consequently, with larger synaptic delays, the hyperactive firing activities

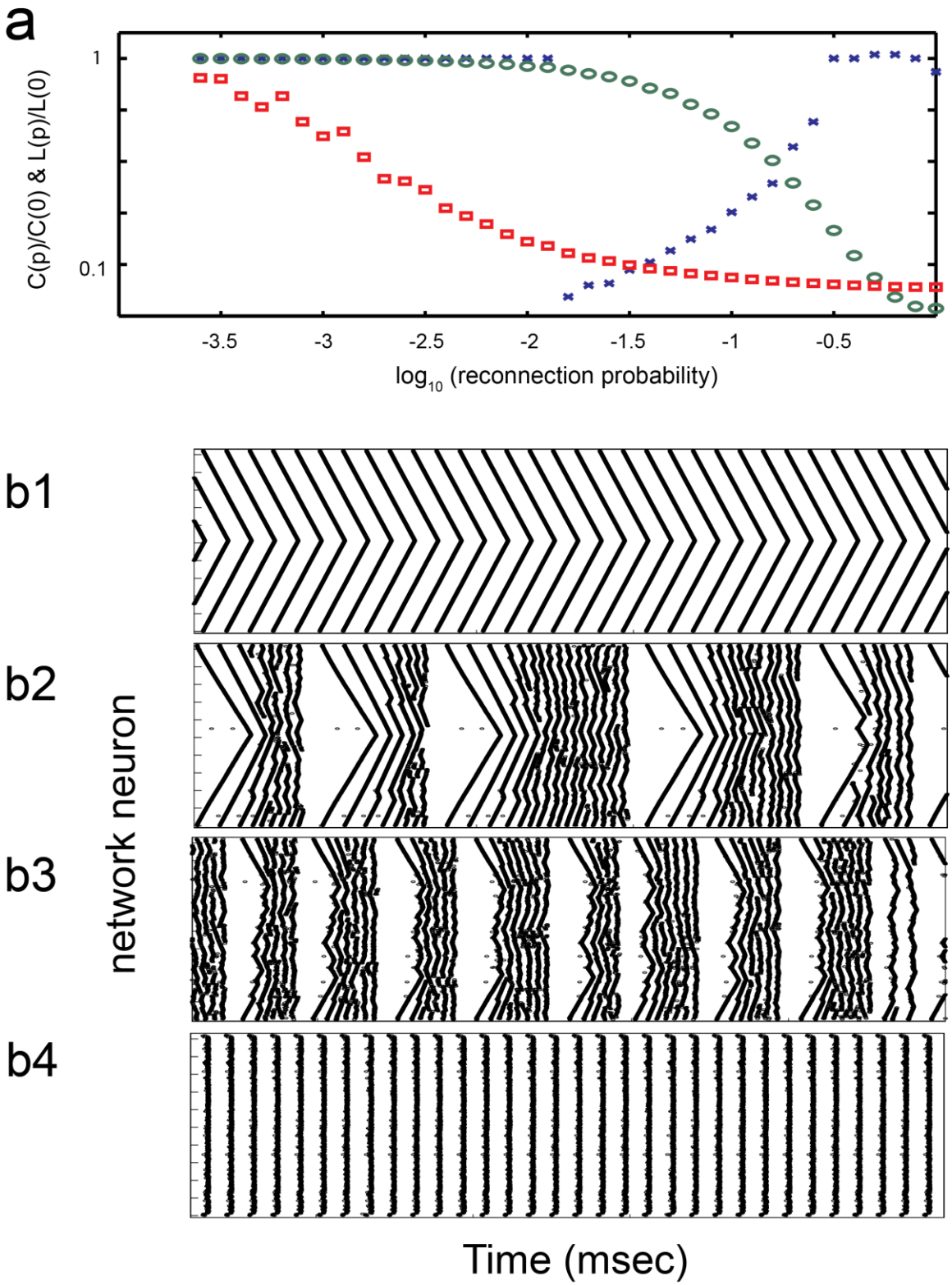

Figure 3.3 Small-world (SW) connectivity leads to bursting in a network of ML models. Simulations performed in NEURON using nominal parameter values for the ML model (Morris

and Lecar 1981) scaled to a whole-cell capacitance based on an arbitrary soma compartment surface area. The 10 pacemaker neurons receive stimulus current of 2.5 µA/cm2. For all simulations, k = 10, d = 1.5 msec, and the synaptic weight = 0.1 µS. Panel a shows the relationship between the reconnection probability p and the following parameters: normalized characteristic clustering co-efficient (C, indicated in green), normalized mean path length (L, indicated in red), and median dominant firing frequency (indicated in blue). Panel b1 through b4 each shows typical network activities corresponding to a particular value of p. These p values are 0, 0.025, 0.079, and 0.794 from top to bottom; plots are raster plots with each black dot indicating a firing event.

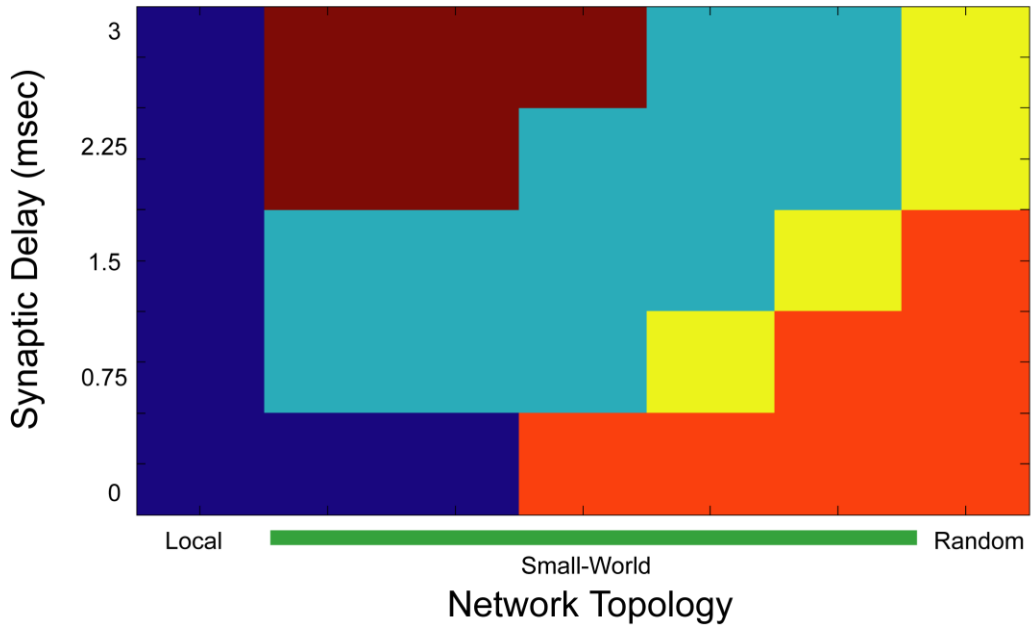

Figure 3.4 Synaptic delay, network topology, and network level activities. This figure demonstrates how network level activities depend on both the synaptic delay and network topology. The green bar signifies the range of small-world network topology. The light blue squares indicate bursting activities, and the yellow squares indicate a mixture of bursting and near-synchrony firing activity. The color brown indicates where hyperactive activities were observed, and the color dark blue indicates network-level activities characterized by propagating waves. Finally, the color orange indicates network-level synchronous firing activities. When synaptic delay is zero, no bursting activities exist regardless of the network topology. As the synaptic delay increases beyond zero, bursting activities (light blue) start to emerge in the small-world regime. For example, when the synaptic delay equals to 1.5 msec, network activities transition from propagating waves (dark blue) to bursting activities (light blue), then to a mixture of bursting & synchronized firing activities (yellow), and eventually to synchronized firing activities (orange). When the value of synaptic delay is large (e.g. 3 msec), hyper-active activities (brown) emerge in the small-world regime before any bursting activities can be observed.

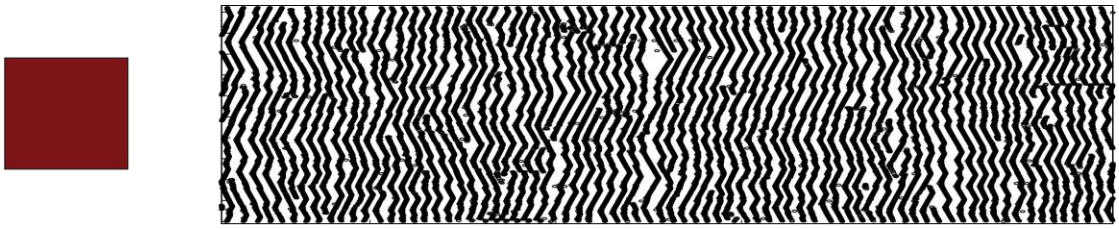

"Seizing": hyperactive network-state,
e.g. bursting with unusually long burst period

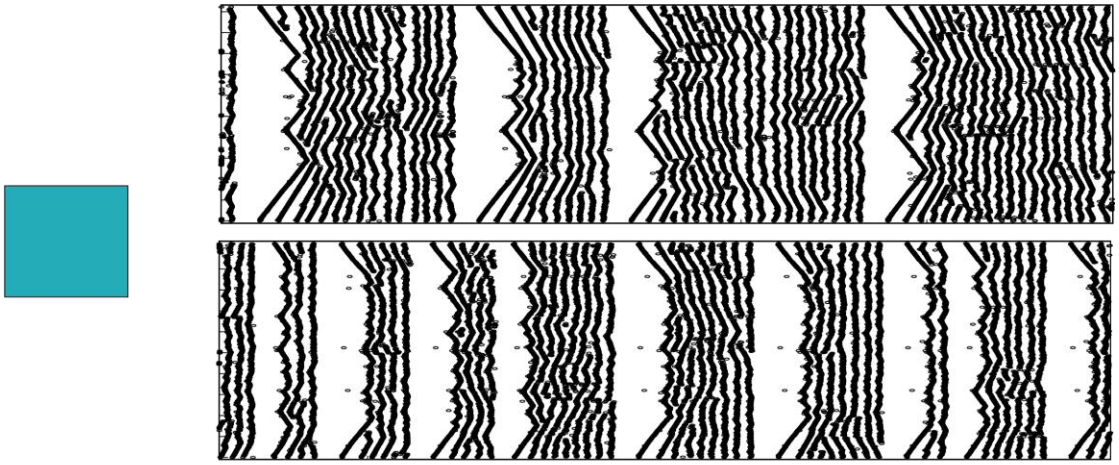

"Bursting": top portion: p = 0.063;
bottom portion: p = 0.126

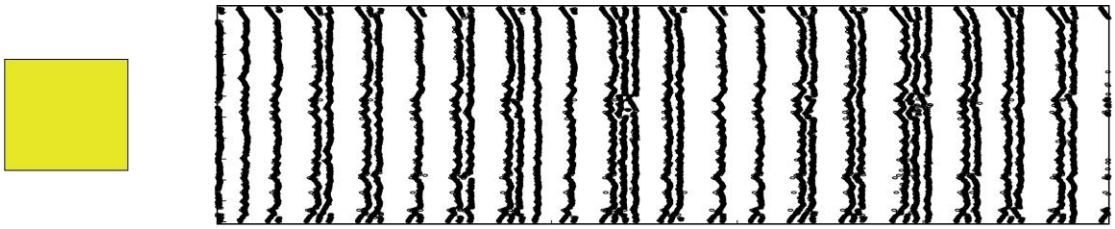

A mixture of bursting and
near-synchrony firing activities

Figure 3.5 Examples showing the relationship between network-level activities in the SW regime and synaptic delay. This figure demonstrates how network-level activities transition from "hyperactive" (e.g. "seizing"), to bursting, and to a mixture of bursting and near-synchrony firing activities in the SW regime. The synaptic delay is set to 2.25 msec, and the color-coding corresponds to that used in Figure 3-4. From top to bottom, the reconnection probabilities are 0.031, 0.063, 0.126, and 0.251.

occur in the small-world regimes achieved with lower values of *p* (Figure 3-5), since higher values of *p* indicate more long-range projections that facilitate network synchronization. In conclusion, the faster the network components synchronize their activities, the faster the burst terminates (e.g. shorter period), and this concept will be further examined in the next sub-section.

An increase in synchrony causes burst termination in the absence of refractory period

As introduced previously, a "burst" consists of an episode of spiking activities followed by a quiescent episode. The last part of this work focuses on investigating how such quiescent episode come to be when at the single cell level, there is no slow mechanism directly contributing to the refractory period that causes the neuron to enter the refractory state.

Two examples of typical bursting activities facilitated by SW network topology are shown in Panel a2-b2 in Figure 3-6. Within each burst, the network synchronization level varies within a range and eventually increases to a local maximum. This phenomenon is demonstrated in Panel a1-b1 in Figure 3-6, where the synchronization level is calculated as the size of a time window preceding a specific time point during which a population-wide activity event has occurred, e.g. 85% of the population fires at least once. By this definition, a smaller time window implies a more synchronized network state, while a larger time window implies a less synchronized network state. This measure was relatively insensitive to the choice of population percentage threshold to claim population wide activity had occurred, for similar results were obtained with values from 70% to 95%.

For further investigation of the relationship between network synchronization level and burst termination, a separate set of simulations was designed. In these simulations, a stimulus whose amplitude is just sufficient to generate a single action

potential was administered at a randomly generated time to each neuron during a specified time window. This random delivery of stimuli was drawn from a uniform

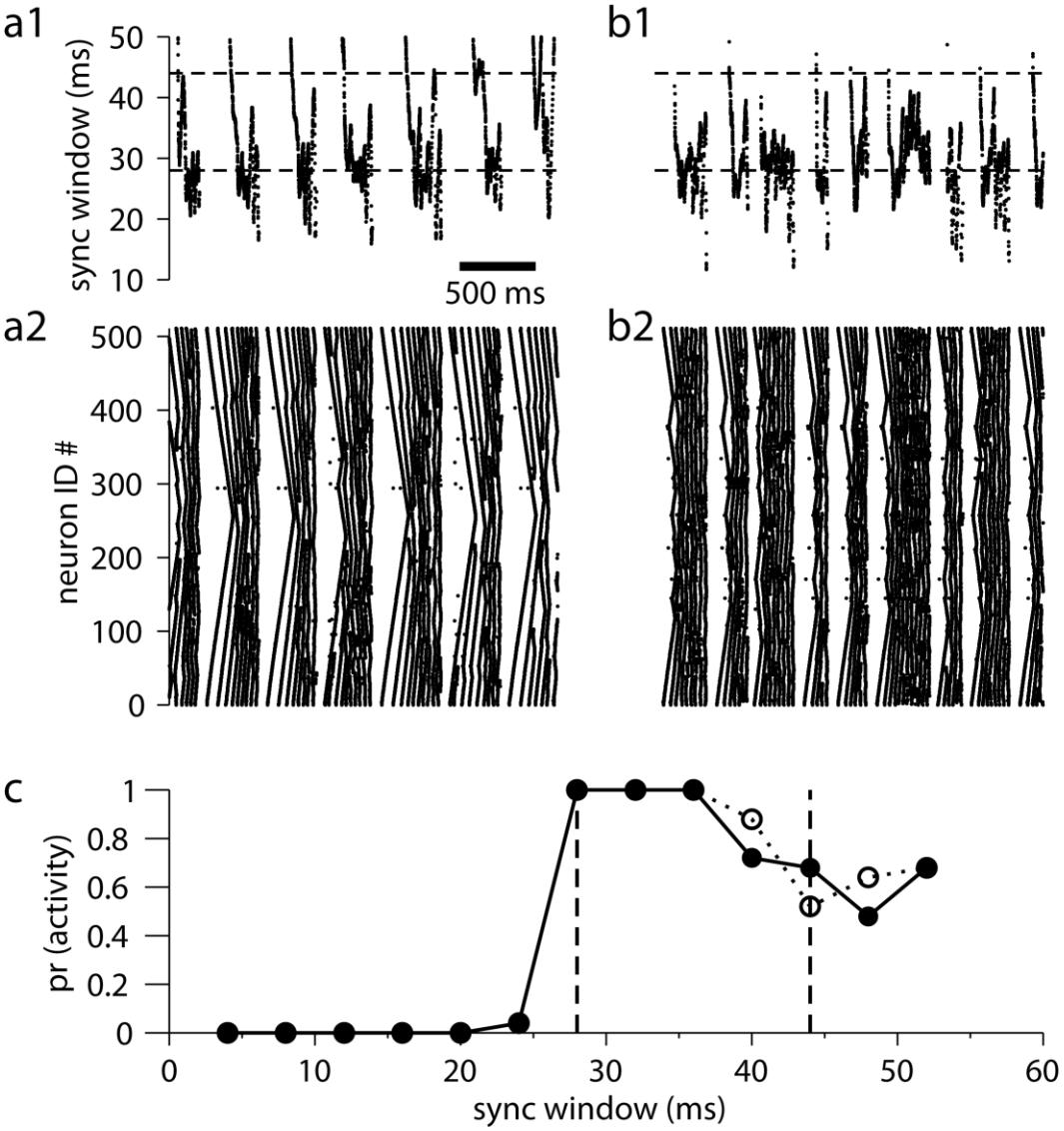

Figure 3.6 Progressive synchronization during a burst, and associated probability of bursting given a certain set of initial synchrony condition. Time-varying synchronization measures (shown in a1/b1) associated with the simulations shown in a2/b2, with p values of 0.0316 (a1, a2) and 0.0631 (a2, b2) respectively. Synchronization at each given time is measured by the time window preceding the reference point during which 85% of the neuron population fires at least once. Panel c illustrates the probability of self-sustained burst from equilibrium conditions given an initial level of synchronized network-wide firing (closed circles and open circles represent p = 0.0361 & 0.0631 respectively). The dashed lines at 28 and 44 msec are also shown in panel a1/a2 for reference.

distribution and applied to the network initially in a quiescent state. When an initial quiescent condition is imposed, the probability of post-stimulus activity is maximized when the initial stimulus is applied within a specific time window. This optimal time window ranging from 28 to 44 is indicated in Panel C in Figure 3-6.

This optimal time window is specified as the two dashed lines in Panel a1-a2 of Figure 3-5, within which the majority of intra-burst spiking activities occur. In addition to a general trend of increasing synchrony (decreasing synchronization measure) toward the end of each burst, the bursting activity terminates as the network activity becomes highly synchronous, e.g. when the synchronization measure eventually falls outside the time window of 28-42 msec. Based on these observations, we can conclude that in the SW regime, burst initiation is due to the initial firing of pacemaking nodes and recurrent excitation within the network. Burst termination, on the other hand, can be attributed to an increase in the level of synchrony in the network beyond which a self-sustained burst is unlikely.

3.4 Summary

In the project presented in this chapter, the influence of network topology over the output of the neural network is investigated. The transitions in network level activities presented here are also observed in other topology-dependent activity variation studies where the component model neuron is of the canonical form, e.g. an integrate-and-fire or Hodgkin-Huxley model (Netoff et al. 2004). The values for synaptic delay used in Netoff et al. 2004 were set at 2.8~3.7 msec; therefore, the small-world topology in their study supports hyperactive behavior (e.g. seizing) similar to what we observed here with longer synaptic delays. Consequently, a distinct transition of network activity to rhythmic burst occurs at higher values of *p*, where the topology is considered to be between the small-world and the random structure. Factors other than the level of synaptic delay which might contribute to differences in observations can also include the fundamental

differences in the component neuron as well as the size of the simulated network. In another set of simulations (results not shown), we have observed that with all else is held equal, the minimal reconnection probability *p* which results in a SW topology facilitating network-level bursting activity increases when the size of the ML network is increased.

There are many neural systems where SW connectivity is likely to be present (Boersma et al.; Gong et al. 2009; Wright and Butera 2006; Yan et al. 2010), and it is speculated that the mechanisms elucidated in this project may foster slower neural rhythms with time-scales that currently cannot be accounted for by the time constants of voltage-gated, calcium-activated, or other synaptic-kinetic mechanisms. The input-output properties of the ML model are not esoteric; if one interprets the ML model as a generic measure of neural activity, the response of the ML model to input during the active phase is remarkably similar to the response of endogenously bursting neurons (e.g. ML as a model of the envelop of bursting activity). Therefore, the results derived from this project have the implication in issues such as how endogenously bursting neurons, regardless of the mechanisms underlying their pacemaking properties, may contribute to maintaining network rhythms much slower than the bursting activities at the level of isolated neurons. This observation is especially interesting and relevant to the ultimate goal of the work presented in this document, as the pre-Bötzinger complex in the transverse slice respiratory circuitry has been shown to contain multiple types of pacemaking neurons working collectively to generate rhythmic PBC region output (Thoby-Brisson and Ramirez 2001).

4. INTER-NEURON COUPLING DEPENDENT NETWORK-LEVEL PHENOMENA[2]

4.1 Abstract

Important physiological functions, which often manifest at the time scale of seconds or more, are initiated, controlled and monitored by neuron networks. On the other hand, the function of a given neuron network is governed partially by inter-neuron interactions that occur at a drastically different time scale. Adhering to the objective of investigating emergent excitatory network phenomena, the work presented in this chapter focuses on how changes in the type and strength of coupling among two or more neurons at the millisecond time scale can manifest at another time scale orders of magnitude apart (Figure 3.1).

In addition to elucidating the mathematical yet physiologically significant relationship between processes occurring at drastically different time-scales and different structural levels, the research presented here also provides possible explanations for the effects of gap-junctional coupling in the output of respiratory transverse slice preparation (Bou-Flores and Berger 2001). The work also serves as a basis for further explorations of the fine balance between multiple excitatory effectors (e.g. multiple neurotransmitters) concurrent in neuronal population in vivo (Doi et al. 2009; Zanella et al. 2009).

[2] The work presented in this chapter has been submitted to Journal of Computational Neuroscience as a paper and is currently in the 3rd round of review process. The author of this document is the first author of the aforementioned paper in review. The portion of the work presented in this chapter investigating the effects of varying Ggap while fixing Gsyn in the paired-cell scenario was originally conducted by the third author of the paper. The metric proposed in this work categorizing different burst solutions was contributed by the second author Natalia Toporikova. The author of this document is independently responsible for all other work presented in this chapter except otherwise clarified.

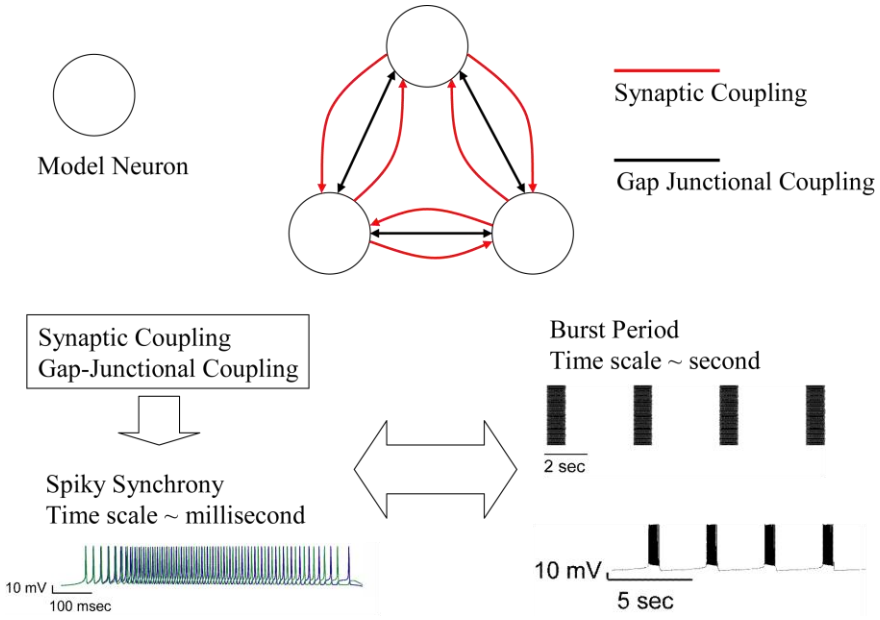

Figure 4.1 Effects of synaptic and gap-junctional couplings at different time scales. The couplings effect spike synchrony at the millisecond time scale, and also have effects on the burst period at the second time scale. The synaptic coupling has a time constant of 5 msec, and the gap-junctional coupling modeled as a simple electrical resistor takes effect immediately.

4.2 Methods

The simulation studies are performed on networks of single neuron model published previously (Purvis et al. 2007). The network contains either 2 or 50 such neuron models, and the model neurons are connected to each other with all-to-all excitatory synaptic coupling (Butera et al. 1999a; Purvis et al. 2007) and electrical coupling, which is modeled as a simple resistor. Values of electrical and synaptic coupling are specified where needed; otherwise, nominal parameter values were adopted from previous work.

All simulations were run for 160 seconds of simulation time. To eliminate initial transient network activity, results from the first 60 seconds of all simulations were discarded. The simulations were performed in NEURON. In addition, a subset of the paired-cell network set-up was subject to quasi steady state non-linear bifurcation

analysis using XPP AUTO. Resulting data from all simulations was analyzed using customized MATLAB scripts. The purpose of these MATLAB analyses is to extract features which can serve as a platform for comparison between phenomena observed at different time scales. The two features extracted from these network simulations are network burst period (Panel A, Figure 3-1) and intra-burst spike synchrony (Panel B, Figure 3-1).

SDI – Quantifying phenomena occurring at the millisecond time scale

When analyzing intra-burst spike synchrony, a Spike Deviation Index (SDI) was used to calculate the degree of spike-level alignment in firing times. One neuron is first selected as the reference, and for each spike produced by the reference neuron, the time interval between the spike and the closest spike, either forward or backward in time, produced by another neuron within the same burst is identified. $T_{closest\text{-}spike}$ for the reference neuron is then calculated as the averaged value of the aforementioned time intervals identified for every single spike produced by the reference neuron within a single burst. Repeating the same calculation over the entire neuron population, the SDI is defined as the standard deviation of all the $T_{closest\text{-}spike}$ values identified for all neurons in the population (N = 50).

The calculation of SDI can be summarized by the following equations. If N1 is defined as the number of spikes within a single burst, and N2 is defined as the number of bursts recorded from the same neuron (neuron x) from the population, then:

$$T_{\text{Nth burst}} = \{ \sum_{\text{all spikes}} [\min(| \text{spike-time(neuron x)} - \text{spike-time(neuron y, } y \neq x) |)] \} / N_1$$

$$T_{\text{closest spike, neuron x}} = [\sum_{\text{all bursts of neuron x}} (T_{\text{Nth burst of neuron x}})] / N_2$$

$$SDI = \sigma (T_{\text{closest spike of neuron 1}}, \ldots, T_{\text{closest spike of neuron x1}}, \ldots T_{\text{closest spike of neuron 50}})$$

where σ is the standard deviation.

This SDI metric was not intended to be a rigorous definition of spike-level synchrony, but rather to easily distinguish at a population level in-phase synchrony (SDI

is near 0) from splay-phase synchrony (SDI is on the order of many milliseconds), which is analogous to anti-phase synchrony in the two-neuron case.

4.3 Results

As stated in the Methods section, the two types of inter-neural couplings of interest here are the synaptic (chemical) coupling and the gap-junctional (electrical) coupling. The link between manifested electrical profiles observed at different time scales is established by examining the relationship between network burst period (on the time scale seconds) and intra-burst spike synchrony (on the time scale of milliseconds). The structure of the discussion in the following subsections is summarized as follows. Using a 50-cell simulated neural network as the substrate, the effects of varying the two types of coupling strengths respectively on network-level electrical profiles are examined. The investigation then moves to examining simulation results from paired-cell networks. With qualitatively identical manipulation of the two coupling strengths, consistency in changes of electrical profiles in both the 50-cell and the paired-cell settings suggest similar underlying mechanisms. These mechanisms are further examined in using bifurcation analysis. In addition to emphasizing the physiological significance of the work presented, the project concludes with the introduction of a metric that connects changes in electrical profiles with changes in bifurcation landscape.

50-cell network: Coupling strengths alter burst period and spike synchrony within the burst

In a 50-neuron network, varying gap-junction and synaptic coupling strengths produces two effects that occur at two different time scales orders of magnitude apart. The faster millisecond time scale corresponds to that at which each individual neuron spikes, and the slower second time scale corresponds to that at which network-level bursting activity manifests (Figure 4-1). At the level of network bursting activity, for a

given value of excitatory synaptic conductance (G_{syn}), increasing the strength of gap-junction coupling (G_{gap}) from zero causes the network burst period to increase (Figure. 4-2B1 through 4-2B3). However, beyond a critical G_{gap} value, termed $G_{gap\text{-}p\text{-}critical}$ (Figure. 4-2B3, 4-2B4), the network burst period quickly decreases and remains nearly unresponsive to further changes in coupling strengths.

Increasing the value of G_{syn} while fixing the value of G_{gap}, on the other hand, causes an abrupt increase followed by a gradual decrease in the SDI measure (Panel D, Figure 4-2). In the parameter space examined, the decrease in the SDI measure never reaches to the value characterizing in-phase spiking activities (Panel F1-F3, Figure 4-2). This phenomenon is accompanied by an abrupt change in the network burst period (Panel A, Panel C1-C3, Figure 4-2). The abrupt increase in network burst period occurs at the same level of G_{gap} where the switch in spike synchrony occurs (Panel A & D, Panel C2 & F2, Figure 4-2); however, the burst period continues to increase unlike the decreasing trend in the SDI measure following the abrupt change. These observations are robust across a broad range of the parameter space (Panel A & D, Figure 4-2).

To summarize, while fixing G_{syn}, $G_{gap\text{-}p\text{-}critical}$ corresponds to the value of G_{gap} at which the effect of increasing G_{gap} on the burst period reverses. Similarly, $G_{gap\text{-}s\text{-}critical}$ corresponds to the value of G_{gap} at which the effect of increasing G_{syn} on the spike synchrony (SDI) within each burst reverses. In addition, for the simulation settings specific to our study, they ($G_{gap\text{-}p\text{-}critical}$ & $G_{gap\text{-}s\text{-}critical}$) both have the value of 1.75nS when G_{syn} is fixed at 2 nS. As will be further described in section 3.2, $G_{gap\text{-}p\text{-}critical}$ and $G_{gap\text{-}s\text{-}critical}$ turns out to be identical for any fixed level of G_{syn}.

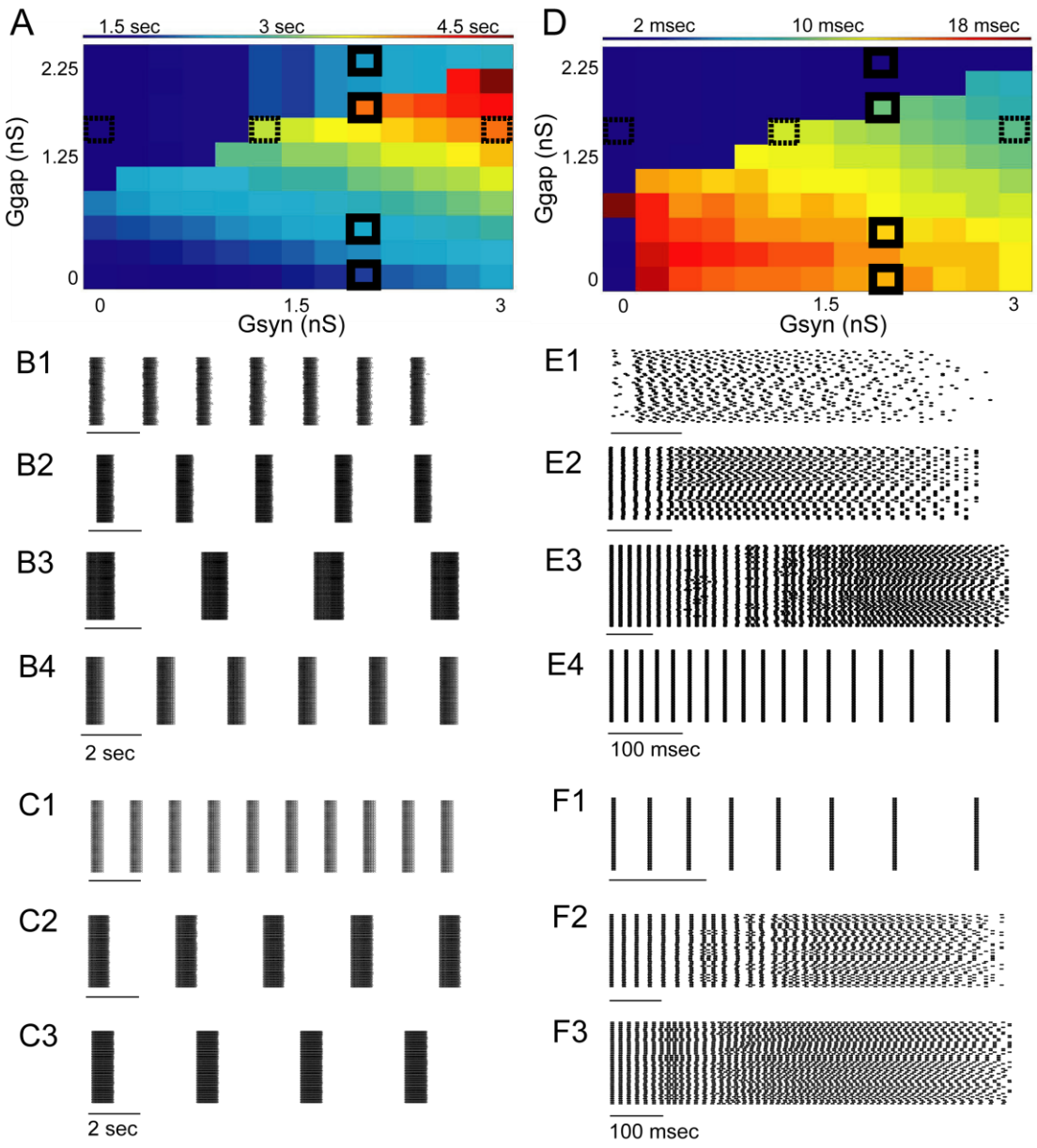

Figure 4.2 50-cell: effects of Ggap and Gsyn on burst period and spike synchrony. The burst period is color-coded in Panel A, and the Spike Deviation Index (SDI) characterizing spike synchrony is color-coded in panel D. The calculation of SDI is described in the Methods section. Panels B/E are raster plots of several periods of bursting (B) and a single burst (E) within the network for 4 sets of coupling parameters indicated by the solid black boxes in panels A/D; the parameter sets are: Ggap = 0, 0.5, 1.75, and 2.25 nS, with Gsyn fixed at 2 nS. Panel C/F contain the same information for another 3 sets of coupling parameters indicated by the dashed black boxes in panels A/D; these parameters are: Gsyn = 1.5 nS, with Ggap = 0, 1.25, and 3 nS.

Unlike the cases where G_{syn} is kept fixed with varying values of G_{gap}, we do not observe the type of complex thresholding phenomena when varying values of G_{syn} are coupled with a fixed value of G_{gap}. For each fixed value of G_{gap}, the burst period abruptly increases as G_{syn} is increased beyond a critical value ($G_{syn\text{-}critial}$, Panel C2 in Figure 4-2). Furthermore, unlike the case where varying G_{gap} is coupled with a fixed G_{syn} (Panel B3, Figure 4-2) where both increased burst duration and recovery time together contribute the observed increase in burst period, the increase in burst period here is predominantly due to a lengthening in the recovery time of the burst. At the same critical value of G_{syn}, the model neurons transition into asynchronous spiking, e.g. anti-phase activities (Panel F2-F3, Figure 4-2) and never return to the synchronous, e.g. in-phase spiking states (Panel F1, Figure 4-2). As will be examined in later sections, the difference stems from the interactions of different solution-branches in a changing bifurcation landscape.

Paired-cell network: Effects similar to those observed in 50-cell network on burst period and spike synchrony suggest similar underlying mechanism.

In Figure 4-3, the six panels illustrate typical paired-cell simulation results observed from varying the strengths of couplings between two model neurons. Each of these six panels has three portions. The top portions are dedicated to illustrating the time series membrane voltage data from paired-cell simulations. The progression of intra-burst spiking synchrony is highlighted in the middle portions of these panels. Lastly, the bottom portions correspond to results derived from non-linear bifurcation analysis. Panel A through Panel C represent results from simulations with a fixed G_{syn} and varying G_{gap} values; whereas Panel D through Panel F represent results from simulations with a fixed G_{gap} and varying G_{syn} values. Overall, systematically varying G_{gap} and G_{syn} in the paired-cell scenarios yield results that are qualitatively similar to that from 50-cell network simulations.

With a fixed G_{syn}, the paired model neurons cannot maintain in-phase synchronous spiking activities when the burst period increases with G_{gap} (Panel A & B, Figure 4-3). On the other hand, when the burst period decreases with further increases in G_{gap} (Panel C, Figure 4-3), the two neurons are firing identically with synchrony. As shown in middle portions of Panel A-C, the burst initially starts with the two neurons firing synchronously; however, this state is not stable and is lost within the first few action potentials of the burst. In general, in the simulated paired-neurons, a larger value of G_{gap} (Panel B Figure 4-3) does allow the model neurons to maintain transient in-phase synchronous spiking activities for a longer fraction of the burst duration than smaller values of G_{gap} (Panel C, Figure 4-3).

Briefly summarizing, in the paired-neuron scenario, the spike synchrony within a burst transitions from in-phase synchronous to anti-phase asynchronous spiking activities when the $G_{gap} < G_{gap\text{-}p\text{-}critical}$. From now on, this mode of bursting activities where intra-burst spike synchrony transitions from synchronous to asynchronous is characterized as anti-phase spike bursting (**ASB**). Whereas when $G_{gap} >= G_{gap\text{-}p\text{-}critical}$, the spiking activities from the paired model neurons remain synchronous throughout the burst, and this mode of bursting is characterized as in-phase spike bursting (**ISB**, synchronous spiking throughout a burst). In addition, since $G_{gap\text{-}p\text{-}critical}$ corresponds to a change in spike synchrony as the value of G_{gap} is varied, i.e. $G_{gap\text{-}p\text{-}critical} = G_{gap\text{-}s\text{-}critical}$, they will be referred to collectively as $G_{gap\text{-}critical}$. For the purpose of clarification, the naming convention is detailed in Table 4-1.

Table 4.1 Bursting Mode Characterization.

Bursting Mode Characterization	
Anti-Phase Spike Bursting (**ASB**)	In-Phase Spike Bursting (**ISB**)
Synchronous in-phase (**IP**) spiking activities transition to asynchronous anti-phase (**AP**) spiking activities within a burst	Synchronous in-phase (**IP**) spiking activities are maintained throughout a single burst

Panel D through F of Figure 4-3, together with the highlighted Row A in Figure 4-4, illustrate the results obtained when a fixed G_{gap} is coupled with varied values of G_{syn} across an appropriate region of parameter space. As derived similarly from its counterpart in 50-cell simulations, increasing G_{syn} while fixing G_{gap} results in a loss of in-phase synchronous spiking activities earlier within a burst (middle portions of Panel D through F, Figure 4-3) along with an increase in burst period (top & middle portions of Panel D through F, Figure 4-3). The complex thresholding phenomena observed while varying G_{gap} with a fixed G_{syn} are not observed here.

The effects described so far are spike mediated. In a two-neuron network without spiking currents (i.e. just a sub-threshold oscillation), manipulation of G_{gap} or G_{syn} has a negligible effect on period (results not shown). The key conclusion from both the network level and the paired-neuron simulations is that manipulation of spike-level synchrony ultimately alters the burst dynamics. Furthermore, this conclusion, along with the characteristics of ASB and ISB activities, persist as the time constant of the chemical synapse is decreased to one-tenth of the original value (results not shown). The paired-cell simulation set-up enables a more in-depth treatment using numerical bifurcation analysis. The next two subsections focus more on the application of quasi-steady state bifurcation analysis on results from simulation scenarios where varying values of G_{gap} are coupled with a fixed value of G_{syn}. Results from such treatment on cases where G_{syn} is varied while keeping G_{gap} fixed will be discussed in comparison when appropriate.

Transition between ASB and ISB

The quasi-steady state bifurcation analysis of the paired-cell model is used to understand the dynamical mechanisms accounting for the transition between ASB to ISB as G_{gap} and/or G_{syn} is varied. The variable h is treated as the slow time-scale bifurcation parameter is the fast-slow decomposition. This variable h accounts for the slow inactivation of an excitatory (depolarizing) persistent sodium current (I_{NAP}) in our neuron

model. It is responsible for frequency adaptation and the cessation of spiking activity once a burst has been initiated (Butera et al. 1999a). Analyzing the paired-neuron model under quasi-steady state conditions is reasonable for analyzing the dynamics of bursting (Bertram et al. 1995; Izhikevich 2000; Rinzel 1985), since we are only studying the activities of the paired neurons at the time-scale of bursting. This form of analysis and the qualitative features of the single neuron and two-neuron bifurcation diagram are comparable to previous studies of so-called square-wave bursters for both single cells as well pairs of coupled cells that have considered electrical coupling (De Vries et al. 1998; Sherman 1994).

As a prelude to the detailed treatment in the following two subsections, the structure of the summarizing Figure 4-3 is provided again as follows:

The bottom portions of Panels A through F in Figure 3.3 demonstrate the results from utilizing the quasi-steady state bifurcation analysis on the paired-cell simulations. In Panel A through C, the value of G_{syn} is fixed; whereas in Panel D through F, the value of G_{gap} is fixed. The value of G_{syn} in Panel A through C is fixed at 3 nS, with the values of G_{gap} being 0, 0.5, and 1.5 nS respectively. For simulations in Panel D through Panel F, the value of G_{gap} is fixed at 0.7 nS, while G_{syn} are 0.75, 1.5, and 3 nS respectively.

From ASB to ISB: Effects of Varying G_{gap} while Fixing G_{syn}

As shown by De Vries et al. 1998 and Sherman 1994, we also observed two sub-critical Hopf bifurcations in our paired-cell models. Emanating from each of the Hopf bifurcations are two periodic solution branches referred to here as the anti-phase (**AP**, red) and the in-phase (**IP**, black) solution branch. Each of these two solution branches corresponds to the anti-phase and in-phase spiking activities respectively. When there is no electrical coupling (Panel A, Figure 4-3), the two periodic solution branches are nearly identical in location and both periodic branches emanate from Hopf bifurcations in the increasing h direction with unstable periodic orbits. At their respective limit points

(saddle nodes of the periodic solutions), the AP period branch reverses its stability twice and IP period branches reverse its stability once, and both continue in the decreasing h direction until terminating at the equilibrium solution branch (Figure 4-4, bottom portion of Panel A). In this case when G_{gap} is zero (G_{syn} = 3nS), the AP branch is stable and the IP branch is unstable in the range of h where bursting occurs. When G_{gap} is greater than zero, the AP and IP solution branches become distinct and exist at different but overlapping intervals of h (Panel B, Figure 4-3). Furthermore, a z-shaped curve bifurcates from the slow manifold resulting in a set of asymmetric steady-state (ASS) solutions upon which the periodic solutions terminate, in a manner similar to that presented in previous work (Sherman and Rinzel 1992).

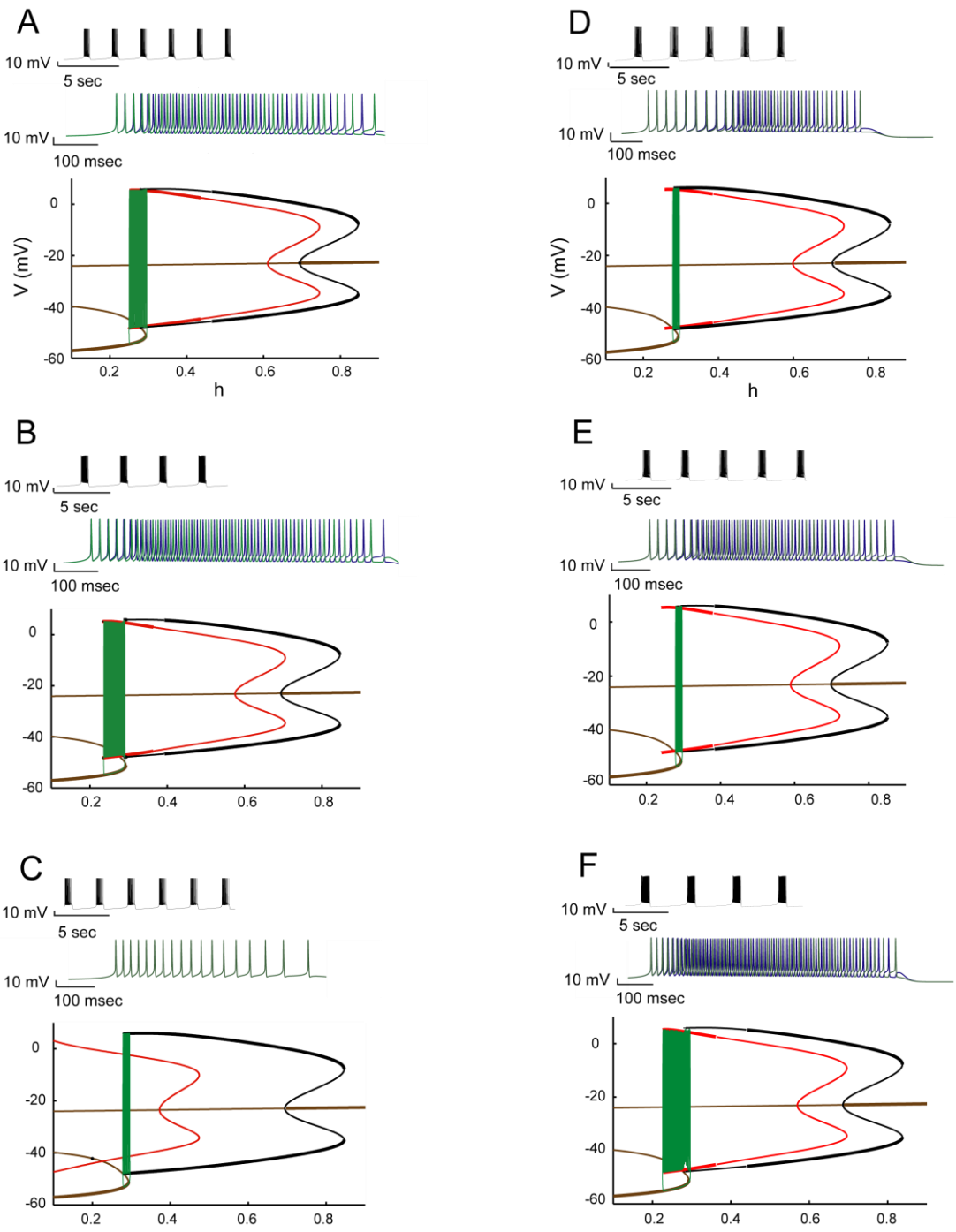

Figure 4.3 Paired-cell: Effects of Gsyn & Ggap on burst period and spike synchrony. (IP: black. AP: red. Bursting trajectory: green. Steady State Solution: brown.) Example results from two-neuron network simulations. From top to bottom, Panels A-C illustrate the simulation results when Gsyn is fixed at 3.0 nS, and Ggap = 0, 0.5, and 1.5 nS. Similarly, Panels D through F illustrate the results when Ggap is fixed at 0.7 nS, and Gsyn is varied from 0.75, 1.5, and 3 nS. From top to bottom, insets in each panel sequentially highlight the change in burst period, the detailed spiking profile that occurs within each

burst, and the results from non-linear bifurcation analysis. Specific to the quasi-steady state non-linear bifurcation analysis, the x-axis represents the slow bifurcation parameter h, and the y-axis represents membrane voltage. The trends in burst period and intra-burst spike synchrony are similar to those observed in network simulations illustrated in Figure 4-2.

As G_{gap} increases, the entire AP solution branch and associated Hopf bifurcation shifts to lower values of h, while having no effect on the stable equilibrium solution or the location of the IP branch. For low to intermediate levels of G_{gap} (Figure 4-3 Panel A & B, bottom portions), a growing continuous region of the AP branch loses stability. Correspondingly, the IP periodic branch gains stability over a larger range of h. For example, in the bottom portion of Figure 4-3 Panel B, there is a brief initial interaction of the burst trajectory with the IP solution, but the bursting trajectory converges to the AP spiking solution. As G_{gap} is further increased to large values (Figure 4-3 Panel C, bottom portion) the bursting trajectory lies entirely on the IP periodic branch during the spiking phase. At this point the AP periodic branch is at all points unstable, while the IP periodic solutions are stable.

Taken together with the previous section, these results suggest that an increase in G_{gap} promotes a transition from anti-phase spiking activities to in-phase spiking activities. As G_{gap} is increased, periodic solutions corresponding to AP lose stability, while periodic solutions corresponding to IP gain stability.

From ISB to ASB: Effects of Varying G_{syn} while Fixing G_{gap}

The bifurcation landscape remains quite similar in cases where varying G_{syn} is coupled with a fixed value of G_{gap}. As shown in Panels D through F in Figure 4-3, the AP branch remains stable in the range of h where bursting occurs regardless of the change in the value of G_{syn}. However, as G_{syn} increases, the IP branch loses stability from the left (Figure 4-3 Panel D2 Panel F2, bottom portions), while AP branch remains stable with extended stability into the lower h region (highlighted row in Figure 4-4).

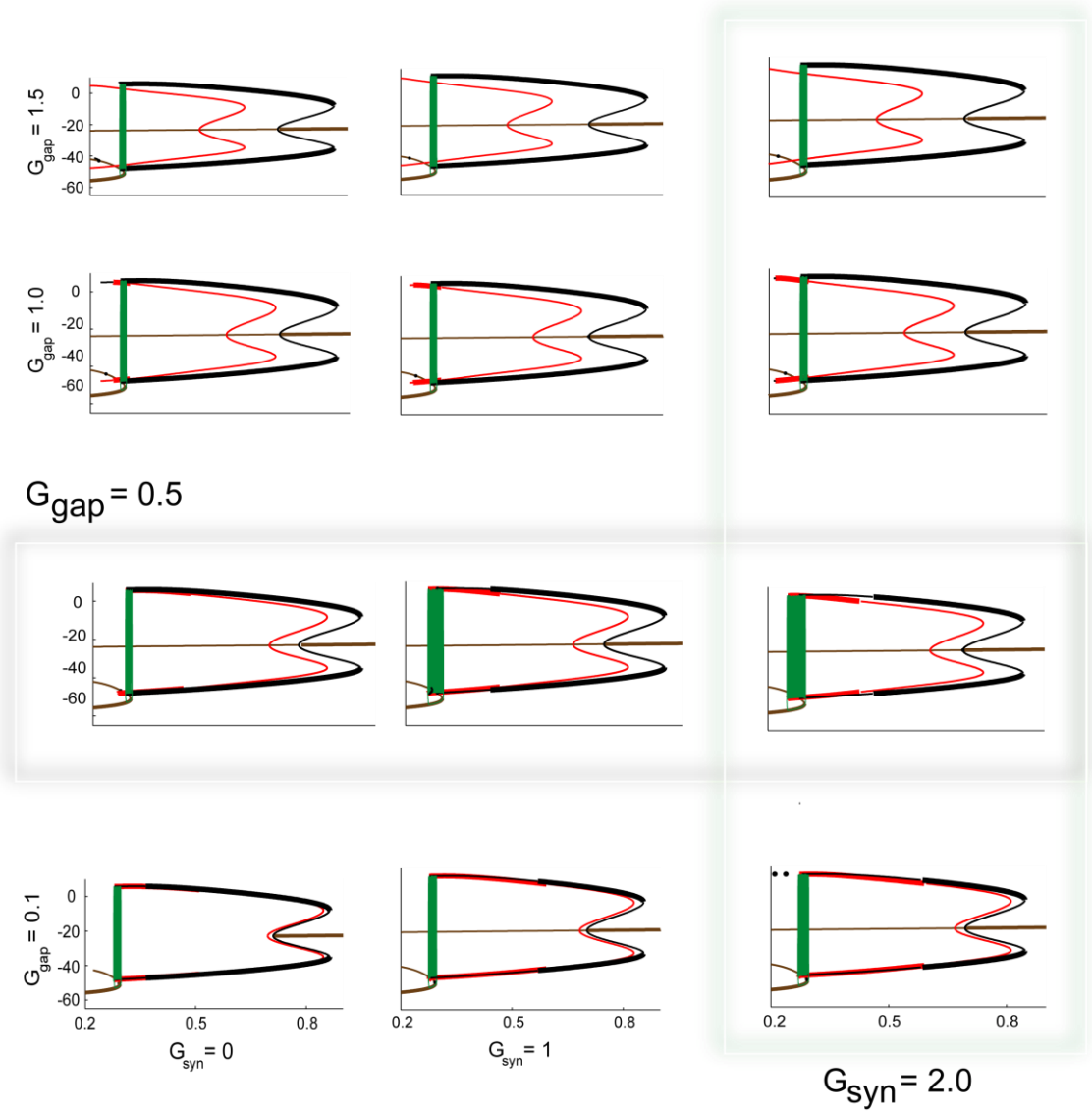

Figure 4.4 Detailed profiles of the bifurcation diagrams where synaptic and gap-junctional coupling strengths (nS) are varied. The coupling strengths are as follows: Gsyn = 0, 1, 2 nS and Ggap = 0.1, 0.5, 1, 1.5 nS. In each panels, the x-axis is h (inactivation parameter for persistent sodium current), and the y-axis is the membrane voltage (mV). The highlighted row and column is representative of the convergence behavior of the bursting trajectory, as well as the changes in the two periodic solution branches AP (red) and IP (black).

For the viable range of h values, the bursting trajectory converges to the IP branch if it is available and stable. For example, in the bifurcation diagram included at the bottom of Panel D Figure 4-3, there is an initial interaction of the burst trajectory with the

IP solution. As the value of G_{syn} increases, the interaction between the bursting trajectory and the IP branch loses its significance, and the bursting trajectory converges to the AP spiking solution. As G_{syn} is further increased to large values (bottom portion of Panel F, Figure 4-3), the bursting trajectory further follows the extended stability of the AP periodic branch into the region with lower h. These results suggest that an increase in G_{syn} promotes a transition from in-phase spiking to anti-phase spiking. As G_{syn} is increased, the IP branch loses its stability, and the burst trajectory instead converges to the AP branch.

Transition between ASB and ISB Modifies Burst Period.

In this subsection, we present a potential dynamical mechanism to account for the initial increase and subsequent decrease in burst period that occurs during the transition between ASB and ISB as G_{gap} or G_{syn} is varied.

For any fixed value of G_{syn}, the entire AP periodic solution branch transitions to lower values of h as G_{gap} increases (e.g. highlighted column of Figure 4-4). Even though the increase in G_{gap} with a fixed G_{syn} has no effects on the region of hysteresis between the IP periodic branch and the equilibrium branch, it does increase the region of hysteresis in h between the AP periodic branch and the equilibrium branch. In comparison, the process of varying G_{syn} while fixing G_{gap} has insignificant effects on the location and stability of the AP solution branch (e.g. highlighted row of Figure 4-4).

Comparing the panels in each column of Figure 4-4, it can be easily seen that as long as the AP branch is stable and the IP branch is unstable, the increase in hysteresis with larger G_{gap} will correspond to an increase in burst duration. This increase in burst-duration consequently leads to a longer burst-period. However, as G_{gap} increases, the AP branch loses stability over some ranges of h and the IP branch gains stability. In addition, at a sufficiently large value of G_{gap}, the AP branch becomes entirely unstable and the IP branch becomes stable. This loss in AP stability combined with its left-ward shift in

location decrease the effective range of hysteresis in stable periodic solutions and the equilibrium branch. It eventually offsets the increase in burst period due to left-ward shifting of the AP branch and leads to an overall decrease in burst period. This form of hysteresis is necessary for this class of square-wave bursting (Bertram et al. 1995; Izhikevich 2000; Rinzel 1985).

When varying G_{syn} is paired with a fixed G_{gap}, one does observe loss of stability in the IP solution branch. Nevertheless, such loss of stability does not effectively change the overall hysteresis region (e.g. highlighted row of Figure 4-4) and does not contribute to the change in burst period. In fact, the change in burst period when G_{gap} is kept fixed can be attributed to an extension of the stable AP branch to the left. Therefore, the aforementioned relationship between the variation of coupling strength and the change in hysteresis between the AP branch and the equilibrium branch, which causes period modification, only exists for different G_{gap} values when G_{syn} stays constant. In biophysical terms, increasing G_{gap} increases the dynamic range of the persistent sodium conductance (regulated by h), where the bi-stable existence of anti-phase spiking together with the hyperpolarized silence enable bursting to occur. This increased range of conductance over which spiking occurs leads to longer burst durations. This increase in G_{gap} ultimately results in the anti-phase spiking losing stability, while stabilizing in-phase spiking. It is important to keep in mind that only the stability of the solution branch is affected by the G_{gap} coupling strength; the range of persistent sodium conductance where in-phase spiking and hyperpolarized silence exist (necessary conditions for bursting), however, does not vary with the G_{gap} value.

In summary, we have shown that the stability of the faster dynamics (in-phase or anti-phase) spiking has a profound effect on the slower-time scale dynamics of bursting. These results have been demonstrated in a fifty-neuron network as well as a two-neuron network, and are robust as either G_{syn} or G_{gap} is varied. Mechanisms were determined via

bifurcation analysis of a two-neuron network as G_{gap} is varied, and are consistent with dynamics observed in the fifty-neuron network.

Proposed Metric Defining the Class of Burst Solution

In this section, we propose a metric that categorizes and predicts the convergence of the bursting solution onto either one of the periodic branches as the coupling strengths vary. Panel A of Figure 4-5 illustrates a zoomed-in version of Figure 4-4, showing portions of the bifurcation diagrams relevant to the development of this metric (Figure 4-5, Panel B).

A close examination of Panel A, Figure 4-5 shows that the start of the bursting trajectory always converges to the periodic solution branch that is stable at the "knee" of the z-shaped steady-state solution. Furthermore, when both IP and AP branches are stable, the solution converges to the IP branch. Since only the AP branch is stable at the knee for lower values of coupling strengths, in such cases the bursting trajectories always start at the AP branch. On the other hand, the trajectory converges to the IP branch solution for higher coupling strengths.

These observations are the basis for the formation of the proposed metric, as this metric is defined to be the distance from the end of the stable branch of the IP solution to the knee of the steady-state solution (h_{stable}-h_{LK}). When the IP branch intersects with this knee, h_{stable}-h_{LK} equals zero, at which point one would predict a complete transition to the

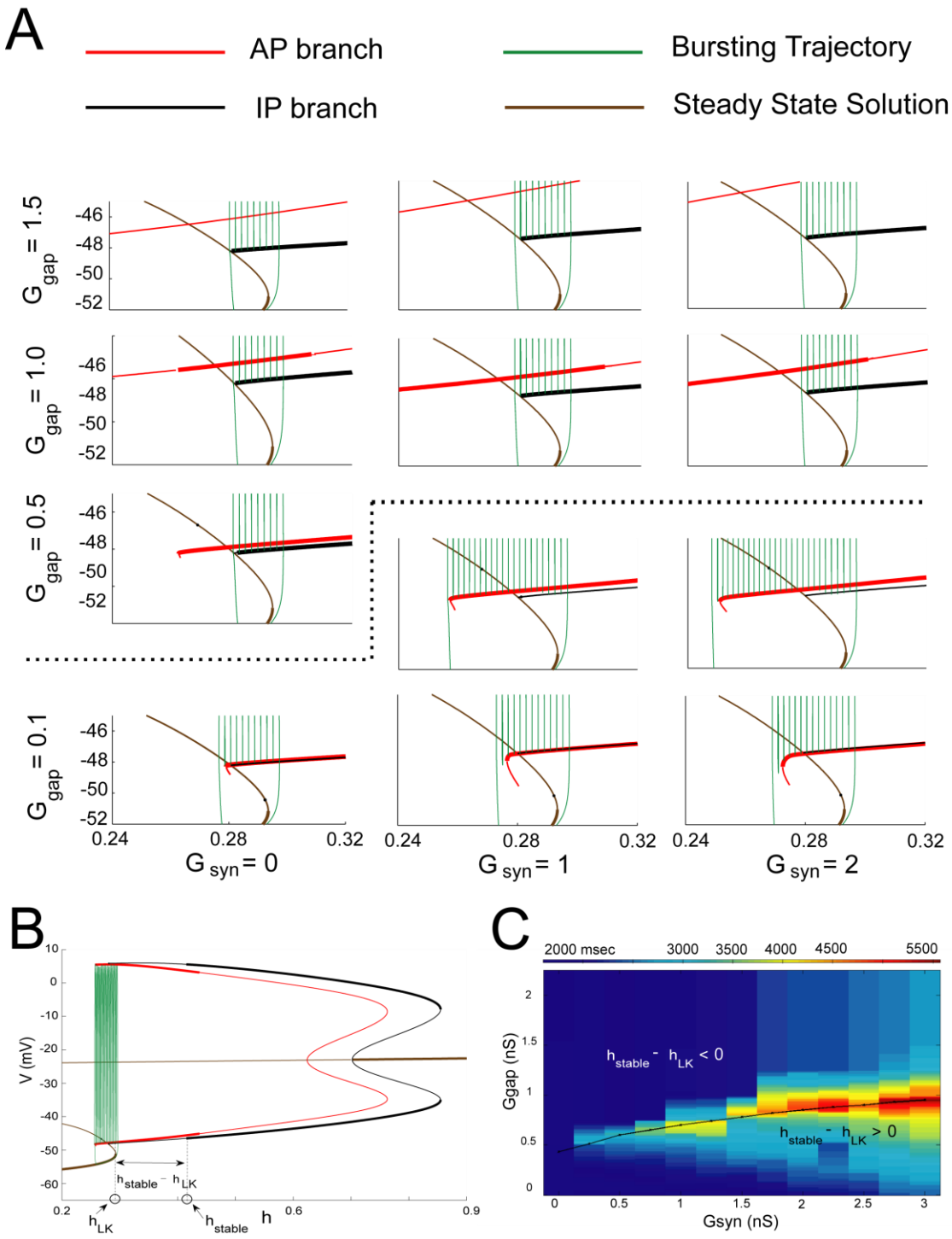

Figure 4.5 Development of a metric categorizing the class of the burst solution. Panel A is a zoomed-in version of Figure 3. For each sub-panel in panel A, the x-axis is h, and the y-axis is membrane voltage V (mV). Panel B illustrates the metric proposed to categorize the convergence of bursting trajectory. Panel C compares the change in burst period (as the coupling strengths are varied)

versus the switch in the sign of the metric (hstable – hLK). Note that Ggap is incremented in 0.1 nS in panel C. The dashed line in Panel A represents the transition of (hstable-hLK) between positive and negative value. The value of (hstable – hLK) is negative for the three sub-panels in the bottom-right corner; and the opposite is true for the five sub-panels on the top-left corner. Accordingly, the bursting trajectory (green) for the three sub-panels in the bottom-right converges to the AP branch (red); and that for the top-left five sub-panels converges to the IP branch (black).

IP bursting mode. Interestingly, the drop in bursting period correlates with a drop of the value h_{stable}-h_{LK} to zero (Figure 4-5, Panel C), both of which occurs when G_{gap} equals to $G_{gap\text{-}p\text{-}critical}$. Therefore, this metric can also be used to identify the critical value of G_{gap} (with fixed G_{syn}) at which the reversal of the trend in the direction of change of burst period, thus spike synchrony, occurs. Approaching from another standpoint, the metric is also valid when characterizing the change in burst period and a critical value of synaptic coupling as varying G_{syn} is coupled with a fixed G_{gap}.

Effects of Gap Junctional Coupling on Spiking and Spectral Properties

Previously published research has studied how gap-junctional coupling modulates inspiratory motoneuron and phrenic nerve activities in the transverse slice as well as the en-bloc preparations (Bou-Flores and Berger 2001). Specifically, a reduction in gap junction strength causes an increase in burst period along with the emergence of a dominant intra-burst spiking frequency as observed in both the hypoglossal nerve rootlet recordings from the transverse slice. Similar effects on bursting period and intra-spike frequency distribution were observed in phrenic nerve recordings. These observations correspond to the results from our study presented in this paper where G_{syn} is fixed and G_{gap} is decreased from a very high level (3 nS) down to the critical value $G_{gap\text{-}critical}$.

Extending and applying identical measures used in analyzing experimental data on our simulation results, we were able to derive conclusions that are consistent with these phenomena observed in experiment settings. As can be seen in Figure 4-6 – along with an increase in burst period – a dominant frequency for intra-burst spiking begins to

emerge when G_{gap} is decreased from 2.25 nS while fixing G_{syn}. Further decrease in G_{gap} below 1.75 nS still allows a dominant intra-burst spiking frequency to exist, accompanied by a decrease in burst period.

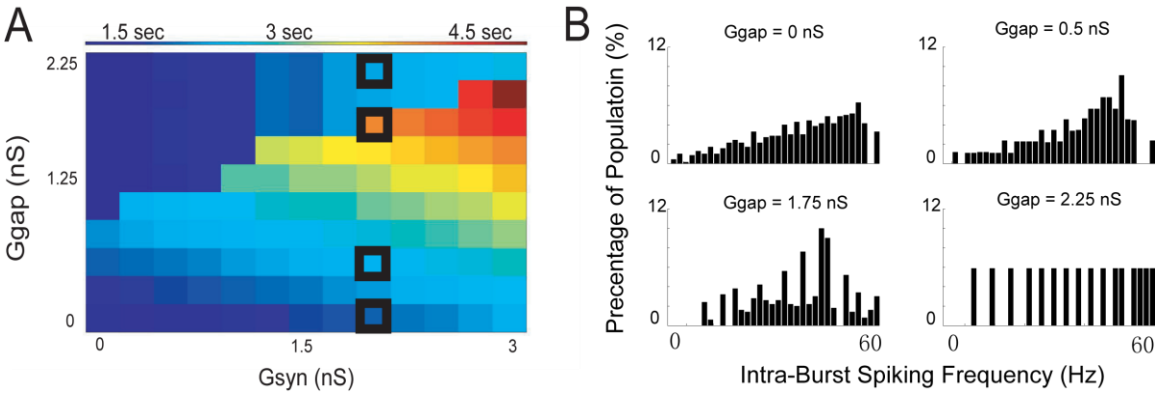

Figure 4.6 Gap-junctional coupling & spectral properties. Panel A is identical to Panel A of Figure 4-2, illustrating how burst period changes with respect to changes in coupling strengths. Panel B demonstrates the appearance of a dominant intra-burst spiking frequency as gap-junctional coupling strength is varied. The x-axis runs from 0 to 60 Hz, showing the range of intra-burst spiking frequency in our simulation data. The y-axis shows the percentage of occurrences of a specific spiking frequency within a single burst. The coupling strengths used to generate Panel B are identical to those identified by the solid black boxes in Panel A.

4.4 Summary

There is little doubt about the importance of the roles played by factors such as electrical or chemical synapses in the functional output of neuronal populations. The slightest differences in the timing, amplitude, or synchrony of the functional neuronal output can be magnified through the circuitry in our nervous system and manifest downstream as physical abnormalities or diseases. Some examples which have already been areas for extensive research are sleep apnea, Sudden Infant Death Syndrome (SIDS), and the Rett syndrome. These disturbances or abnormalities have been linked at the cellular level to several neuromodulatory substances such as norepinephrine and serotonin, which exerts mainly excitatory effects at the millisecond time-scale when

working alone, but produce unexpected emergent network properties at a different time-scale.

Even though previous results presented in Sherman et al. 1991, 1992, and 1994 have presented several aspects of our results in other context, our work here is the first to demonstrate at multiple structural levels how the manipulation of spike synchrony through either electrical or chemical coupling can lead to complex thresholding changes in burst period. Such phenomena cannot be simply explained by a single well-defined biophysical mechanism, but only by considering the interactions between the spiking and bursting processes and the emergent dynamics of the coupled processes. The underlying mechanisms have also been investigated via quasi steady-state bifurcation analysis at the paired-cell level, and can be generalized to explain the complex phenomena observed at the 50-cell network level.

Exploring further in the area of respiratory rhythmogenesis and maintenance, previously published research has studied how inhibitory synaptic transmission and gap-junctional coupling modulate inspiratory motoneuron activities (Bou-Flores and Berger 2001). The "kernel" for these modulatory effects has been proposed to be the pre-Bötzinger Complex (pBC) region, and our results are consistent with these ideas. Moreover, our research is also in line with recent experimental results, where the characteristics of neuronal network activities change in a complex way as the amount of excitation present in the system varies (Doi et al. 2009; Zanella et al. 2009).

5. TWO TYPES OF PACEMAKING PBC NEURONS: DIFFERENCES & SIMILARITIES MANIFESTING AT THE SINGLE-CELL LEVEL AND THE LEVEL OF SIMULATED PBC REGION[3]

5.1 Abstract

The respiratory rhythm originates in the brainstem (Bianchi et al. 1995; Feldman and Smith 1989) in a critical region of the ventrolateral medulla called the PBC (Smith et al. 1991). Evidence from *in vitro* (Funk et al. 1993; Koshiya and Smith 1999; Ramirez and Richter 1996; Smith et al. 1991; Smith et al. 1990) and *in vivo* studies (Koshiya and Guyenet 1996; Ramirez et al. 1998; Schwarzacher et al. 1995; Solomon et al. 1999) suggests that this region contains a locus of rhythm generating inspiratory neurons that continue to fire when isolated *in vitro*, and cause a cessation of normal breathing when lesioned *in vivo*. The traditional view of this respiratory rhythm generation occurring primarily via complex network of inhibitory and excitatory connections (Bianchi et al. 1995; Richter et al. 1992) had become controversial when rhythmogenesis persisted in en-bloc preparation when synaptic inhibition was blocked (Brockhaus and Ballanyi 1998; Feldman and Smith 1989; Onimaru et al. 1990). Recent results (Del Negro et al. 2002a; Thoby-Brisson and Ramirez 2001; Tryba et al. 2003) have also shown that in addition to the NAP-dependent pacemakers – or Cd^{+}-insensitive pacemakers (Del Negro et al. 2002a; Thoby-Brisson and Ramirez 2001) – a second type of pacemaker exists in the pBC of mice (Pena et al. 2004; Thoby-Brisson and Ramirez 2001). This second type of

[3] The concept of the new PBC neuron model has been previously detailed in Specific Aim # 2 in NIH grant R01-HL088886 by the author of this document.

pacemaker is referred to as cadmium-sensitive or CAN-current dependent pacemaker (Pena et al. 2004; Thoby-Brisson and Ramirez 2001).

The work presented here consists of the construction of a new generation PBC model neuron, which incorporates a second-messenger pathway linked to the intracellular [Ca^{2+}] buffering mechanism. As will be presented in the result section, this PBC model neuron is able to simulate both the NAP-dependent and the CAN-current dependent pacemakers. Based on this model, a series of network simulations were conducted to examine the emergent network rhythms as a result of including a varying percentage of different types of pacemakers in the network. A future study focusing on the investigation of how PBC activities might be modulated by neuromodulatory substances released by Raphé neurons is presented in Chapter 7.

5.2 Methods

Overview

All simulations presented in the study were performed in MatLab with SimEngine developed by Simatra Technologies (http://www.simatratechnologies.com). The single-cell level simulations were performed for 60 seconds simulation time, with results from the first 30 second discarded as transient. The network-level simulations were performed for 90 seconds simulation time with the first 30 second discarded as transient.

For our purpose, we first constructed a single-compartment PBC neuron model that serves as a basis for all component neurons within the simulated PBC region. The model's parameter space, made up by the conductance of the persistent sodium current (g_{nap}) and the calcium-dependent cationic current (g_{can}), can be categorized into two "pacemaking modes" where the model neuron is said to be operating as a NAP-burster or a CAN-burster. In other words, the model possess the capability to simulate (Figure 5-1) a spectrum of pacemaking activities characteristic to the I_{nap}-dependent (NAP-burster,

Cd^{+}-insensitive) as well as I_{can}-dependent (CAN-burster, Cd^{+}-sensitive) pacemaking neurons. The distinction between the two pacemaking modes is made based on the differences in simulated membrane electrical activities as a result of depolarizing current injection. Examples of these "pacemaking modes" as well as the typical parameter values used to simulate each can be found in Figure 5-2, and the exact criteria used to make the distinctions are detailed in the result section (Figure 5-3).

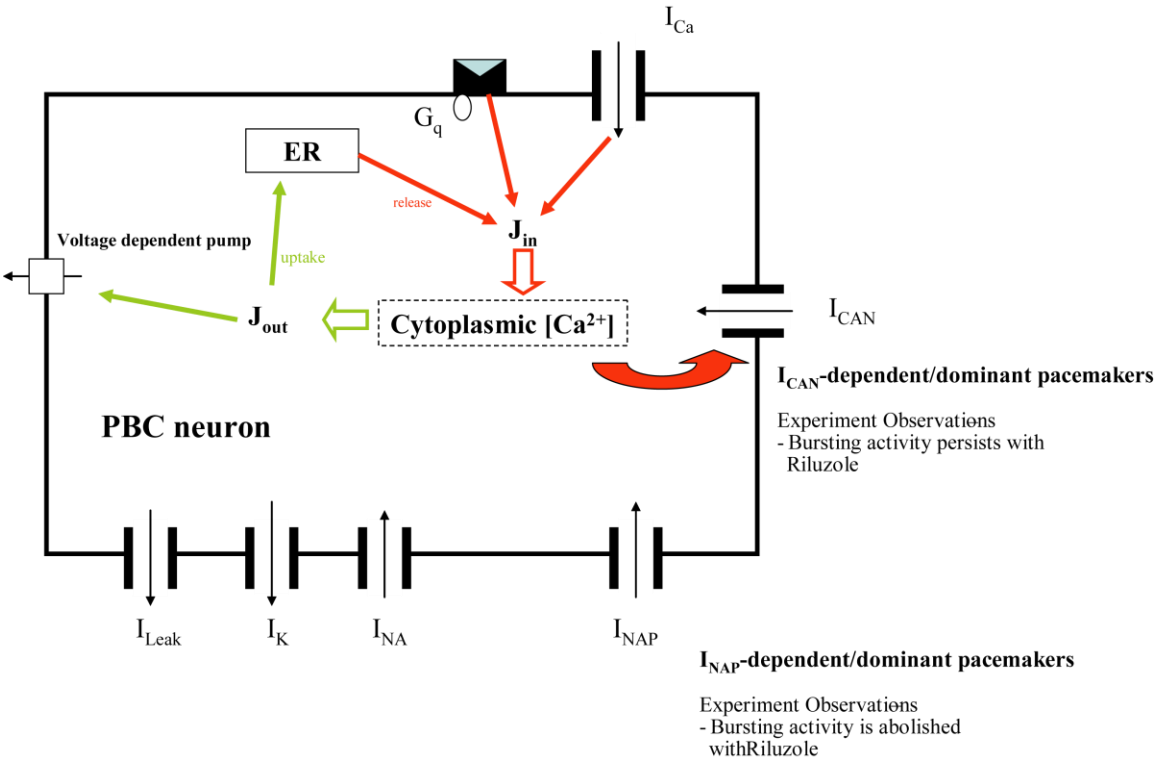

Figure 5.1 Schematics of the single PBC neuron model. The new PBC neuron model includes a new calcium-activated cationic current (Ican), an inward calcium current (It), a G-protein coupled pathway which affects calcium buffering mechanisms mediated by ER as well as a membrane calcium pump. The black arrows associated with the ion channels are indicative of the ion-current flow direction. The red arrows indicate the positive effects of the following three factors on intracellular [Ca2+]: 1.) ER calcium-release, 2.) inward calcium current, and 3.) activation of Gq-coupled receptor. The green arrows indicate the negative effects on intracellular [Ca2+] of: 1.) ER calcium-uptake, and 2.) voltage- & [Ca2+]- dependent membrane calcium pump.

Single PBC model

The schematic of the single-compartment PBC neuron central of this study is illustrated in Figure 5-1. It consists of eight non-linear differential equations. It contains a buffered oscillatory IP3 - endoplasmic reticulum (ER) - Ca^{2+} pathway that is also dependent upon synaptic activation. The model is described by the following equations –

$dV/dt = - (I_{total} - I_{ext}) / C_m$ (C_m: membrane conductance)

Where $I_{total} = I_{nap} + I_{na} + I_k + I_{ca} + I_{can} + I_t + I_{leak} + I_{syn} + I_{tonic} + JEXT_{out}/K$

The equations governing I_{nap}, I_{na}, I_k, I_{syn} (synaptic excitation), and I_{tonic} (tonic excitation) are adopted from previous work (Purvis et al. 2007). Current injection into the model neuron is simulated by the term I_{ext}. $JEXT_{out}/K$ represents the current change due to the outward calcium flux through the calcium pump. The calcium-dependent cationic current I_{can} (CAN-current) can be described by the following equation –

$I_{can} = g_{can} \bullet F([Ca^{2+}]) \bullet (V-E_{cations})$, while $F([Ca^{2+}]) = 1 / (1+(K_{can}/[Ca^{2+}])$

The oscillatory IP_3-ER-Ca^{2+} pathway that includes cytoplasmic buffering effects is formulated as three non-linear differential equations (Keizer and De Young 1992; Wagner and Keizer 1994)–

$d[Ca^{2+}]/dt = \beta([Ca^{2+}]) \bullet (JER_{in} – JER_{out} – JEXT_{out})$

$d[IP_3]/dt = Gq(t, V) + P([Ca^{2+}]) – D([IP_3])$

$dw/dt = (w_{inf} - w) / \tau_w([Ca^{2+}])$, where $\beta([Ca^{2+}])$ represents cytoplasmic calcium buffering effects, $P([Ca^{2+}])$ accounts for effects of intracellular calcium concentration on IP_3 production , and $D([IP_3])$ is the degradation term for IP_3 concentration. The Gq(t, V) term simulates the time and voltage-dependent effects from G-protein coupled receptor, and this term is omitted in the work presented here. The variable w describes the activation of the IP_3 receptor that is dependent upon both calcium and IP_3 binding to the appropriate sites. JER_{in} and JER_{out} stand respectively for the calcium flux flowing into the cytoplasmic space and the calcium uptake by ER. On the other hand, $JEXT_{out}$ stands for the outward calcium flux through a pump located on the membrane, whose

dependency on membrane voltage and intracellular calcium concentration is modeled as follows (Cha et al. 2009) –

$v_{activation} = 1 / (1+\exp(-(V+40)/5))$;

$[Ca^{2+}]$-dependent activation = $0.26 \bullet ([Ca^{2+}]^2) / (0.1+[Ca^{2+}]^2)$

$JEXT_{out} = v_{activation} \bullet Ca^{2+}$-dependent activation

Detailed expressions for the formulations listed above as well as the parameter values relevant to the newly included inward transient calcium current (I_t) current as well as the IP3-ER-Ca^{2+} mechanisms can be found in Appendix A. The parameter values used are all of the correct order of magnitude as observed in previous experiments across various cell types.

Single cell level analysis: parameter space identification – Pacemaking bursters vs. non-pacemakers, NAP-bursters vs. CAN-bursters

All parameter values assigned to the parameters in the PBC model presented here – such as the parameters governing the IP3-calcium pathway or the calcium buffering mechanism, the persistent sodium current conductance, as well as the CAN-current conductance – could potentially significantly alter the electrical profiles of the model. However, in an attempt to focus our efforts to address issues relevant to different pacemaking modes directly stemming from the (co-)existence of persistent sodium current, the CAN current, and the serotonergic modulatory effects – the parameter space examined in this work is limited to be two-dimensional. Namely, the parameter space consists of two conductance variables – the NAP-current conductance (g_{nap}) and the CAN-current conductance (g_{can}) – where both are varied between 0 to 3nS with 0.1nS increment.

Using a divide-and-conquer methodology, we first divide the (g_{can}, g_{nap}) parameter space into the sub-space consisting of non-pacemakers, as well as the subspace where intrinsic bursting activities were observed. The division is made possible by injecting a

model neuron with a specific (g_{can}, g_{nap}) pair at a hyperpolarized state with incremental depolarizing current injection. If the model's membrane electrical activities go through the transition from silence to bursting, and eventually to spiking activities, then the model is categorized as a pacemaker. Otherwise, the model whose activities transition directly from silence to spiking is categorized as a non-pacemaker.

The constrained parameter space for pacemakers was then further divided into 2 regions representing the 2 pacemaking modes – the NAP-bursters, and the CAN-bursters – based on the modulation of the model neuron's bursting activities to depolarizing current injections. The criteria used as well as the calculations performed to define each "pacemaking mode" are detailed in Section 5-3. The prototypical simulated electrical profile of each operating mode is shown in Figure 5-3 & Figure 5-4.

PBC nucleus model

51 PBC model neurons were coupled with all-to-all as well as sparse (10% connectivity) synaptic projections to create a 51-cell network. In the sparse connectivity scheme, each model neuron within the network projects synaptically on average to 5 other randomly selected neurons in the network. These simulations were designed to investigate how different percentage combinations of non-pacemakers with a specific type of pacemakers might affect network-level rhythmogenesis. The number of pacemakers in each network is varied from 0 (e.g. no pacemakers in the network) to 51 (e.g. all network components are pacemakers) with roughly 5-cell increments (Figure 5-7 & Figure 5-8). Some example network compositions are 95% non-pacemakers & 5% NAP-bursters, or 80% non-pacemakers & 20% NAP-bursters, or 70% non-pacemakers & 30% CAN-bursters. The component model neurons in each simulated PBC nucleus are uniformly selected from the population of NAP-busters, CAN-bursters, and non-pacemakers as described in the previous sub-section.

For each composition scenario, 15 trials were performed where the model neurons were connected with all-to-all synaptic projections. For each composition scenario, additional 15 trial simulations were performed where the model neurons are inter-connected with sparse connections (10% connectivity), and are assigned parameter values identical to those used in the 15 trial simulations with all-to-all connections. In all cases, the strength of each synaptic projection (g_{syn}) received by a single model neuron was scaled so that the total excitation from synaptic inputs equals to 7.5nS. On the other hand, the total tonic excitation received by a single model neuron was selected to be 0.2nS.

Simulating the PBC nucleus – Activity analysis

Within the simulated PBC nucleus, rhythmic bursting activities can occur at the single cell level, at the level of a cluster consisting of a small subset of network component neurons, and finally at the network level involving a majority (80%) of model neurons. In view of our objective to examine activities beyond the single-cell level, an automated algorithm was implemented for burst-detection occurring at the cluster level and above. This algorithm takes a histogram of spike times from every cell in the network as input, and determines whether the network activities exhibited can be considered as a network-level burst or not. The maximum and minimum amplitude of the histogram was calculated, and the difference between those values was compared against a threshold (A_{thres}). If the threshold was met at least twice throughout the non-transient simulation time (e.g. at least two bursts in 60 seconds), and if the amplitude of the histogram remained <10% of the maximum amplitude for some pre-defined minimum amount of time ($Interval_{min}$), then the output was defined as a burst. The value for A_{thres} was chosen to be 5, and the value for and $Interval_{min}$ was chosen to be 150 msec respectively. Depending on the degree of population recruitment, the defined burst can be either a cluster-level or a network-level phenomenon. The degree of population

recruitment is defined as the median of the percentage of neuron population that fires at least once within a single episode of (cluster- or network-) rhythmic bursting activity summarized across all bursts from all 15 trials per simulation set-up (e.g. certain pacemaker % composition combined with a specific type of pacemaker, with a certain connectivity scenario). In addition to the degree of population recruitment, another feature of interest is the period of bursting activity defined as the time interval which elapses between two episodes of activities.

5.3 Results

Investigating the parameter space: Pacemaker identification

Starting from a state of zero electrical activities, pacemaker neurons are those neurons that respond to depolarizing current injection with the emergence of bursting activities. Furthermore, once these pacemaker neurons are already exhibiting bursting activities, they continue to respond to additional depolarizing current injections with bursting activities until spiking activities emerge and persist with further depolarization. Non-pacemakers, on the other hand, are defined as neurons that respond to depolarizing current by a direct transition from non-activity to spiking.

Setting g_{leak} at 3.3 nS and E_{leak} at -70mV, for each pair of (g_{nap}, g_{can}), a depolarizing current is injected into each model neuron. With g_{nap} and g_{can} being systematically varied from 0 to 3nS with 0.1nS increment, a total of 34596 (31 ● 31 ● 36) single-cell simulations were performed where the magnitude of the depolarizing current was increased from 0 to 70pA with 2pA increment for each pair of (g_{nap}, g_{can}). Based on the response of a model neuron to depolarizing current injections, the parameter space is divided into two parts; namely, the pacemaking region and the non-pacemaking region (Figure 5-2).

Panel G in Figure 5-2 illustrates the results from this process of identifying pacemakers in the (g_{nap}, g_{can}) parameter space. The red squares indicate a (g_{nap}, g_{can}) pair that facilitates the emergence of bursting activities in response to certain magnitudes of depolarizing current injection, where the "threshold" current magnitude where the transition from silence to bursting occurs differs for each (g_{nap}, g_{can}) pair. The blue squares, in comparison, represent the (g_{nap}, g_{can}) pairs where the electrical profiles of the non-pacemaker model neurons transition directly into spiking as the magnitude of depolarizing current is increased.

Panel A through C illustrate the electrical profiles of model neurons with values of (g_{nap}, g_{can}) corresponding the emphasized parameter-pair in Panel D, Figure 5-2. The bursting activities shown are those that first emerge with depolarizing current injection. The (g_{nap}, g_{can}) values specific to each panel are detailed in the figure caption. As can be already seen from this figure, characteristically different bursting activities exist within the parameter space. In the following sub-section, the differences in bursting characteristics – such as burst shape and burst duration – as well as the model neuron's response to depolarization are closely related to the different mechanisms underlying the rhythmic bursting activities.

Mechanisms underlying bursting activities in different regions of the pacemaking parameter space

As alluded to earlier, previous experiment results have demonstrated the existence of two different types of pacemakers within the PBC region. The type of pacemakers that responds to depolarization with prominent period modulation was identified to be Cd^{+}-insensitive, as its bursting activities persist with the blockade of calcium-dependent cationic current (I_{can}) with Cd^{+}. These pacemakers have also been shown to be sensitive to the blockade of persistent-sodium current (I_{nap}) with Riluzole and are alternatively referred to as I_{nap}-dependent pacemakers, e.g. NAP-burster. On the other hand, those

pacemakers whose bursting activities are sensitive to Cd^+ application have been shown to be resistant toward Riluzole. These Cd^+-sensitive pacemakers are referred to as CAN-bursters in this work. Unlike NAP-bursters, the electrical profiles of CAN-bursters show very little period modification when injected with depolarizing current. In fact, CAN-bursters exhibit more prominent burst-duration modulation when depolarized.

In addition to the classifications based on responses to depolarizing current, Cd^+, or Riluzole, these two types of pacemakers have been shown to respond to serotonin application differently. The increase in burst-duration observed in CAN-bursters is more prominent than period modulation in response to serotonin application. Contrary to the case with CAN-bursters, decreased burst-duration and period are observed in NAP-bursters with serotonin application. Further analysis of the PBC model which simulates

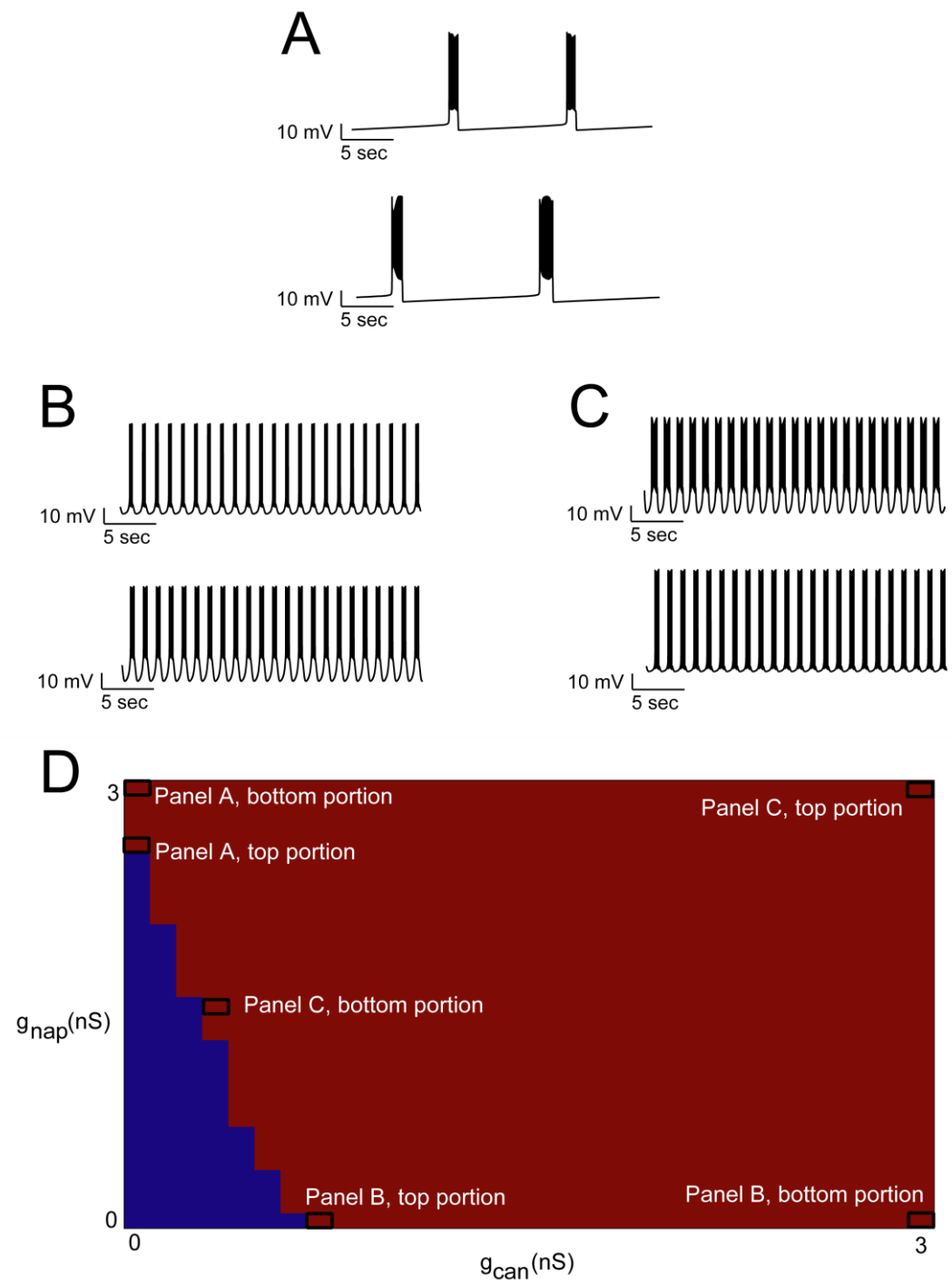

Figure 5.2 Investigating the parameter space: Pacemaker Identification. Panel A through C illustrate the bursting activity of model neuron from different corners of the parameter space as the pacemaking property first emerges with depolarizing current injection. Panel D shows the result from pacemaking-identification within the parameter space where (gnap, gcan) = (0~3nS, 0~3nS). The red portion represents the sub parameter space of pacemakers, and the blue portion represents that of non-pacemakers.

both types of pacemakers as detailed below highlights the underlying mechanisms for the pacemakers' distinctive responses to depolarizing current or serotonergic modulation.

Along the two axes of our parameter space, the pacemaking properties of the model neurons depend entirely on I_{nap} (when $g_{can} = 0$) or I_{can} (when $g_{nap} = 0$). With this sole dependency on either g_{nap} or g_{can} for their pacemaking property, the model neurons along the axes proto-typically demonstrate the period (left portion of Panel A & B, Figure 5-3) or burst-duration modulation (Panel C & D, Figure 5-4) characteristics of the two types of pacemakers (e.g. CAN-bursters and NAP-bursters) in response to depolarizing current injection. Results from bifurcation analysis on two model neurons prototypical of the CAN-burster and the NAP burster are illustrated in Figure 5-3 and Figure 5-4 & Figure 5-5 respectively.

Figure 5-3 demonstrate the analysis results for the NAP-burster (g_{nap}=3, g_{can}=0nS). As illustrated in the left portion of Panel A & B, depolarizing current injection leads to faster bursting activity (reduced period) as well as a relatively less significant decrease in burst duration. This phenomenon can be explained by examining the change in bifurcation landscape as shown in the right portion of Panel A & B, Figure 5-3. The slow bifurcation parameter here is *h*, which governs the inactivation of I_{nap} in the model neuron. With all else being equal, a depolarizing current injection shifts the lower branch of the steady state solution (black) to the left. Consequently, the region of hysteresis between the steady state solution and the period solution (red) decreases, leading to significant reduction burst period and less significant decrease in burst duration.

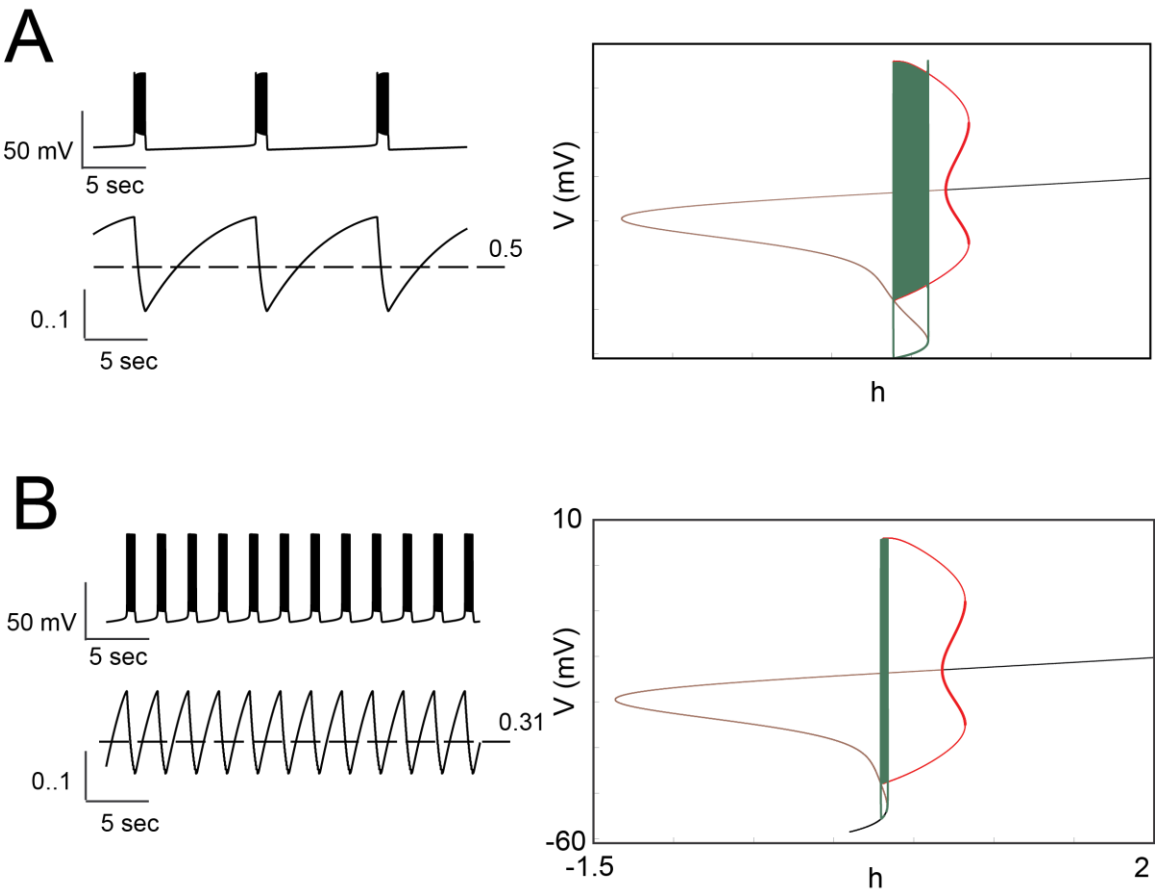

Figure 5.3 The electrical profile and bifurcation landscape for a NAP-burster in response to depolarizing current injection. The top-left portion of panel A shows the electrical profile of a model neuron (membrane voltage V, mV) with (gnap, gcan) = (3, 0) nS, and the bottom-left portion shows the variation in the activation of I_{nap} current (h, no unit). The right portion of panel A shows the corresponding bifurcation landscape (red: periodic solution, brown: unstable steady state solution, black: stable steady state solution), with corresponding bursting trajectory imposed in green. Panel B shows the same information from same model neuron, with the addition of a depolarizing current injection of 10pA. The mechanism for prominent period modulation observed is illustrated in the right portion of Panel A & B.

Non-linear bifurcation analysis was also performed for the prototypical CAN-burster (g_{nap}=0, g_{can}=3nS). In Figure 5-4, the top trace of Panel A shows the membrane voltage of the pacemaking CAN-burster with no current injection. The intracellular calcium concentration – which is directly linked to the inward calcium-dependent cationic current experimentally verified to be responsible for the pacemaking property of

a CAN-burster – is contributed by two sources in the modeling work presented here. The first source is the fast inward calcium current, and the second one is the intracellular calcium release from the endoplasmic reticulum (ER) controlled by $[IP_3]$. The relationship between the membrane potential and the variations in the two concentrations ($[Ca^{2+}]$ & $[IP_3]$) of a CAN-burster is shown as the green trace in Panel B, Figure 5-4. The projection of this relationship (green) on to the x-y plane indicates a constant relationship between $[Ca^{2+}]$ and $[IP_3]$ (black) through the progression of the bursting activity.

Since the conventional role of I_{nap} is completely abolished in a prototypical CAN-burster, the variation in $[Ca^{2+}]$ (direct contribution) and $[IP_3]$ (linked to $[Ca^{2+}]$, indirect contribution) can be considered as the slow mechanisms responsible for inducing bursting activities. Furthermore, non-linear bifurcation analysis was conducted taking the main slow mechanism, $[Ca^{2+}]$ oscillation, as the bifurcation parameter. Changes in the pacemaking properties of the CAN-burster as a result of serotonin application or depolarizing current injection can be explained by examining the bifurcation landscape of the prototypical CAN-burster.

For different values of $[IP_3]$ within the baseline oscillatory range (middle trace of Panel A, Figure 5-4), the bifurcation landscape remains constant, and simulation results showed no modulations in burst duration or burst period (results not shown). When $[IP_3]$ is elevated above its baseline level, simulating the effects of serotonin application, the bifurcation landscape still remains identical (Panel C1-C2 and D1-D2 of Figure 5-4, where $[IP_3]$ was fixed at 0.8 μM and 1.2 μM respectively). However, a decrease in burst period and a significant increase in burst duration was observed since a drastically elevated $[IP_3]$ upsets the original calcium uptake-release ER mechanisms. As a result, the amplitude of $[Ca^{2+}]$ oscillation increases, allowing longer burst duration and a slightly shorter burst period to manifest (Panel C2 & D2 of Figure 5-4). Similar phenomena were observed in previous experiments investigating how the electrical activities of CAN-bursters can be modulated by the application of norepinephrine (NE), which triggers

overlapping if not identical down-stream second-messenger pathways as 5HT (Doi and Ramirez 2008; Doi et al. 2009; Feldman et al. 2005; Neverova et al. 2007; Viemari and Ramirez 2006).

Further dissection of the bifurcation landscape specific to a CAN-burster leads to the conclusion that burst initiation and termination are caused by a saddle-node on invariant circle (SNIC) bifurcation structure completely different from that in the case of NAP-burster. Due to this specific SNIC bifurcation structure, the shift in the steady-state solution to the left (Panel B & D, Figure 5-5) as caused by depolarizing current allows bursting activity to be initiated (green) at a lower level of $[Ca^{2+}]$ (Panel D, Figure 5-5). This in turn leads to a prominent positive modulation in burst-duration that is characteristic of the CAN-burster receiving a depolarizing current injection (Panel A, Figure 5-5). The relationship between the amplitude of depolarizing current and the minimum $[Ca^{2+}]$ for burst initiation is illustrated in Panel C, Figure 5-5.

Previous experiment work has demonstrated in respiratory related neurons (e.g. PBC neuron, hypoglossal motoneuron) under serotonergic modulation a suppression of leak current and a positive influence on intracellular $[Ca^{2+}]$ speculated to be mediated by the IP3-pathway. As illustrated in Figure 5-4 through Figure 5-6, the simulated NAP-burster responds to depolarizing current with decreased burst duration and decreased burst period. However, these effects are completely absent with any manipulations on the IP3-pathway as g_{can} is set to zero. On the other hand, the burst period of the simulated CAN-burster can only be modulated by an elevated $[IP_3]$; whereas its burst duration can be increased by both depolarizing current and an increased $[IP_3]$. Since our model accurately simulates the variety of responses elicited from the two types of PBC pacemakers, the different mechanisms underlying pacemaking properties in the CAN- & the NAP-burster, as well as changes in their respective bifurcation landscape in response to depolarizing current injection and/or elevated $[IP_3]$ presented here provide an excellent

substrate for further investigation of the serotonergic effects in the transverse slice respiratory circuitry. This important point is further expounded upon in Chapter 7.

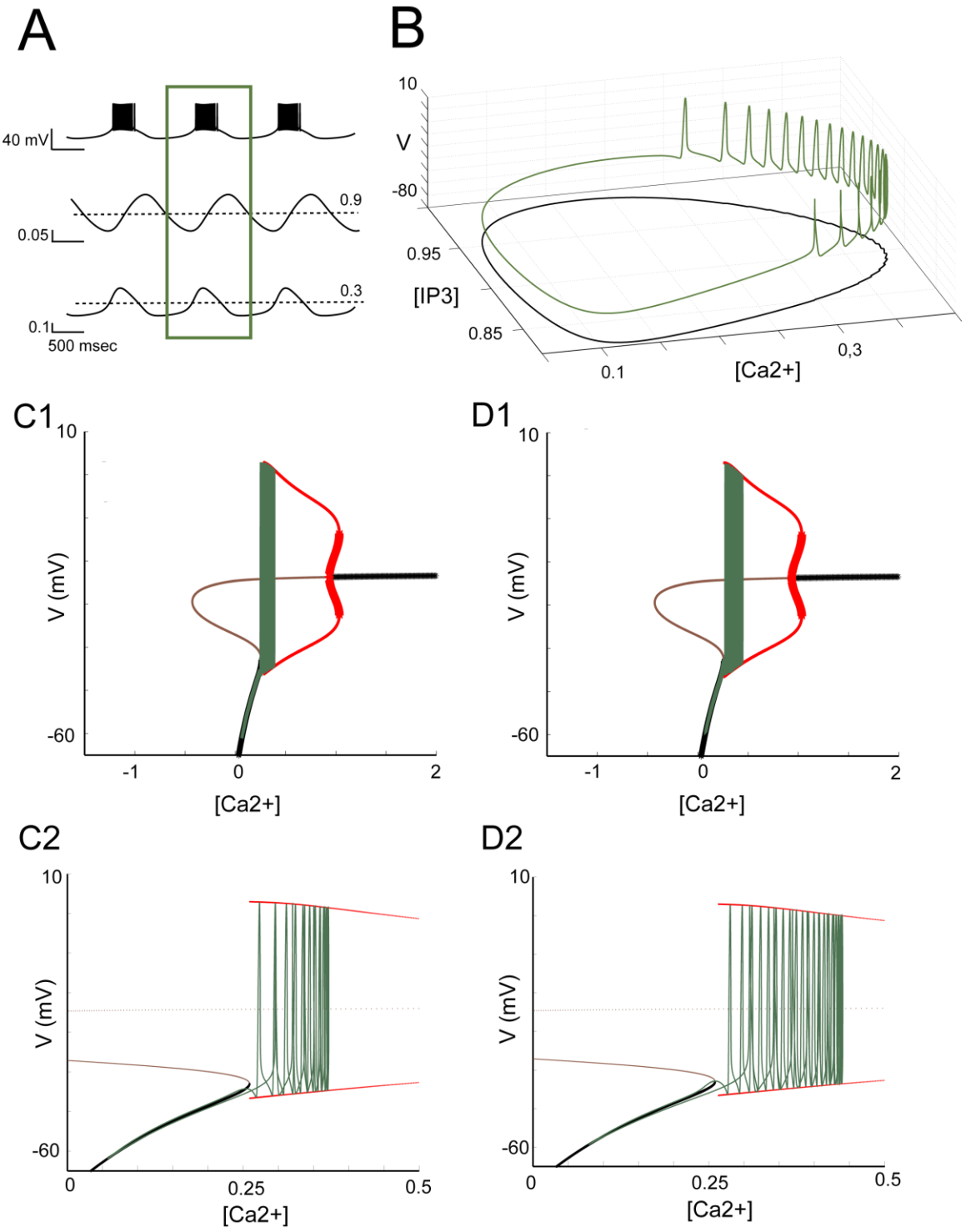

Figure 5.4 The electrical profile and the typical bifurcation landscape for a CAN-burster: simulated serotonergic modulation. From top to bottom, the three traces shown in panel A are the membrane potential (mV), the [IP3], and [Ca2+] traces (both in μM) of a prototypical CAN-burster with (gnap, gcan) = (3, 0). Panel B contains a portion of these three trances (highlighted by a green box in Panel A) plotted in a different parameter space showing the variations in the two slow processes - [IP3] and [Ca2+] – in connection to a single burst of the CAN-burster. Panel C1 shows the bifurcation landscape when [IP3] is fixed at 0.8 μM (green: bursting trajectory, red: periodic solution, brown: unstable steady state solution, black: stable steady state solution). Panel D1 shows the bifurcation landscape when [IP3] is fixed at 1.2 μM. Panel C2 & D2 zoom into the regions of interest in Panel C1 & D1.

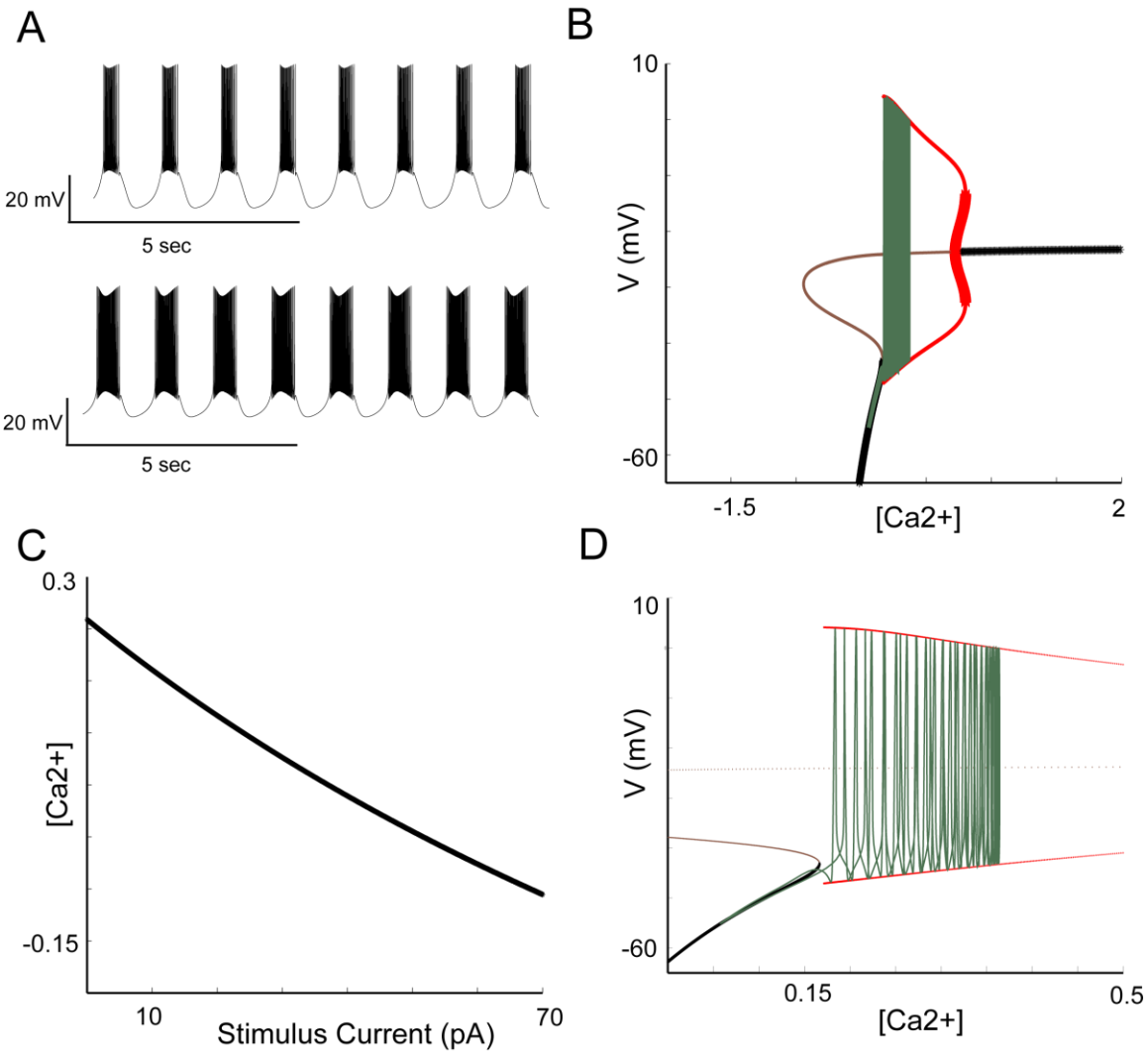

Figure 5.5 Changes in the bifurcation landscape for a CAN-burster: depolarizing current injection. (For Panel B & D, bursting trajectory is imposed in green. The color red indicates

period solution, and the color brown (unstable)/black (stable) indicates steady state solution) Panel A illustrates the significant burst duration modulation as a result of depolarizing current injection (bottom portion). From top to bottom, the stimulus current is 0pA and 20pA respectively. In comparison to Panel C1 & C2 of Figure 5-4, where stimulus current is 0pA, Panel B & D here illustrate the bifurcation landscape when the stimulus current is 20pA. It is important that the lowest $[Ca^{2+}]$ supporting burst initiation roughly equals to 0.25μM in Panel C1 & C2 in Figure 5-4; however, this value is left-shifted to roughly 0.15μM in Panel B & D here. Panel C shows results from two-parameter bifurcation analysis, showing how an increase in the amplitude of depolarizing stimulus current (x-axis) allows for burst initiation at a lower level of $[Ca^{2+}]$ (μM).

Pacemaking mode identification: NAP-bursters vs. CAN-bursters

Summarizing the results presented so far, in the parameter space of interest (e.g. (g_{can}, g_{nap}) = (0~3 nS, 0~3 nS)), the different underlying mechanisms for pacemaking activities in a prototypical NAP-burster (g_{can}=0) as well as a prototypical CAN-burster (g_{nap}=0) have been investigated using non-linear bifurcation analysis. The period and burst duration modulation observed in experiments as well as our simulation studies can be explained by the difference in the bifurcation landscape, along with changes in the landscape induced by depolarizing current injection. These results from analyzing the prototypical NAP-burster and CAN burster can be applied to understanding the entire parameter space in the sense that the combined effects of g_{nap} & g_{can} determine the degree & type of modulation one observes when the model neuron is depolarized. In this subsection, we further categorize the (g_{nap}, g_{can}) parameter space into different pacemaking modes, where depolarizing current injection causes characteristically different modulations of the bursting activity of a single model neuron.

Figure 5-6 illustrates the results from this process. Starting from a hyperpolarized state, a model neuron was systematically injected with a depolarizing current ranging from 0 to 70 pA (with 2 pA increment). The period as well as burst duration for each level of current injection is calculated. As the model neuron becomes more depolarized, the period modulation is calculated as ($period_{depolarized}$ - $period_{hyperpolarized}$) /

$period_{hyperpolarized}$, and the burst duration (BD) modulation is calculated as ($BD_{depolarized}$ − $BD_{hyperpolarized}$) / $BD_{hyperpolarized}$. During this process of incremental depolarizing current injection, if the maximum observed period modulation between two increments in injected current is more negative than -30%, the pacemaker is then categorized as a NAP-burster (Panel A, Figure 5-6). This categorization of NAP-bursters corresponds to a median burst-duration modulation being more negative than -15% (Panel B, Figure 5-6). On the contrary, a pacemaker is categorized as a CAN-burster if its burst duration modulation is positive. In some cases, the level of burst duration modulation reaching is greater than 30% (Panel B, Figure 5-6). This categorization of CAN-bursters corresponds by a maximum period modulation of ~0% (Panel A, Figure 5-6).

In summary, the parameter space that renders the PBC neuron with pacemaking properties characteristic of NAP-bursters is highlighted in orange in Panel C, Figure 5-5. On the other hand, the red region indicates the region where pacemaking properties characteristic of CAN-bursters are observed. The parameter space for NAP-bursters does not overlap with the region for CAN-bursters. Interestingly, when a subset of the identified NAP-bursters is projected onto the x-axis (g_{nap} forced to 0), these neurons do not lose their pacemaking property but instead behave as CAN-bursters. On the other hand, when the parameter space for CAN-bursters is projected onto the y-axis (g_{can} forced to 0), all CAN-bursters lose their pacemaking properties. These observations are significant in the sense that they suggest the I_{nap}-dependent and I_{can}-dependent pacemaking properties are not mutually exclusive, e.g. both currents contribute to a neuron's bursting activities.

Significance of pacemakers in a neural network: beyond single-cell level bursting activities & population recruitment

Network-level simulations consisting of rhythmically active cells are not unique to the area of respiratory rhythmogenesis. Examples of network level simulations can be

found in the area of cardiac physiology, where the significance of various attributes of the sinoatrial node (e.g. the SN node), the natural pacemaker of the heart, has been studied (Chang et al. 2009; Protas et al. 2010). In addition, previous experiments as well as computational research focusing on investigating physiological functions controlled by neural network outputs have demonstrated numerous instances where network-level rhythmic activities can emerge in the absence of bursting activities at the isolated single-cell level (Kosmidis et al. 2004; Rubin 2008). Network-level rhythmic bursting phenomenon in the absence of pacemakers, along with the observed low population percentage of pacemakers ranging from 5% to 10% in naturally occurring neural networks, have long been used as two of the most common arguments against the significance of pacemakers in neural signaling. However, our simulation results – as will be presented in this section (Panel A & B from Figure 5-7 & Figure 5-8) – propose that the presence of pacemakers, albeit at low percentage (5.8%), demonstrate higher capability at inducing cluster level rhythmic behavior with greater level of population recruitment within each burst.

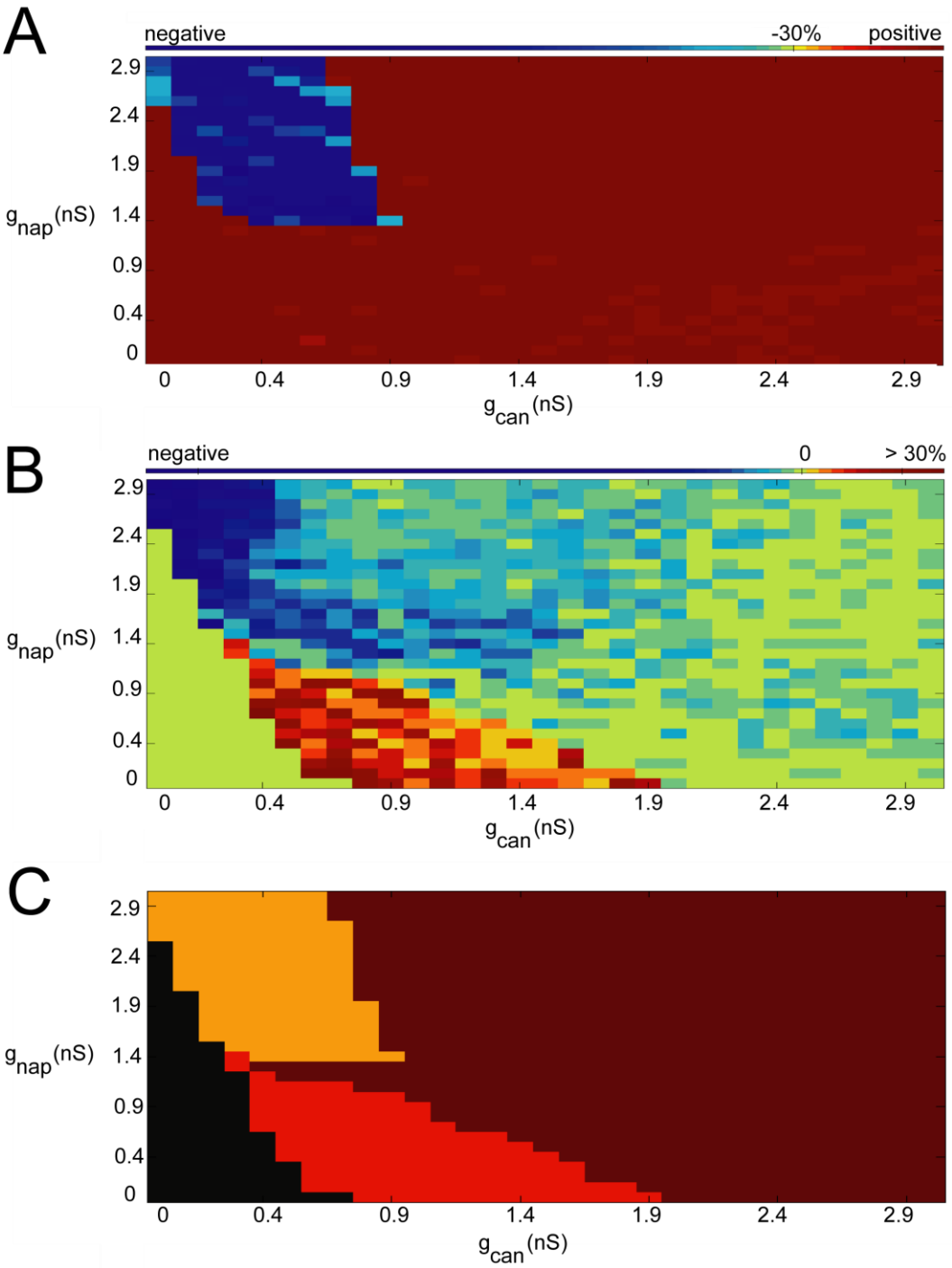

Figure 5.6 Different pacemaking modes within the parameter space: NAP-burster & CAN-burster. Within the parameter space of (gnap, gcan) = (0~3, 0~3nS), Panel A shows the degree of period modulation from depolarizing current injection. Panel B shows the degree of median burst duration modulation in response to depolarizing current injection. Panel C shows the overall results of pacemaking mode identification in the parameter space. The lower-left corner (black) in Panel C represents non-pacemakers. The upper-right corner (brown) in the same panel represents pacemaking model neurons that

show minimal period modulation & negative burst duration modulation (not characteristic of CAN-bursters) in response to depolarizing current injection, therefore, this region is characterized neither as the CAN-bursters nor as the NAP-bursters. The parameter space characterized as NAP-bursters is indicated in orange, whereas the parameter space characterized as CAN-bursters is indicated in red.

Two important conclusions can be derived by examining the top two panels in Figure 5-7 & Figure 5-8. First of all, in comparison with simulation results based on model networks consisting only of non-pacemakers, a pacemaker percentage as low as 5.8% is able to induce cluster level bursting behavior with certainty (probability = 1). Secondly, especially in networks containing NAP-bursters, the inclusion of pacemakers, even at a low percentage, recruit more neurons within the network to fire at least once within a single burst. When the pacemaker percentage is raised to 9.8%, the probably of emerging bursting activities still equals to 1; furthermore, population recruitment reaches as high as 45% within each single burst. Therefore, even though a network containing only non-pacemakers can at times induce bursts involving groups of neurons in the network, the presence of pacemakers within a neural network can further contribute positively to overall network-level rhythmogenesis.

Emergence of network-level rhythmic activity: NAP-bursters networks vs. CAN-bursters networks

After identifying the (g_{nap}, g_{can}) pairs which render the model neurons with electrical profiles characteristic of either the Cd^{+}-insensitive (NAP-burster) or Cd^{+}-sensitive (CAN-burster) pacemakers, the network-level studies simulating the PBC

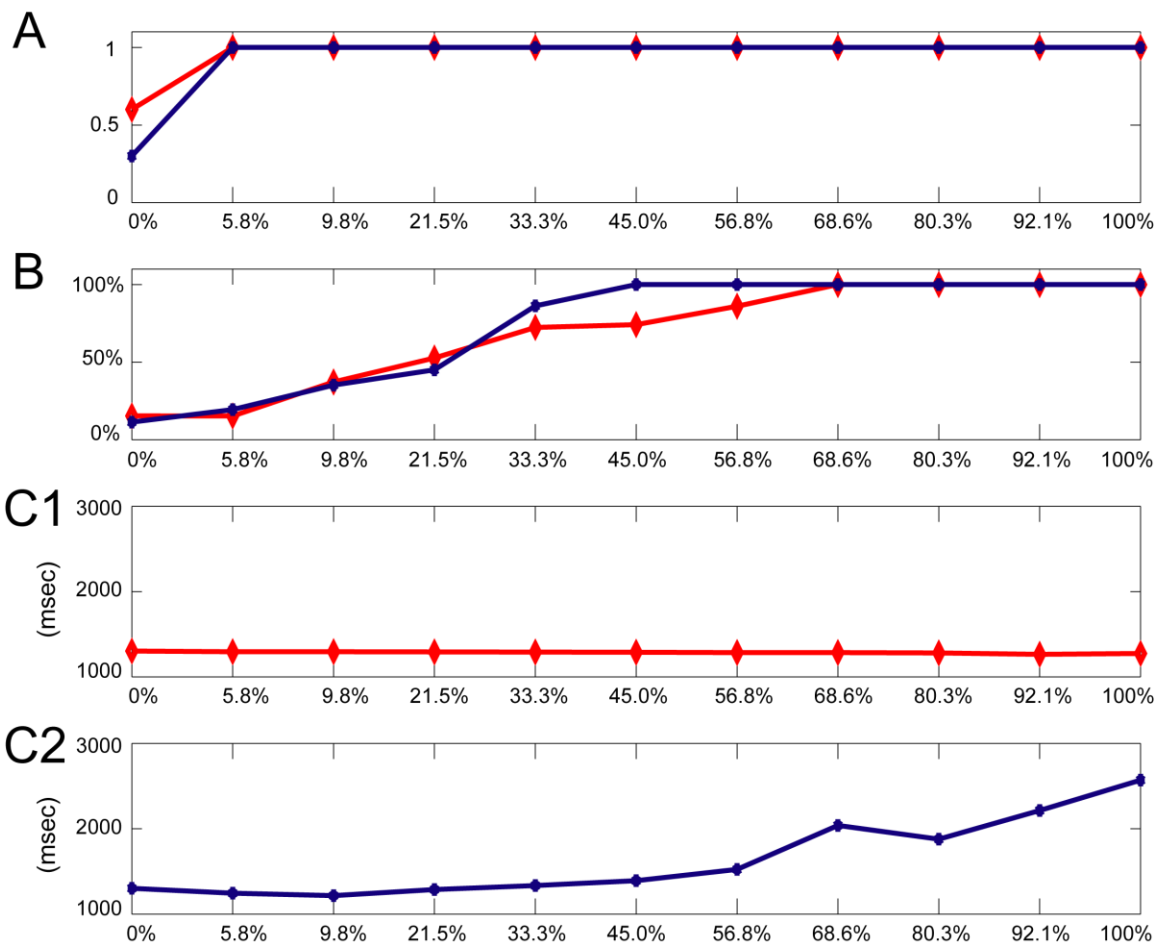

Figure 5.7 Simulating the PBC region, all-to-all connectivity: effects of different percentages of CAN- or NAP-bursters. In this set of simulations, the model neurons are interconnected with all-to-all synaptic projections. The x-axis shows the varying percentages of pacemaking CAN- (indicated in red with hollowed diamond markers) or NAP-bursters (indicated in blue with asterisk markers) included in the simulated network. Panel A shows the probability of either cluster-level (population recruitment < 80%) or network-level (population recruitment >= 80%) bursting activities in the network. Defining the population recruitment as the median number of neurons that fire at least once in all burst identified, Panel B shows the degree of population recruitment for each type & percentage of pacemakers included in the network. Panel C1 & C2 shows the variation of burst period versus the percentage of CAN-pacemakers & NAP-pacemakers included in the network respectively.

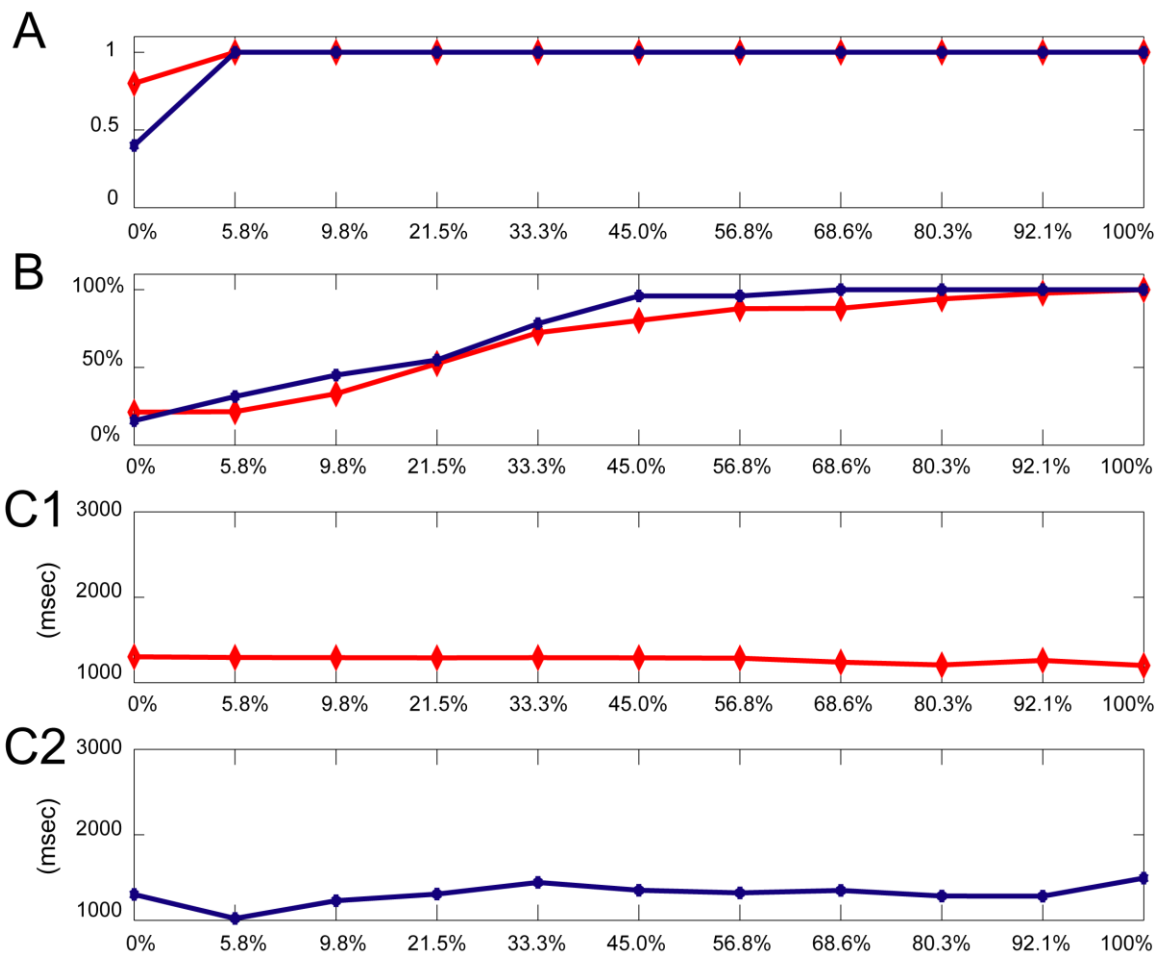

Figure 5.8 Simulating the PBC region, sparse connectivity: effects of different percentages of CAN- or NAP-bursters. In this set of simulations, the model neurons are interconnected with sparse (10%) synaptic projections, e.g. on average, each model neuron receives synaptic inputs from 5 neurons and project to 5 neurons in the network. The x-axis shows the varying percentages of pacemaking CAN- (indicated in red with hollowed diamond markers) or NAP-bursters (indicated in blue with asterisk markers) included in the simulated network. Panel A shows the probability of either cluster-level or network-level bursting activities in the network. Panel B shows the degree of population recruitment for each type & percentage of pacemakers included in the network. Panel C1 & C2 shows the variation of burst period versus the percentage of CAN-pacemakers & NAP-pacemakers included in the network respectively.

region were accomplished by constructing a series of 51-cell networks where varying percentages of pacemakers – either NAP-bursters or CAN-burster – are connected with

non-pacemakers with all-to-all or sparse synaptic connections. The results from these simulations were summarized in Figure 5-7 and Figure 5-8.

As introduced in the previous section, Panel A from both Figure 5-7 and Figure 5-8 present the probability of network-level rhythmic burst activity versus the percentage of pacemakers included in the network. Panel B from both figures illustrate the population recruitment level observed within a single burst. Panels C1 & C2 in Figure 5-7 summarize the range of burst period observed versus the percentage of pacemakers observed in networks with all-to-all synaptic connections consisting of either NAP-bursters & non-pacemakers, or CAN-bursters & non-pacemakers. Similar information from networks with sparse (10%) synaptic connections was shown in Panels C1 & C2 in Figure 5-8.

Immediately, a conclusion can be drawn from Panel A & B from Figure 5-7. The probability of bursting activities involving multiple neurons emergence reaches 1 as soon as the pacemaker percentage reaches 5.8%. Furthermore, population recruitment level increases with higher pacemaker percentages. The qualification of network-level bursting activity (80% population recruitment) defined in the Methods section is satisfied when the pacemaker percentage reaches roughly 33%. As the pacemaker percentage continues to increase, the population recruitment level increases, and reaches complete recruitment when the pacemakers included in the network reaches 45% and 68% for NAP-bursters networks and CAN-bursters network respectively. This observation implies that NAP-bursters have higher capability at recruiting network neurons.

Another feature of the cluster- or network-level bursting activities, e.g. the range of bursting period that can be possibly generated by the network, also exhibits interesting variability in relation to the type of pacemakers included in the network (Panel C1 & C2, Figure 5-7). As shown in Panel C1 of Figure 5-7, the median period observed in CAN-bursters networks remain approximately the same when different percentages of pacemakers are included in the network; where as in the NAP-bursters networks, a wider

range of median burst period was observed. Defining the "output robustness" as the variety of network burst activities observed, these two observations in network burst period in NAP-bursters networks and CAN-bursters networks indicate that the NAP-bursters networks possess a higher level of output robustness. Another set of simulations (results not shown) were also conducted, where the effects of varying levels of tonic and synaptic excitations were investigated. In these simulations, the general relationship between pacemaker percentage and the behavior of the network remains the same, with higher level of synaptic excitations supporting more network-level bursting activities and higher population recruitment for each percentage of pacemakers included in the network

In Figure 5-8, where simulation results from networks with sparse synaptic connections were presented, one can see that conclusions qualitatively identical to the results from networks with all-to-all connections can be derived. As the percentage of pacemakers included in the network increases, bursting activities beyond the single-cell level emerge with certainty, and the population recruitment level within a single burst increases. In addition, the range of burst period observed in NAP-bursters network is still wider than that observed in CAN-bursters network, indicating higher output robustness in the NAP-bursters networks. The conclusions relevant to all-to-all NAP-bursters network qualitatively reproduce those derived from previous modeling research based on a different PBC model presented by Purvis et al. 2007.

5.4 Summary

A new PBC model built upon our previously developed PBC neuron model described in Purvis et al. 2007 is introduced in this chapter. This new model is able to simulate two types of pacemaking activities (e.g. CAN-bursters & NAP-bursters) experimentally identified in multiple publications (Pena et al. 2004; Thoby-Brisson and Ramirez 2001). Different bifurcation structures underlying the two pacemaking modes are also identified in this chapter. Network-level simulations investigating how different

percentages of different types of pacemakers within a simulated PBC region, in addition to different interneuron connectivity, can influence overall network-level phenomena. The results support the significance of pacemakers, albeit at low percentages, in naturally occurring neural networks. In fact, the inclusion of pacemakers results in an immediate increase in the probability of multi-neuron bursting activities to 1 as well as a higher degree of population recruitment. Lastly, except for a reduced output robustness observed in the NAP-bursters networks, networks with sparse connectivity produce qualitatively identical results with networks with all-to-all connectivity.

The completion of this project where different types of pacemaking modes are examined at both the single-cell level and the network level establishes a simulation platform for investigating how modulatory agents commonly present in the transverse slice (e.g. serotonin, SP) can affect neuronal activities at multiple structural levels. This proposition is described in more details in Chapter 7.

6. HYPOGLOSSAL MOTONEURON: NEUROMODULATORY EFFECTS VIA THE ACTIVATION OF SECOND-MESSENGER PATHWAYS[4]

6.1 Abstract

Respiratory motoneurons such as Hypoglossal Motoneurons (HM) are not directly involved in respiratory rhythmogenesis; however, their discharge pattern is an important determinant for alveolar ventilation through convolving with respiratory mechanics. Changes in respiratory motoneuron excitability are functionally important as failure to regulate this aspect can lead to pathological conditions (Feldman et al. 2005). Specifically, the excitability of HM is subject to modulation by numerous factors including serotonin (5HT), TRH, norepinephrine (NE), substance P (SP), pH level, as well as multiple protein kinases and phosphatases.

Relevant to the scope of the research presented in this document, respiratory motoneurons receive tonic serotonergic modulations directly from medullary Raphé neurons, and excitatory innervations through the pre-motoneurons (Section 2-1). The serotonergic modulation mediated by a myriad of intracellular signaling pathways is of special interest, since preliminary experiments in this area have shown that such mechanism plays an important role in the long-term plasticity of HM (Neverova et al. 2007; Tadjalli and Peever). In this chapter, we present results from a preliminary study focusing on constructing a new-generation HM model incorporating a part of the complex second messenger pathways downstream of serotonergic modulation known to be significant in the regulation of intracellular calcium dynamics. The model facilitates

[4] The preliminary work presented in this chapter has been published in the form of a peer-reviewed book chapter, "Computational model of TASK channels and PKC-pathway dependent serotonergic modulatory effects in respiratory-related neurons." Adv Exp Med Biol. 2008;605:382-6. The author of this document is independently responsible for the work presented here.

the investigation of how neuromodulatory factors such as 5HT and pH can affect HM activities, and serves as a basis for further study in the area of long-term plasticity.

6.2 Methods & Results

The serotonergic modulation of calcium-signaling is mediated by two subtypes of 5-HT receptors, namely, the 5-HT_{1A} and the 5-HT_2 receptors (Bayliss et al. 1997). Both receptor subtypes are abundant in neonatal HM and the activation of each contributes differentially to the regulation of intracellular calcium profile. Activation of 5-HT_{1A} reduces current flow through N- and P/Q-type calcium channels and consequently inhibits after-hyperpolarization (AHP) caused by calcium-activated potassium current (Ladewig et al. 2004). On the other hand, the activation of 5-HT_2 receptors affects basal intracellular calcium concentration and has generally been linked to the PKC-pathway leading to calcium release from intracellular stores (Figure 6-1). The PKC-pathway involves phospholipase C (PLC)-mediated production of inositol triphosphate (IP_3) that leads to calcium release from intracellular stores and diacylglyceral (DAG) activation of protein kinase C leading to phosphorylation and dephosphorylation of membrane proteins.

Neurotransmitter-induced enhancement of excitability can be mediated by inhibition of a resting K+ current. TASK-1 channels, TASK-3 channels, as well as their heterodimers provide prominent leak K+ currents and are targets for neurotransmitter modulation in HMs (Berg et al. 2004). These pH-sensitive K+ channels can be fully inhibited by 5-HT, NE, SP among other neuromodulators and causes depolarization (Talley et al. 2000). Furthermore, it has been shown that 5-HT induced depolarizing current has a pH-sensitive component mediated by the TASK channels.

In the present work, we introduce a computational HM model that includes TASK channel conductance as well as cellular mechanisms for the protein kinase C (PKC) pathway that allow for neuromodulatory effect by 5-HT.

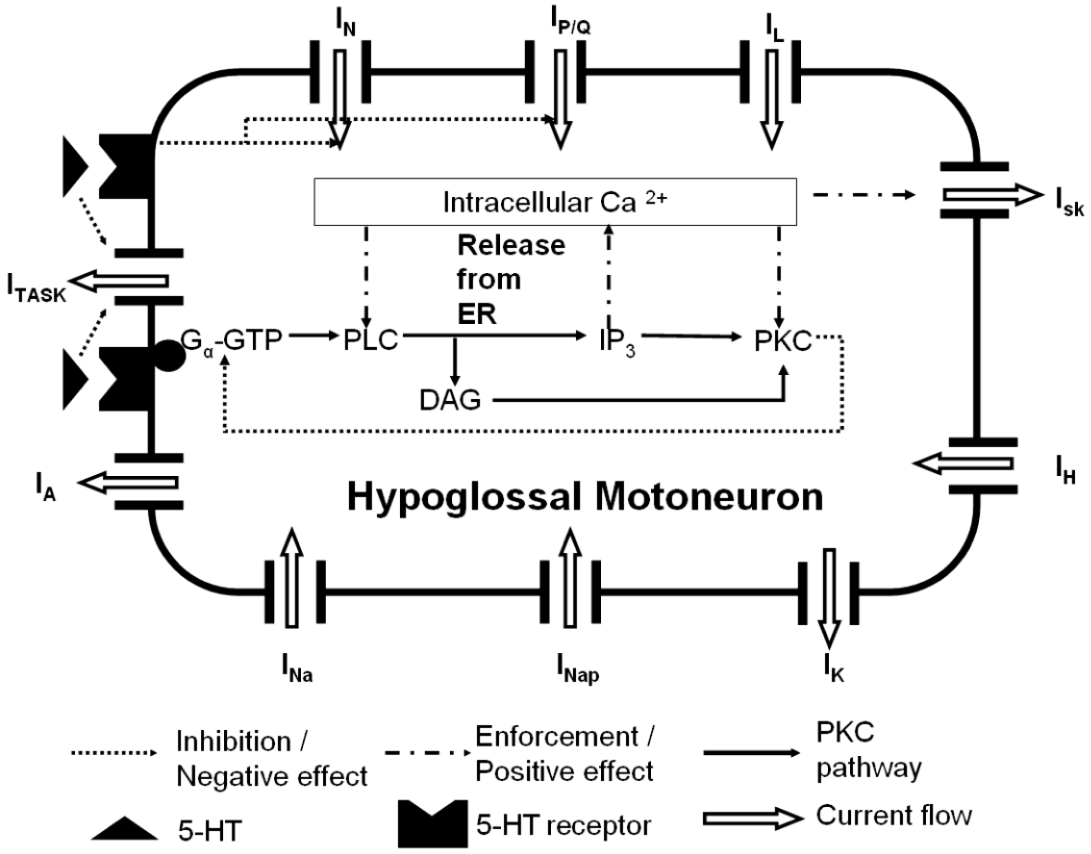

Figure 6.1 Schematic representation of our working modified HM model.

Our working model qualitatively reproduces features of serotonin-mediated effects on HM excitability. These features include increased membrane excitability, decreased AHP amplitude, elevated basal intracellular calcium concentration ($[Ca^{2+}]_i$), and depressed $[Ca^{2+}]_i$ oscillation amplitude. We started with the HM model of Purvis and Butera 2005. The total TASK-channel conductance of 3.5 nS was adopted from Talley et al. 2000. As proposed in Talley et al 2000, TASK channels are considered to be fully inhibited with the application of 5-HT. The mechanisms through which 5-HT receptor activation modulates $[Ca^{2+}]_i$ can be represented by a set of three simultaneous differential equations (Cuthbertson and Chay 1991):

$$d[G\text{-}GTP]/dt = r_g - h_g R_{pkc}[G\text{-}GTP] \quad (1)$$

where R_{pkc} is the fraction of activated PKC.

$$d[DAG]/dt = k_d R_{PLC} - h_d * [DAG] + l_d \quad (2)$$

where R_{PLC} is the fraction of activated PLC.

$d[Ca^{2+}]_i/dt = R_{IP3} - h_c[Ca^{2+}]_i + l_c$ *(3)*

The preliminary results from our working model are illustrated in Figure 6-2 and two scenarios were investigated. Scenario one considered 5-HT modulatory effect on intracellular calcium dynamics and consequently membrane electrodynamics. Results from scenario one are illustrated in panel A1 and A2 of Figure 6-2. The second scenario considers the effects of 5-HT on both calcium dynamics and TASK-channel conductance. The resulting intracellular calcium concentration profile and corresponding membrane potential trace are illustrated in panel B1 and B2. Action potentials were evoked via a 600-ms current pulse of 1 nA. Bath application of 5-HT (25 μM) was simulated for 200 ms and is signified by the horizontal bar in Figure 6-2.

The simulation results indicate that 5-HT application results in reduced AHP amplitude and consequently a higher AP firing frequency (Figure 6-2, Panel A1). The corresponding intracellular calcium profile (Figure 6-2. A2) demonstrate 5-HT modulatory effects characterized by an elevated basal $[Ca^{2+}]_i$ and smaller oscillation amplitude. The smaller oscillation amplitude is caused by calcium induced calcium

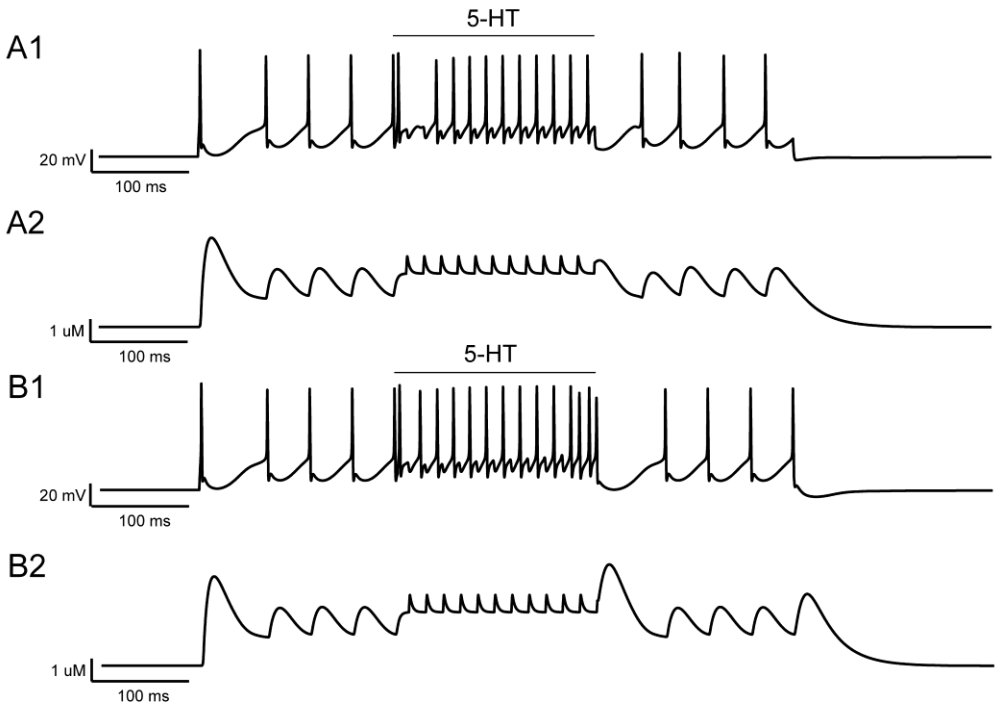

Figure 6.2 Simulating the serotonergic modulatory effects in HM. Panel A1 & A2, simulation results from considering only the modulatory effects mediated by the PKC-pathway. Panel B1 & B2, simulation results from considering modulatory effects mediated by both the PKC-pathway and the TASK channels. In both simulation scenarios, simulated membrane potential is shown in Panel A1 & B1; whereas corresponding intracellular calcium dynamics is shown in Panel A2 & B2. The readers are encouraged to refer to Appendix B for the results from an improved version of this model, as well as Ladewig et al. 2004 for the experiment results serving as the benchmark for this study.

release from the endoplasmic reticulum (Ladewig et al. 2003). When the inhibition of 5-HT on TASK-channel conductance is taken into consideration, the simulation results illustrate higher membrane excitability signified by accelerated AP firing frequency while the $[Ca^{2+}]_i$ profile remains unchanged from scenario one (Figure 6-2, Panel B1 & B2). The gradual increase in AP firing frequency can be attributed to a decrease in the fast-transient potassium current (I_A, results not shown).

6.3 Research Significance

Respiratory motoneuronal excitability is subject to modulation by several transmitters. Some of these modulatory effects, such as those mediated by 5-HT, are highly correlated with sleep-wake states and rhythmic motor activities (Murillo-Rodriguez et al. 2009). Activation of 5-HT receptors has been traditionally linked to the activation of PKC pathway. The PKC pathway can also be activated by mGluRs, which are also abundantly expressed in HMs. It has been proved that the PKC pathway is crucial to the induction of *ivLTF* in motoneurons and has a significant impact on intracellular calcium dynamics. The second feature of the PKC pathway renders more investigation because intracellular calcium dynamics have been linked to several physiological and patho-physiological states (Feldman et al. 2005). The disruption of calcium signaling can have detrimental effects especially in neurons such as HMs that have low calcium-buffering capacity (Lips and Keller 1999). In addition to peptidergic and serotonergic modulations, HMs are also subject to modulation by pH values. Variations in pH values are associated with physiological states such as hypoxia. The pH-sensitivity in HM is mediated by TASK channels, which are inhibited in acidic condition and activated in alkaline condition. Excitation caused by TASK-channel inhibition can also be with 5-HT and occur in be parallel with the activation of PKC pathway (Talley et al. 2000).

Our new HM model qualitatively reproduces observations of how 5-HT application can alter membrane electrodynamics both directly by inhibiting a "leak" conductance (TASK) and indirectly through the PKC-pathway ($[Ca^{2+}]_i$). This new HM model serves as a first step to modeling how neuromodulators affect respiratory-related motoneuronal activity either directly or via intracellular signaling pathway at a single cell level. Our next step is to modify this preliminary model so that the accelerated action potential firing frequency with 5-HT application falls within physiological range. Current implementation of the PKC-pathway can also be improved via differentiating effects mediated by different receptor subtypes. Additional second-messenger pathway

mediated by other protein kinases such as protein kinase A (PKA) and protein kinase G (PKG) can also be implemented for further investigation of how each pathway affects HM membrane electro-dynamics, such concept is outlined in further details in Chapter 7.

7. SUMMARY & FUTURE DIRECTION

7.1 Summary of work & limitations

The work presented in this document can be collectively considered as a preliminary treatment to investigating emergent network properties at different levels of networks existing in the transverse slice preparation. Starting from the level of intracellular networks exemplified by second-messenger pathways mediating neuromodulatory effects, and progressively moving toward higher structural levels, these networks include the network of a single nucleus (e.g. the PBC nucleus) consisting of identical neurons and the network of nuclei such as the transverse slice respiratory neural circuitry (e.g. the Raphé region, the PBC nucleus). The construction and integration of the pathway model – shown to be both significant in intracellular calcium metabolism and crucial for mediating neuromodulatory effects – into previous single neuron models facilitate the investigations of how exogenous factors such as 5HT can modulate single-cell activities (Chapter 5 & Chapter 6). Even though the complexity of the pathway model presented is drastically reduced from other published pathway models (Bhalla 2002; 2003), and studies presented in the document were conducted in isolation (e.g. without consider interactions with other pathways), the model has allowed for the qualitative reproduction of experiment observations and facilitated some preliminary network-level simulation work. In one of the ensuing sub-sections, the author of this document proposes how considering interactive pathway models might allow future researchers to understand long-term plastic phenomenon dependent on both stimulus pattern and strength.

Beyond the level of intracellular pathway and the level of single neuron, studies at the level of simulated PBC region with the improved single PBC model neuron, as well as with the Morris-Lecar model neuron, have also been presented in this document.

Based on the results from these studies, it has been shown that regardless of the mechanisms underlying the pacemaking properties in individual PBC neurons (Chapter 5), a special network structure called small-world can facilitate network-level rhythmic activities (Chapter 3). The interneuron coupling types and strengths, on the other hand, can interact and induce unexpected network-level phenomena at a time scale orders of magnitude larger than that of the couplings (Chapter 4). While the results presented are consistent with experiment observations and other modeling works, the all-to-all connectivity adopted in most of the network set-ups is unrealistic. It is the belief of the author of this document that more in-depth knowledge can be derived with network simulations adopting a small-world network topology where synaptic projections and gap-junctional couplings are assigned in a spatially relevant way. In other words, for future studies, the network connectivity can be modified such that clusters of neurons in the small-world are interconnected with synapses and gap junctions, while inter-cluster long-range connections are achieved by synaptic projections only.

Table 7.1 Major limitations of the work presented in this document.

Major limitations of the work presented in this document	
Chapter 3 – Network Topology	1. With improved computation technology, results can be refined using networks with PBC model neurons 2. The difference between clustered and long-range projections should also be expressed in the inter-neuron connection strengths and/or types
Chapter 4 – Inter-neuron interactions	1. All-to-all connectivity is unrealistic, insights derived from Chapter 3 were not incorporated 2. Insufficient experiment data on the strengths of gap-junctional couplings in the PBC region
Chapter 5 – CAN-burster & NAP-burster	1. Simplified second-messenger pathway

	2. Second-messenger pathway considered in isolation 3. Calcium buffering mechanism unaccounted for 4. Formulation of the G_q-term included in the model needs to be refined based on more experiment data
Chapter 6 – Hypoglossal Motoneuron	1. Simplified second-messenger pathway 2. Second-messenger pathway considered in isolation 3. Calcium buffering mechanism unaccounted for 4. Does not account for age-dependent differences in the electrical activities of HM observed in experiments

7.2 Proposed future studies

Using what have been accomplished in this document as basis, several possible future investigations in the area of respiratory neural control and rhythmogenesis are described in this section.

Pathway mediated long-term plasticity in Hypoglossal Motoneuron

There are two types of long-term plasticity of interest observed in HMs, *in vitro* long-term facilitation (ivLTF) and *in vivo* long-term facilitation (LTF). In the case of ivLTF, the plasticity is measured as activity-dependent postsynaptic enhancement of AMPA receptor function; whereas LTF is measured as an increase in respiratory motor output after episodic exposures to hypoxia. Both *in vivo* and *in vitro* respiratory long-term facilitation require mechanisms depending on intermittent, but not continuous, 5-HT_2 receptor activation, and it has been suggested that these long-lasting changes in the excitability involve PKC activation via the $G_{\alpha q}$-PLC signaling pathway downstream of serotonin receptor activation (Feldman et al. 2005).

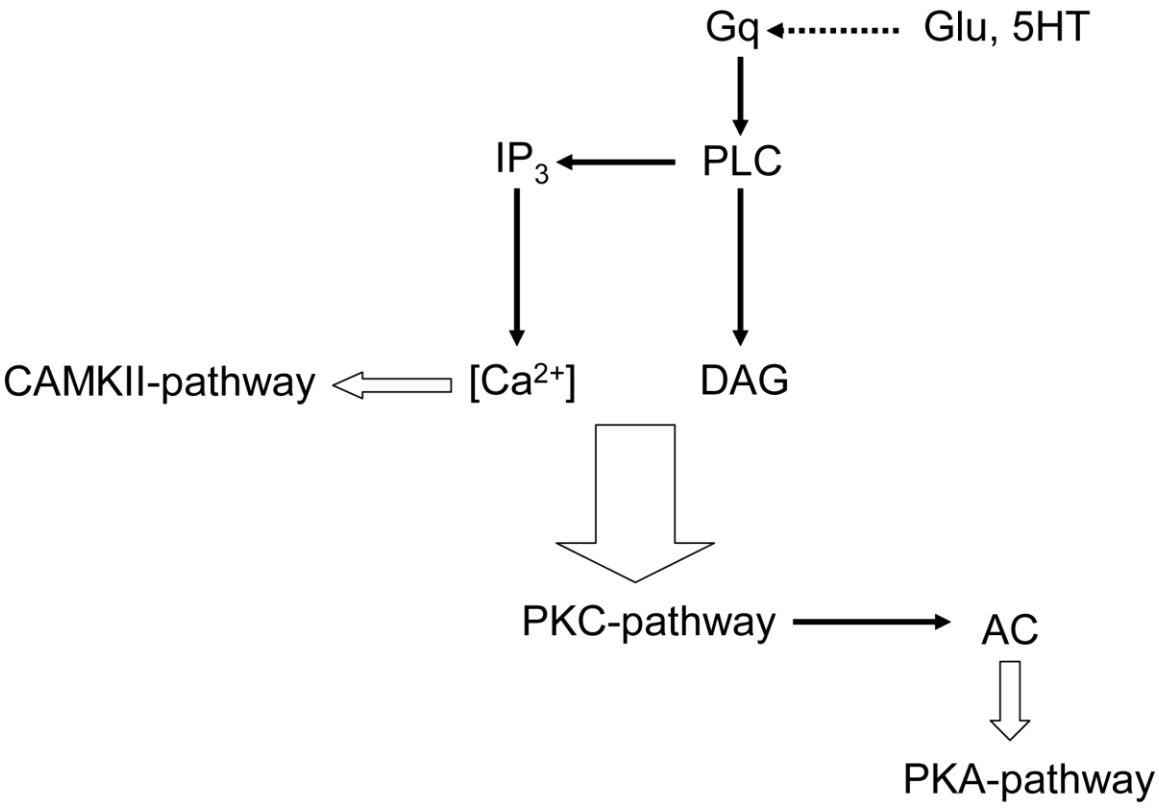

Figure 7.1 The interactions among different intracellular pathways. The PKC-pathway is not isolated in the intracellular space. The upstream contributor, [Ca2+], affects the CAMKII-pathway, and the protein kinase C itself interacts with AC and influence the PKA-pathway indirectly.

The PKC pathway is not isolated in the intracellular space (Bhalla 2002; 2003). In fact, the PKC pathway can interact with the PKA pathway via Adenylate Cyclase (AC), and the CAMKII pathway via intracellular calcium concentration (Figure 7-1). The PKA pathway and the CAMKII pathway have long been the focus of interest in the area of neuroscience investigating the late long-term potentiation (late-LTP) phenomenon in the CA1 region of hippocampus (Smolen et al. 2006). Previous experiment and modeling studies combined with experiments identifying gene transcription factors have allowed for investigations of how multiple kinase activities can converge and induce stimulus-pattern dependent plasticity which occurs at a much slower time scale (Bejar et al. 2002; Bhalla 2002; Hayer and Bhalla 2005; Mayford 2007; Smolen et al. 2006). By combining

these results from the modeling and experiment studies in areas other than respiratory neural control, further advances can be made to elucidate how intracellular pathways facilitate long-term plasticity in HMs. An HM model simulating stimuli pattern-dependent LTF by incorporating interacting second-messenger pathways and a calcium diffusion mechanism between intracellular compartments has been constructed by the author of this document. A conceptual design more detailed than that presented in Figure 7-1 as well as the simulation results were presented in SFN 2009 (Appendix C). However, these results are preliminary in nature and are not presented in this document.

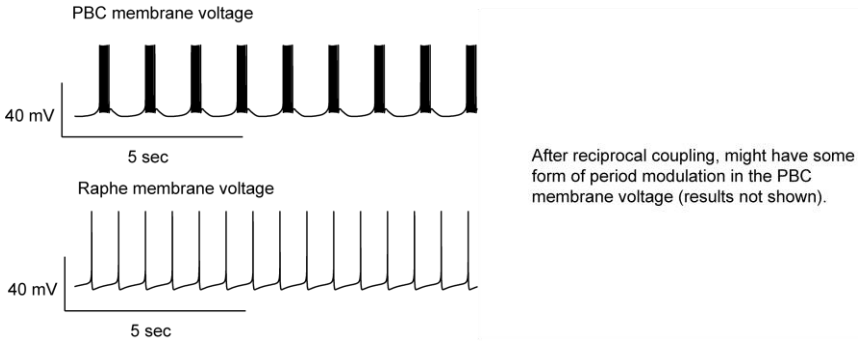

Figure 7.2 Significance of the serotonergic modulation from Raphé neuron: a preliminary study. Part of this proposed modeling work has been accomplished by the author of this document (results not shown), where the reciprocal connection between a model Raphé neuron and a PBC model neuron (prototypical CAN-burster, see Chapter 5) results in a significantly modulated burst period. Recall from Chapter 5 that, contrary to that of a NAP-burster, the burst period of a prototypical CAN-burster is resistant to depolarizing current injection.

Simulated Raphé modulatory effects in the CAN- & NAP-bursters

In addition to network-level studies presented in Chapter 5, where different types of pacemaking modes are examined separately at the network level, the author of this document has also independently completed two other relevant projects in early 2009 (results not shown). The first project focuses on the effects of mixing different percentages of CAN-bursters and NAP-bursters in a single network (e.g. a mixed-bursters network), and the second investigates the effects of different network topologies (e.g.

regular, SW, and random) in CAN-bursters, NAP-bursters, or mixed-bursters networks. Based on these studies, it can be concluded that in mixed-pacemakers networks, network-level activities quickly converge to those typical of a CAN-bursters network presented in Chapter 5 as soon as the percentage of CAN-bursters is increased beyond 20% regardless of the topologies.

This observation is especially interesting since, in addition to the differential changes in burst period and burst duration in response to depolarization observed in CAN-bursters and NAP-bursters respectively, experimental results have also shown that the pacemaking activities of CAN-bursters and NAP-bursters are modulated differently by serotonin. To facilitate future efforts in investigating the interactions between the PBC region and the Raphé nucleus (RN), a Raphé model neuron simulating all the characteristics of typical Raphé spiking activities was constructed by the author of this document (Figure 7-2). Since the new PBC model neuron presented in Chapter 5 includes mechanisms capable of simulating neuromodulatory effects on intracellular $[Ca^{2+}]$ and $[IP_3]$ via G-protein coupled receptors, reciprocally coupling it with the Raphé mode neuron provides a model system for investigations at the paired-cell level that can be further extended into investigations on the relationship between the RN and the PBC region. Figure 7-2 illustrates the concept for this proposed study.

Modeling the Transverse-Slice Respiratory Neural Circuitry

The goal of this proposed future study is to develop a next-generation transverse slice model that incorporates the current knowledge of the slice-level architecture with 5 neural populations: tonically firing neurons, Raphé neurons, PBC neurons, pre-motoneurons (preMNs), and HMs. Simulated networks containing improved versions of the single-cell models with more comprehensive second-messenger pathways than those presented in Chapter 5 & 6 of this document can be utilized in constructing the entire transverse slice model. While the inter-nuclei interactions should reflect the schematics

anatomically derived as illustrated in Figure 2-1, the intra-nucleus connections should base on the results from the investigations of the small-world topology presented in this document, as well as those from future investigations on the effects of physiologically and spatially relevant network connectivity set up.

The incorporation of interacting second-messenger pathways at the single neuron level leads to a transverse slice respiratory circuitry model which puts the investigation of neuromodulation into a larger context. This new frame work will facilitate in-depth understanding on how the respiratory neural control signals from this respiratory circuitry can be affected by multiple factors to result in interesting neural plasticity that is crucial for respiratory homeostasis, especially when the organism is in distress (e.g. hypoxia).

APPENDIX A

The IP3-ER-Ca^{2+} mechanism

With V representing the membrane voltage and $[Ca^{2+}]$ representing calcium concentration in the intracellular space, the IP3-ER-Ca^{2+} mechanisms included in the new generation PBC model neuron consists of the following equations:

$d[Ca^{2+}] / dt = \beta([Ca^{2+}]) \bullet (JER_{in} - JER_{out} - JEXT_{out})$

$d[IP_3] / dt = Gq(t, V) + P([Ca^{2+}]) - D([IP_3])$

$dw / dt = (w_{inf} - w) / \tau_w([Ca^{2+}])$

where

$\beta([Ca^{2+}]) = 1/\{tau * [1 + Kcyt*Bcyt/((Kcyt+[Ca^{2+}])\text{^}2)]\}$

$JER_{in} = c1*(v1*(w*[Ca^{2+}] / (d5 + [Ca^{2+}]))\text{^}3 + v2)*([Ca^{2+}]_{ER} - [Ca^{2+}]) - K* I_t$

$JER_{out} = v3*([Ca^{2+}]\text{^}2) / (k3\text{^}2 + [Ca^{2+}]\text{^}2)$

$[Ca^{2+}]_{ER}$ = Calcium concentration in the ER = $(1.20- [Ca^{2+}])/0.185$

I_t = fast inward calcium current = $gt*mt*ht*(V-E_{ca})$

where

mtinf = (1 + exp(-(Vm+38)/5))^-1

taumt = 2 + 5 / (exp((V+28) / 25) + exp(-(V+28) / 70))

htinf = (1 + exp((V+70.1)/7))^-1

tauht = 1 + 20 / (exp((V+70)/65) + exp(-(V+70)/65))

dmt /dt = (mtinf-mt) / taumt

dht / dt = (htinf-ht) / tauht

and

$P([Ca^{2+}]) = v6*[Ca^{2+}] / (k6 + [Ca^{2+}])$; $D([IP_3]) = v7*[IP_3]$

$w_{inf} = [IP_3]*d2 / ([IP_3] + d3) / (\alpha*d2 + [Ca^{2+}])$

$\tau_w([Ca^{2+}]) = 1 / (a2*(\alpha*d2 + [Ca^{2+}]))$

where

$\alpha = 1 / ((1 + Kcyt*Bcyt) / ((Kcyt + [Ca^{2+}])\text{^}2))$

Furthermore, as detailed in Section 5.2

$JEXT_{out} = 1 / (1+\exp((V+40) / -5))\bullet\ 0.26\bullet\ ([Ca^{2+}]\text{^}2) / (0.1 + [Ca^{2+}]\text{^}2)$

The following table shows the parameter values used in the formulation –

Table A.1 Parameter values for the IP3-ER-Ca^{2+} mechanism.

Parameter Name	Parameter Value
gt	1 nS
v1	6.5
v2	0.066
v3	0.9
v6	0.24
v7	0.1
c0	2
c1	0.185
c2	0.19
d1	0.13
d2	1.05
d3	0.943
d5	0.0823
a2	0.2
Bcyt	150
Kcan	0.8

Kcyt	1.5
K	0.0005 µM/pA
k3	0.1
k6	0.25
tau	0.01 msec

APPENDIX B

The PBC neuron model, Purvis et al. 2007 & Butera et al. 1999

The following equations for the four currents included in the original PBC neuron model where adopted from the appendix from Purvis et al. 2007.

(Sodium current) $I_{na} = g_{na} * m_{\infty}^3 * (1-n) * (V - E_{na})$

$n_{\infty} = 1/(1+\exp(-(V+29)/4))$, $\tau_n = 10$;

(Delayed rectifier current) $I_k = g_k * n^4 * (V - E_K)$

$n_{\infty} = 1/(1+\exp(-(V+29)/4))$, $\tau_n = 10$;

(Persistent sodium current) $I_{nap} = g_{nap} * m_{\infty} * h * (V - E_{na})$

$m_{\infty} = 1/(1+\exp(-(V+45.1)/5))$;

$h_{\infty} = 1/(1+\exp((V+53)/6))$, $\tau_h = 10000$;

(Leak current) $I_{leak} = g_{leak} * (V - E_{leak})$

The hypoglossal motoneuron (HM) model, Purvis et al. 2005

The following equations for the ten currents included in the original HM model were adopted from the appendix from Purvis et al. 2005.

(Sodium current) $I_{na} = g_{na} * m^3 * h * (V - E_{na})$;

$m_{\infty} = 1/(1+\exp(-(V+36)/8.5))$, $\tau_m = 0.1$;

$h_{\infty} = 1/(1+\exp((V+44.1)/7))$, $\tau_h = 3.5/(\exp((V+35)/4) + \exp(-(V+35)/25)) + 1$;

(Persistent sodium current) $I_{nap} = g_{nap} * m_{nap} * h_{nap} * (V - E_{na})$;

$m_{nap-\infty} = 1/(1+\exp(-(V+47.1)/4.1)$, $\tau_{mnap} = 0.1$;

$h_{nap-\infty} = 1/(1+\exp((V+65)/5)$, $\tau_{hnap} = 150$;

(Delayed rectifier current) $I_k = g_k * n^4 * (V - E_k)$;

$n_{\infty} = 1/(1+\exp(-(V+30)/25)$, $\tau_n = 2.5/(\exp((V+30)/40) + \exp(-(V+30)/50)) + 0.01$

(Leak current) $I_{leak} = g_{leak} * (V - E_{leak})$

(Low-voltage activated calcium current) $I_t = g_t * m_t * h_t * (V - E_{ca})$

$m_{t-\infty} = 1/(1+\exp(-(V+38)/5)$, $\tau_{mt} = 5/(\exp((V+28)/25) + \exp(-(V+28)/70)) + 2$;

$h_{t-\infty} = 1/(1+\exp((V+70.1)/7)$, $\tau_{ht} = 20/(\exp((V+70)/65) + \exp(-(V+70)/65)) + 1$;

(High-voltage activated current) $I_n = g_n * m_n * h_n * (V - E_{ca})$

$m_{n-\infty} = 1/(1+\exp(-(V+30)/6))$, $\tau_{mn} = 5$;

$h_{n-\infty} = 1/(1+\exp((V+70)/3))$, $\tau_{hn} = 25$;

(High-voltage activated current) $I_p = g_p * m_p * (V - E_{ca})$

$m_{p-\infty} = 1/(1+\exp(-(V+17)/3)$, $\tau_{mp} = 10$;

(Calcium-dependent potassium current) $I_{sk} = g_{sk} * z_{sk}^2 * (V - E_k)$

$z_{sk} = 1/(1+(0.003/[Ca^{2+}])^2)$, $\tau_{sk} = 1$;

(Fast transient potassium current) $I_a = g_a * m_a * h_a * (V - E_k)$

$m_{a-\infty} = 1/(1+\exp(-(V+27)/6))$, $\tau_{ma} = 1/(\exp((V+40)/5) + \exp(-(V+74)/7.5)) +0.37$;

$h_{a-\infty} = 1/(1+\exp((V+80)/11))$, $\tau_{ha} = 20$;

(Hyperpolarization-activated current) $I_h = g_h * m_h * (V - E_h)$

$m_{h-\infty} = 1/(1+\exp((V+79.8)/5.3))$,

$\tau_{mh} = 475/(\exp((V+70)/11) + \exp(-(V+70)/11)) + 50$

APPENDIX C

The preliminary transverse slice model – poster from SFN 2009

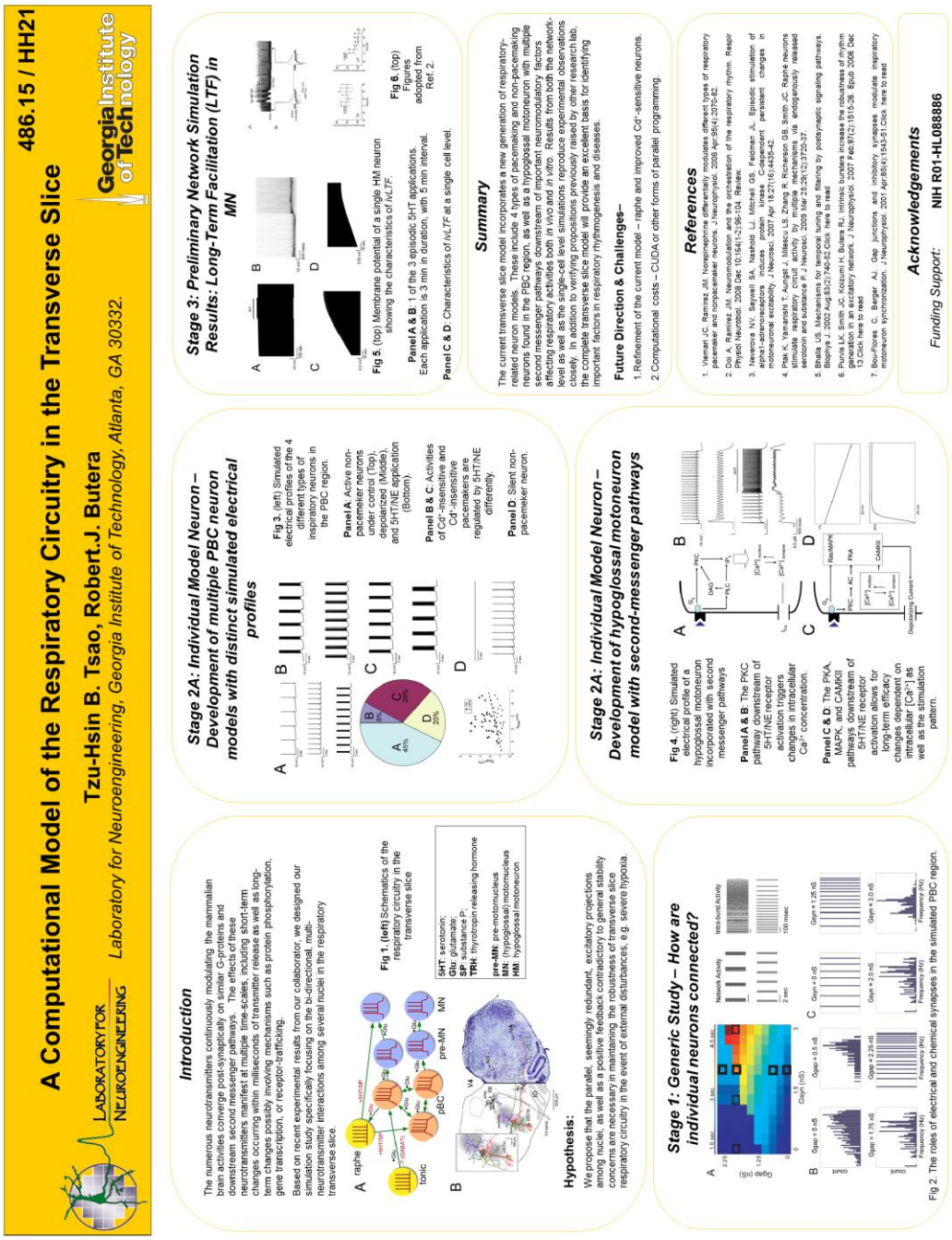

REFERENCES

Bayliss DA, Talley EM, Sirois JE, and Lei Q. TASK-1 is a highly modulated pH-sensitive 'leak' K(+) channel expressed in brainstem respiratory neurons. *Respir Physiol* 129: 159-174, 2001.

Bayliss DA, Viana F, Talley EM, and Berger AJ. Neuromodulation of hypoglossal motoneurons: cellular and developmental mechanisms. *Respir Physiol* 110: 139-150, 1997.

Becker LE, and Zhang W. Vagal nerve complex in normal development and sudden infant death syndrome. *Can J Neurol Sci* 23: 24-33, 1996.

Bejar R, Yasuda R, Krugers H, Hood K, and Mayford M. Transgenic calmodulin-dependent protein kinase II activation: dose-dependent effects on synaptic plasticity, learning, and memory. *J Neurosci* 22: 5719-5726, 2002.

Berg AP, Talley EM, Manger JP, and Bayliss DA. Motoneurons express heteromeric TWIK-related acid-sensitive K+ (TASK) channels containing TASK-1 (KCNK3) and TASK-3 (KCNK9) subunits. *J Neurosci* 24: 6693-6702, 2004.

Bertram R, Butte MJ, Kiemel T, and Sherman A. Topological and phenomenological classification of bursting oscillations. *Bull Math Biol* 57: 413-439, 1995.

Bhalla US. Biochemical signaling networks decode temporal patterns of synaptic input. *J Comput Neurosci* 13: 49-62, 2002.

Bhalla US. Temporal computation by synaptic signaling pathways. *J Chem Neuroanat* 26: 81-86, 2003.

Bianchi AL, Denavit-Saubie M, and Champagnat J. Central control of breathing in mammals: neuronal circuitry, membrane properties, and neurotransmitters. *Physiol Rev* 75: 1-45, 1995.

Boersma M, Smit DJ, de Bie HM, Van Baal GC, Boomsma DI, de Geus EJ, Delemarre-van de Waal HA, and Stam CJ. Network analysis of resting state EEG in the developing young brain: Structure comes with maturation. *Hum Brain Mapp*.

Bou-Flores C, and Berger AJ. Gap junctions and inhibitory synapses modulate inspiratory motoneuron synchronization. *J Neurophysiol* 85: 1543-1551, 2001.

Bracci E, Ballerini L, and Nistri A. Localization of rhythmogenic networks responsible for spontaneous bursts induced by strychnine and bicuculline in the rat isolated spinal cord. *J Neurosci* 16: 7063-7076, 1996.

Brockhaus J, and Ballanyi K. Synaptic inhibition in the isolated respiratory network of neonatal rats. *Eur J Neurosci* 10: 3823-3839, 1998.

Butera RJ, Jr., Rinzel J, and Smith JC. Models of respiratory rhythm generation in the pre-Botzinger complex. I. Bursting pacemaker neurons. *J Neurophysiol* 82: 382-397, 1999a.

Butera RJ, Jr., Rinzel J, and Smith JC. Models of respiratory rhythm generation in the pre-Botzinger complex. II. Populations Of coupled pacemaker neurons. *J Neurophysiol* 82: 398-415, 1999b.

Carpentier V, Vaudry H, Mallet E, Laquerriere A, and Leroux P. Increased density of somatostatin binding sites in respiratory nuclei of the brainstem in sudden infant death syndrome. *Neuroscience* 86: 159-166, 1998.

Cha CY, Oka C, Earm YE, Wakabayashi S, and Noma A. A model of Na+/H+ exchanger and its central role in regulation of pH and Na+ in cardiac myocytes. *Biophys J* 97: 2674-2683, 2009.

Chang D, Dokos S, and Lovell NH. Modelling heart beat initiation and propagation using the MML framework. *Conf Proc IEEE Eng Med Biol Soc* 2009: 4495-4498, 2009.

Cuthbertson KS, and Chay TR. Modelling receptor-controlled intracellular calcium oscillators. *Cell Calcium* 12: 97-109, 1991.

Del Negro CA, and Hayes JA. A 'group pacemaker' mechanism for respiratory rhythm generation. *J Physiol* 586: 2245-2246, 2008.

Del Negro CA, Koshiya N, Butera RJ, Jr., and Smith JC. Persistent sodium current, membrane properties and bursting behavior of pre-botzinger complex inspiratory neurons in vitro. *J Neurophysiol* 88: 2242-2250, 2002a.

Del Negro CA, Morgado-Valle C, and Feldman JL. Respiratory rhythm: an emergent network property? *Neuron* 34: 821-830, 2002b.

Del Negro CA, Pace RW, and Hayes JA. What role do pacemakers play in the generation of respiratory rhythm? *Adv Exp Med Biol* 605: 88-93, 2008.

Doi A, and Ramirez JM. Neuromodulation and the orchestration of the respiratory rhythm. *Respir Physiol Neurobiol* 164: 96-104, 2008.

Doi I, Zanella S, Wei A, Bedogni F, Hodge R, Daza R, Hevner R, and Ramirez JM. Functional interactions among NK1, alpha1 (NE) and 5-HT2 receptors on respiratory rhythm in the Pre-Bötzinger complex. *27014/CC27 , Poster Session, Society of Neuroscience* 2009.

Elsen FP, Shields EJ, Roe MT, Vandam RJ, and Kelty JD. Carbenoxolone induced depression of rhythmogenesis in the pre-Botzinger Complex. *BMC Neurosci* 9: 46, 2008.

Feldman JL, Neverova NV, and Saywell SA. Modulation of hypoglossal motoneuron excitability by intracellular signal transduction cascades. *Respir Physiol Neurobiol* 147: 131-143, 2005.

Feldman JL, and Smith JC. Cellular mechanisms underlying modulation of breathing pattern in mammals. *Ann N Y Acad Sci* 563: 114-130, 1989.

Feldman JL, Smith JC, and Liu G. Respiratory pattern generation in mammals: in vitro en bloc analyses. *Curr Opin Neurobiol* 1: 590-594, 1991.

Francesconi A, and Duvoisin RM. Opposing effects of protein kinase C and protein kinase A on metabotropic glutamate receptor signaling: selective desensitization of the inositol trisphosphate/Ca2+ pathway by phosphorylation of the receptor-G protein-coupling domain. *Proc Natl Acad Sci U S A* 97: 6185-6190, 2000.

Funk GD, Smith JC, and Feldman JL. Generation and transmission of respiratory oscillations in medullary slices: role of excitatory amino acids. *J Neurophysiol* 70: 1497-1515, 1993.

Gong G, Rosa-Neto P, Carbonell F, Chen ZJ, He Y, and Evans AC. Age- and gender-related differences in the cortical anatomical network. *J Neurosci* 29: 15684-15693, 2009.

Gray PA, Janczewski WA, Mellen N, McCrimmon DR, and Feldman JL. Normal breathing requires preBotzinger complex neurokinin-1 receptor-expressing neurons. *Nat Neurosci* 4: 927-930, 2001.

Guntheroth WG, and Spiers PS. The triple risk hypotheses in sudden infant death syndrome. *Pediatrics* 110: e64, 2002.

Harris RE, Coulombe MG, and Feller MB. Dissociated retinal neurons form periodically active synaptic circuits. *J Neurophysiol* 88: 188-195, 2002.

Hartelt N, Skorova E, Manzke T, Suhr M, Mironova L, Kugler S, and Mironov SL. Imaging of respiratory network topology in living brainstem slices. *Mol Cell Neurosci* 37: 425-431, 2008.

Hayer A, and Bhalla US. Molecular switches at the synapse emerge from receptor and kinase traffic. *PLoS Comput Biol* 1: 137-154, 2005.

Hodgkin AL, and Huxley AF. A quantitative description of membrane current and its application to conduction and excitation in nerve. *J Physiol* 117: 500-544, 1952.

Izhikevich EM. Neural Excitability, Spiking, and Bursting. *International Journal of Bifurcation and Chaos* 10: 1171-1266, 2000.

Keizer J, and De Young GW. Two roles of Ca2+ in agonist stimulated Ca2+ oscillations. *Biophys J* 61: 649-660, 1992.

Kinney HC, Myers MM, Belliveau RA, Randall LL, Trachtenberg FL, Fingers ST, Youngman M, Habbe D, and Fifer WP. Subtle autonomic and respiratory dysfunction in sudden infant death syndrome associated with serotonergic brainstem abnormalities: a case report. *J Neuropathol Exp Neurol* 64: 689-694, 2005.

Kinney HC, Panigrahy A, Rava LA, and White WF. Three-dimensional distribution of [3H]quinuclidinyl benzilate binding to muscarinic cholinergic receptors in the developing human brainstem. *J Comp Neurol* 362: 350-367, 1995.

Koizumi H, Smerin SE, Yamanishi T, Moorjani BR, Zhang R, and Smith JC. TASK channels contribute to the K+-dominated leak current regulating respiratory rhythm generation in vitro. *J Neurosci* 30: 4273-4284.

Koshiya N, and Guyenet PG. Tonic sympathetic chemoreflex after blockade of respiratory rhythmogenesis in the rat. *J Physiol* 491 (Pt 3): 859-869, 1996.

Koshiya N, and Smith JC. Neuronal pacemaker for breathing visualized in vitro. *Nature* 400: 360-363, 1999.

Kosmidis EK, Pierrefiche O, and Vibert JF. Respiratory-like rhythmic activity can be produced by an excitatory network of non-pacemaker neuron models. *J Neurophysiol* 92: 686-699, 2004.

Kumar N, Hendriks BS, Janes KA, de Graaf D, and Lauffenburger DA. Applying computational modeling to drug discovery and development. *Drug Discov Today* 11: 806-811, 2006.

Ladewig T, Kloppenburg P, Lalley PM, Zipfel WR, Webb WW, and Keller BU. Spatial profiles of store-dependent calcium release in motoneurones of the nucleus hypoglossus from newborn mouse. *J Physiol* 547: 775-787, 2003.

Ladewig T, Lalley PM, and Keller BU. Serotonergic modulation of intracellular calcium dynamics in neonatal hypoglossal motoneurons from mouse. *Brain Res* 1001: 1-12, 2004.

Lega BC, Halpern CH, Jaggi JL, and Baltuch GH. Deep brain stimulation in the treatment of refractory epilepsy: update on current data and future directions. *Neurobiol Dis* 38: 354-360.

Lieske SP, and Ramirez JM. Pattern-specific synaptic mechanisms in a multifunctional network. II. Intrinsic modulation by metabotropic glutamate receptors. *J Neurophysiol* 95: 1334-1344, 2006.

Lips MB, and Keller BU. Activity-related calcium dynamics in motoneurons of the nucleus hypoglossus from mouse. *J Neurophysiol* 82: 2936-2946, 1999.

Mathews TJ, and MacDorman MF. Infant mortality statistics from the 2003 period linked birth/infant death data set. *Natl Vital Stat Rep* 54: 1-29, 2006.

Mayford M. Protein kinase signaling in synaptic plasticity and memory. *Curr Opin Neurobiol* 17: 313-317, 2007.

McIntyre CC, Savasta M, Kerkerian-Le Goff L, and Vitek JL. Uncovering the mechanism(s) of action of deep brain stimulation: activation, inhibition, or both. *Clin Neurophysiol* 115: 1239-1248, 2004.

Mellen NM, Milsom WK, and Feldman JL. Hypothermia and recovery from respiratory arrest in a neonatal rat in vitro brain stem preparation. *Am J Physiol Regul Integr Comp Physiol* 282: R484-491, 2002.

Mironov S. Respiratory circuits: function, mechanisms, topology, and pathology. *Neuroscientist* 15: 194-208, 2009.

Mironov SL, Skorova E, Hartelt N, Mironova LA, Hasan MT, and Kugler S. Remodelling of the respiratory network in a mouse model of Rett syndrome depends on brain-derived neurotrophic factor regulated slow calcium buffering. *J Physiol* 587: 2473-2485, 2009.

Morris C, and Lecar H. Voltage oscillations in the barnacle giant muscle fiber. *Biophys J* 35: 193-213, 1981.

Murillo-Rodriguez E, Arias-Carrion O, Sanguino-Rodriguez K, Gonzalez-Arias M, and Haro R. Mechanisms of sleep-wake cycle modulation. *CNS Neurol Disord Drug Targets* 8: 245-253, 2009.

Nattie EE, Li A, Richerson GB, and Lappi DA. Medullary serotonergic neurones and adjacent neurones that express neurokinin-1 receptors are both involved in chemoreception in vivo. *J Physiol* 556: 235-253, 2004.

Netoff TI, Clewley R, Arno S, Keck T, and White JA. Epilepsy in small-world networks. *J Neurosci* 24: 8075-8083, 2004.

Neverova NV, Saywell SA, Nashold LJ, Mitchell GS, and Feldman JL. Episodic stimulation of alpha1-adrenoreceptors induces protein kinase C-dependent persistent changes in motoneuronal excitability. *J Neurosci* 27: 4435-4442, 2007.

Newman ME, and Watts DJ. Scaling and percolation in the small-world network model. *Phys Rev E Stat Phys Plasmas Fluids Relat Interdiscip Topics* 60: 7332-7342, 1999.

Obonai T, and Takashima S. In utero brain lesions in SIDS. *Pediatr Neurol* 19: 23-25, 1998.

Obonai T, Yasuhara M, Nakamura T, and Takashima S. Catecholamine neurons alteration in the brainstem of sudden infant death syndrome victims. *Pediatrics* 101: 285-288, 1998.

Onimaru H, Arata A, and Homma I. Inhibitory synaptic inputs to the respiratory rhythm generator in the medulla isolated from newborn rats. *Pflugers Arch* 417: 425-432, 1990.

Panigrahy A, Filiano J, Sleeper LA, Mandell F, Valdes-Dapena M, Krous HF, Rava LA, Foley E, White WF, and Kinney HC. Decreased serotonergic receptor binding in rhombic lip-derived regions of the medulla oblongata in the sudden infant death syndrome. *J Neuropathol Exp Neurol* 59: 377-384, 2000.

Patel AJ, and Honore E. Molecular physiology of oxygen-sensitive potassium channels. *Eur Respir J* 18: 221-227, 2001.

Paterson DS, Trachtenberg FL, Thompson EG, Belliveau RA, Beggs AH, Darnall R, Chadwick AE, Krous HF, and Kinney HC. Multiple serotonergic brainstem abnormalities in sudden infant death syndrome. *JAMA* 296: 2124-2132, 2006.

Pena F, Parkis MA, Tryba AK, and Ramirez JM. Differential contribution of pacemaker properties to the generation of respiratory rhythms during normoxia and hypoxia. *Neuron* 43: 105-117, 2004.

Pena F, and Ramirez JM. Endogenous activation of serotonin-2A receptors is required for respiratory rhythm generation in vitro. *J Neurosci* 22: 11055-11064, 2002.

Pena F, and Ramirez JM. Substance P-mediated modulation of pacemaker properties in the mammalian respiratory network. *J Neurosci* 24: 7549-7556, 2004.

Ponten SC, Bartolomei F, and Stam CJ. Small-world networks and epilepsy: graph theoretical analysis of intracerebrally recorded mesial temporal lobe seizures. *Clin Neurophysiol* 118: 918-927, 2007.

Protas L, Oren RV, Clancy CE, and Robinson RB. Age-dependent changes in Na current magnitude and TTX-sensitivity in the canine sinoatrial node. *J Mol Cell Cardiol* 48: 172-180, 2010.

Ptak K, Di Pasquale E, and Monteau R. Substance P and central respiratory activity: a comparative in vitro study on foetal and newborn rat. *Brain Res Dev Brain Res* 114: 217-227, 1999.

Ptak K, Yamanishi T, Aungst J, Milescu LS, Zhang R, Richerson GB, and Smith JC. Raphe neurons stimulate respiratory circuit activity by multiple mechanisms via endogenously released serotonin and substance P. *J Neurosci* 29: 3720-3737, 2009.

Purvis LK, and Butera RJ. Ionic current model of a hypoglossal motoneuron. *J Neurophysiol* 93: 723-733, 2005.

Purvis LK, Smith JC, Koizumi H, and Butera RJ. Intrinsic bursters increase the robustness of rhythm generation in an excitatory network. *J Neurophysiol* 97: 1515-1526, 2007.

Puzianowska-Kuznicka M, and Kuznicki J. The ER and ageing II: calcium homeostasis. *Ageing Res Rev* 8: 160-172, 2009.

Raastad M, Johnson BR, and Kiehn O. The number of postsynaptic currents necessary to produce locomotor-related cyclic information in neurons in the neonatal rat spinal cord. *Neuron* 17: 729-738, 1996.

Rajasethupathy P, Vayttaden SJ, and Bhalla US. Systems modeling: a pathway to drug discovery. *Curr Opin Chem Biol* 9: 400-406, 2005.

Ramirez JM, and Richter DW. The neuronal mechanisms of respiratory rhythm generation. *Curr Opin Neurobiol* 6: 817-825, 1996.

Ramirez JM, Schwarzacher SW, Pierrefiche O, Olivera BM, and Richter DW. Selective lesioning of the cat pre-Botzinger complex in vivo eliminates breathing but not gasping. *J Physiol* 507 (Pt 3): 895-907, 1998.

Rekling JC, Shao XM, and Feldman JL. Electrical coupling and excitatory synaptic transmission between rhythmogenic respiratory neurons in the preBotzinger complex. *J Neurosci* 20: RC113, 2000.

Richerson GB. Serotonergic neurons as carbon dioxide sensors that maintain pH homeostasis. *Nat Rev Neurosci* 5: 449-461, 2004.

Richter DW, Ballanyi K, and Schwarzacher S. Mechanisms of respiratory rhythm generation. *Curr Opin Neurobiol* 2: 788-793, 1992.

Richter DW, Manzke T, Wilken B, and Ponimaskin E. Serotonin receptors: guardians of stable breathing. *Trends Mol Med* 9: 542-548, 2003.

Rinzel J. *Bursting Oscillations in an Excitable Membrane Model*. Springer Berlin / Heidelberg, 1985.

Rohr S. Role of gap junctions in the propagation of the cardiac action potential. *Cardiovasc Res* 62: 309-322, 2004.

Ruangkittisakul A, Schwarzacher SW, Secchia L, Ma Y, Bobocea N, Poon BY, Funk GD, and Ballanyi K. Generation of eupnea and sighs by a spatiochemically organized inspiratory network. *J Neurosci* 28: 2447-2458, 2008.

Rubin JE. Emergent bursting in small networks of model conditional pacemakers in the pre-Botzinger complex. *Adv Exp Med Biol* 605: 119-124, 2008.

Rubin JE, Shevtsova NA, Ermentrout GB, Smith JC, and Rybak IA. Multiple rhythmic states in a model of the respiratory central pattern generator. *J Neurophysiol* 101: 2146-2165, 2009.

Rybak IA, Abdala AP, Markin SN, Paton JF, and Smith JC. Spatial organization and state-dependent mechanisms for respiratory rhythm and pattern generation. *Prog Brain Res* 165: 201-220, 2007.

Saito Y, Ito M, Ozawa Y, Matsuishi T, Hamano K, and Takashima S. Reduced expression of neuropeptides can be related to respiratory disturbances in Rett syndrome. *Brain Dev* 23 Suppl 1: S122-126, 2001.

Saywell SA, and Feldman JL. Dynamic interactions of excitatory and inhibitory inputs in hypoglossal motoneurones: respiratory phasing and modulation by PKA. *J Physiol* 554: 879-889, 2004.

Schwarzacher SW, Smith JC, and Richter DW. Pre-Botzinger complex in the cat. *J Neurophysiol* 73: 1452-1461, 1995.

Sherman A, and Rinzel J. Rhythmogenic effects of weak electrotonic coupling in neuronal models. *Proc Natl Acad Sci U S A* 89: 2471-2474, 1992.

Singer JH, and Berger AJ. Development of inhibitory synaptic transmission to motoneurons. *Brain Res Bull* 53: 553-560, 2000.

Smith JC, Ellenberger HH, Ballanyi K, Richter DW, and Feldman JL. Pre-Botzinger complex: a brainstem region that may generate respiratory rhythm in mammals. *Science* 254: 726-729, 1991.

Smith JC, Greer JJ, Liu GS, and Feldman JL. Neural mechanisms generating respiratory pattern in mammalian brain stem-spinal cord in vitro. I. Spatiotemporal patterns of motor and medullary neuron activity. *J Neurophysiol* 64: 1149-1169, 1990.

Smolen P, Baxter DA, and Byrne JH. A model of the roles of essential kinases in the induction and expression of late long-term potentiation. *Biophys J* 90: 2760-2775, 2006.

Solomon IC, Edelman NH, and Neubauer JA. Patterns of phrenic motor output evoked by chemical stimulation of neurons located in the pre-Botzinger complex in vivo. *J Neurophysiol* 81: 1150-1161, 1999.

Suzue T. Respiratory rhythm generation in the in vitro brain stem-spinal cord preparation of the neonatal rat. *J Physiol* 354: 173-183, 1984.

Tadjalli A, and Peever J. Role of neurotrophic signaling pathways in regulating respiratory motor plasticity. *Adv Exp Med Biol* 669: 293-296.

Talley EM, Lei Q, Sirois JE, and Bayliss DA. TASK-1, a two-pore domain K+ channel, is modulated by multiple neurotransmitters in motoneurons. *Neuron* 25: 399-410, 2000.

Thoby-Brisson M, and Ramirez JM. Identification of two types of inspiratory pacemaker neurons in the isolated respiratory neural network of mice. *J Neurophysiol* 86: 104-112, 2001.

Tribulova N, Knezl V, Okruhlicova L, and Slezak J. Myocardial gap junctions: targets for novel approaches in the prevention of life-threatening cardiac arrhythmias. *Physiol Res* 57 Suppl 2: S1-S13, 2008.

Tryba AK, Pena F, and Ramirez JM. Stabilization of bursting in respiratory pacemaker neurons. *J Neurosci* 23: 3538-3546, 2003.

Viemari JC, and Ramirez JM. Norepinephrine differentially modulates different types of respiratory pacemaker and nonpacemaker neurons. *J Neurophysiol* 95: 2070-2082, 2006.

Wagner J, and Keizer J. Effects of rapid buffers on Ca2+ diffusion and Ca2+ oscillations. *Biophys J* 67: 447-456, 1994.

Wang H, Stornetta RL, Rosin DL, and Guyenet PG. Neurokinin-1 receptor-immunoreactive neurons of the ventral respiratory group in the rat. *J Comp Neurol* 434: 128-146, 2001.

Wang J, Irnaten M, Venkatesan P, Evans C, Baxi S, and Mendelowitz D. Synaptic activation of hypoglossal respiratory motorneurons during inspiration in rats. *Neurosci Lett* 332: 195-199, 2002.

Watts DJ. Small Worlds. *Princeton University Press* 1999.

Watts DJ, and Strogatz SH. Collective dynamics of 'small-world' networks. *Nature* 393: 440-442, 1998.

Wright TM, and Butera RJ. Modeling study of the dynamical effects of electrical coupling on pre-Botzinger complex neurons. *Program No 63522006, Society for Neuroscience* 2006.

Yan C, Gong G, Wang J, Wang D, Liu D, Zhu C, Chen ZJ, Evans A, Zang Y, and He Y. Sex- and Brain Size-Related Small-World Structural Cortical Networks in Young Adults: A DTI Tractography Study. *Cereb Cortex* 2010.

Zanella S, Garcia AJ, Doi A, Hodge R, Hevner R, and Ramirez JM. Acute intermittent hypoxia alters norepinephrine modulation from stabilizing to destabilizing respiratory activity in mice. *27012/CC25, Poster Session, Society of Neuroscience* 2009.